MFSD7C is an ATP Transporter that Supports Bacterial Killing by Alveolar Macrophages in a Lipid-Rich Microenvironment

by

Douglas R. Brown
B.S. Biochemistry
Boston College, 2013

Submitted to the Department of Biology
in Partial Fulfillment of the Requirements for the Degree of

Doctor of Philosophy

at the

Massachusetts Institute of Technology

September 2022

Signature of the Author

Department of Biology
July 26, 2022

Certified by

Thesis supervisor
Jianzhu Chen, PhD
Professor of Biology

Accepted by

Co-Director, Biology Graduate Committee
Amy E. Keating, PhD
Professor of Biology and Biological Engineering

MFSD7C is an ATP Transporter that Supports Bacterial Killing by Alveolar Macrophages in a Lipid-Rich Microenvironment

by

Douglas R. Brown

Submitted to the Graduate Program in Biology on July 26, 2022
in Partial Fulfillment of the Requirements for the Degree of

Doctor of Philosophy

at the

Massachusetts Institute of Technology

ABSTRACT

Major Facilitator Superfamily Domain-Containing 7C (MFSD7C) is a solute carrier with unknown substrate. In humans, mutations in *MFSD7C* cause Fowler syndrome, which is characterized by aberrant development of fetal vasculature in the brain resulting in hydranencephaly-hydrocephaly. Although most Fowler Syndrome patients do not survive past birth, those who do often experience recurrent respiratory infections. We now show that Mfsd7c-deficient alveolar macrophages in mice have an impaired ability to counter infection. This is demonstrated to be due to their altered metabolic state, characterized by heightened glycolysis and reduced lipid oxidation. When Mfsd7c-deficient alveolar macrophages encounter bacteria with glucose available as a nutrient, their deficiency in bacterial killing is abrogated. We then examine the purified protein MFSD7C and perform a candidate substrate screen using a thermostability-shift assay. We identify ATP as a putative substrate for MFSD7C and validate that 32P ATP can be absorbed by *E. coli* expressing the protein. We also determine that heme increases the rate of ATP uptake, prompting us to examine the effects of heme on ATP transport in alveolar macrophages. We find that heme rapidly and dramatically increases the rate of ATP export by Mfsd7c, providing insight into how this protein may modulate thermogenesis and metabolism as previously observed.

Thesis Supervisor: Jianzhu Chen
Title: Professor of Biology

Acknowledgments

This journey would not have been possible without the selfless help and support that I received from my professors, family, and friends.

First, I would like to thank my thesis advisor and mentor, Professor Jianzhu Chen, PhD, who guided me through the intricacies and pitfalls of scientific research. I am also grateful for the support that I received from my thesis committee members Professor Matthew Vander Heiden, MD, PhD, and Professor Omer Yilmaz, MD, PhD. I would additionally like to express my gratitude to my previous mentors Professor Deborah Hung, MD, PhD, and Professor Eranthie Weerapana, PhD, for everything they have taught me.

I would like to thank my entire family for their continued support throughout my education. Mom, Dad, Mikey, Gunf, Turps - thank you for being such amazing people. I also want to mention my late Grandfather who instilled in me a curiosity and love of science from a young age.

I had a great time in the Chen Lab thanks to the friends and colleagues who were with me along the way, particularly Nikola and James who helped me push through the failed experiments to find new avenues to pursue.

And of course Sam – thank you for loving and supporting me in everything that I do.

Chapter 1: Introduction

Contribution acknowledgments

I wrote this chapter with the help of my thesis advisor Professor Jianzhu Chen, PhD.

Major Facilitator Superfamily Domain-Containing 7C

Proliferative Vasculopathy and Hydranencephaly-Hydrocephaly Syndrome

Proliferative Vasculopathy and Hydranencephaly-Hydrocephaly Syndrome (PVHH, OMIM #225790), or Fowler Syndrome, was first described in 1972 as a prenatally lethal disease characterized by a particular vasculopathy in the central nervous system (CNS) and retina (Fowler et al. 1972). Malcolm Fowler and colleagues identified five fetuses within a single family that showed hydranencephaly and hydramnios without any evidence of underlying infectious etiology, ultimately leading him to conclude that the disease origins were likely due to a congenital CNS defect. Due to the failure of proper development of the CNS, the developing embryos would not be able to properly swallow amniotic fluid leading to hydramnios. Similarly, he observed a symmetrical arthrogryposis whereby he concluded the atrophy of muscles and deformity of the joints was secondary to a neurogenic deficit. Microscopic evaluation of the intact developing brain revealed glomeruloid vessels with intracytoplasmic inclusions on nearby cells, which he postulated might be pericytes. Based on his findings, Fowler hypothesized that the syndrome was likely of genetic origin and caused by a "defect in the vascularization of the central nervous parenchyma," resulting in deaths of the fetuses between 26 and 33 weeks gestation.

Since then, numerous additional patients with similar features have been diagnosed (Radio et al. 2018). Fetuses are affected by hydrocephaly, wherein fluid builds up in the brain resulting in ventriculomegaly, and hydranencephaly, marked by absence of the cerebral hemispheres and

replacement by fluid-filled sacs. Until 2010, patients were established pathologically when fetuses died in utero and autopsy revealed a pathognomonic glomeruloid vascular proliferation localized to the CNS. The disease is rare and due to its autosomal recessive inheritance pattern, it was often identified only when a mother would have multiple stillbirths and an underlying etiology was sought. In 2010, Meyer et al. demonstrated a correlation between PVHH and mutations in the gene Major Facilitator Superfamily Domain Containing 7C, or *MFSD7C* (Meyer et al. 2010). They identified three consanguineous Pakistani families who had produced seven fetuses with PVHH and performed a genome-wide linkage scan using single nucleotide polymorphism (SNP) microarrays to identify regions of homozygosity common to all the affected fetal DNA and further narrowed down using microsatellite markers. By comparing DNA obtained by the fetuses against unaffected parents and siblings, they identified a likely region known to contained ten genes, pseudogenes, and proteins. They performed direct sequencing in this region and mutational analysis revealed a shared homozygous missense T430R mutation in exon 7 of *MFSD7C*. This mutation was not present in 646 control genomes that were analyzed. After identifying this gene as the likely culprit for PVHH, they sequenced *MFSD7C* in two additional PVHH fetuses that were nonconsanguineous and of North European origin; one was compound heterozygous for a 6bp deletion and missense mutation, and the other was compound heterozygous for a nonsense and missense mutation.

In 2020, two groups demonstrated that they could recreate a similar phenotype to PVHH in mice by congenitally knocking out the murine *Mfsd7c* (Nguyen et al. 2020, Santander et al. 2020). Nguyen et al. knocked out *Mfsd7c* in mouse embryos by crossing viable mice with heterozygous deletions. They found that global knockout of *Mfsd7c* generally resulted in late-gestation lethality although some pups did survive a few hours past birth. Affected embryos had

smaller heads and inhibited growth of CNS blood vessels across various regions of the brain, with aberrant vascular tips resulting in glomeruloid vessels. Santander et al. further narrowed down the precipitating cause of the CNS defects by using conditional reporters that not only knocked out *Mfsd7c* in select cells but also replaced *Mfsd7c* expression with green fluorescent protein (GFP), allowing them to study the time-course for when Mfsd7c would normally be expressed in the developing mouse brain. They found that Tie2-Cre-expressing *Mfsd7c*-floxed mice, which knocked out Mfsd7c expression and replaced it with GFP in endothelial cells, displayed blood vessels with reduced sprouting and resulted in late embryonic or early postnatal lethality. The GFP expression in brain endothelial cells was first observed at E12.5 and increased until E18.5, at which time the authors noted essentially all CNS endothelium was GFP-positive. Time-course analyses revealed that embryos at E12.5 had morphologically normal brains, and that beginning around E14.5 and further developing until E18.5 the affected embryos had increasing vascular malformations and surrounding tissue necrosis in areas insufficiently vascularized.

Besides this well-described pathological vascularization in the CNS, the establishment of *MFSD7C* mutations as the underlying defect responsible for PVHH has allowed for more patients and fetuses to be diagnosed with this syndrome (De Luca et al. 2020). In the literature, 72 patients have been described with PVHH, six of whom survived past birth (De Luca et al. 2020). Fourteen distinct mutations have been identified among the diagnosed fetuses and three among the patients who have survived postnatally. Most the fetuses and patients (>80%) exhibited hydrocephaly and cerebral glomerular vasculopathy, but the majority of fetuses also showed glomerular vasculopathy in the spine and musculoskeletal changes associated with the fetal akinesia deformation sequence, findings which were completely absent in the patients who survived past birth. Of the six patients from three distinct families who were born and diagnosed, four are already

deceased – two from multiorgan failure (aged 18 and 22) and two from respiratory infections (aged 3 and 4). All of the patients who survived past birth exhibited some degree of developmental delay, and five out of six have seizure disorders. Other than the one patient who does not experience seizures and who has the mildest developmental delay (and was still alive at age 29 as of 2020), all these patients also experience recurrent respiratory infections.

The pathophysiology leading to these recurrent lung infections, however, remains unclear. MFSD7C is highly expressed by alveolar macrophages, a sentinel innate immune cell that detects and counters pathogens within alveoli. An understanding of MFSD7C's function within these cells would help demonstrate how their immune functions might be impaired by mutations within the protein. Although we have not previously examined alveolar macrophages, our lab has extensively studied MFSD7C in cell lines and more peripherally in bone marrow-derived macrophages.

Modulation of cellular metabolism and thermogenesis by MFSD7C

Our group has been working to understand the function of *MFSD7C* in cell lines and via biochemical assays for some time. This gene is also referred to in the literature as Feline leukemia virus subgroup C cellular receptor family, member 2 (*FLVCR2*) or Solute carrier family 49 member A2 (*SLC49A2*). Much of our previous work can be found published in Nature Communications on September 24, 2020 in Volume 11, Issue 4837, doi: 10.1038/s41467-020-18607-1. My contribution to this paper was primarily in helping to study the mouse model from which we derived bone marrow-derived macrophages (BMDMs) and performing experiments that involved these BMDMs, namely the Seahorse and cellular temperature experiments. Our work primarily explored how *MFSD7C* is implicated in metabolic changes within cells.

Energy released from oxidation of carbohydrates and lipids can be used either for driving chemical reactions (anabolism), synthesizing an energy currency (ATP synthesis), or left unused (generating heat). There are a few proteins known to be capable of increasing heat production relative to energy generation, including the well-characterized UCP1 (Jastroch et al. 2010) as well as SERCA1 and SERCA2b (Block et al. 1994, Ikeda et al. 2017). Our lab has demonstrated that MFSD7C (**Introductory Figure I1)**, is similarly able to modulate ATP synthesis to thermogenesis.

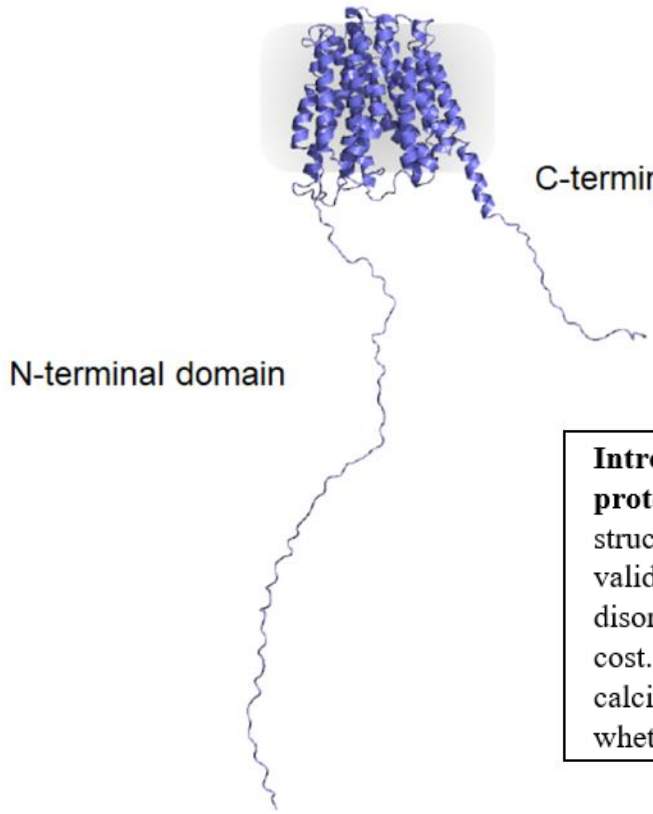

Introductory Figure I1 | Structure of the protein MFSD7C. Although the exact structure remains unknown, it has been validated that the N-terminal domain is disordered and binding it has a high entropic cost. The C-terminal domain resembles a calcium binding domain, but it is unknown whether it actually binds calcium.

The exact mechanism by which MFSD7C achieves thermogenesis remains unknown, but it was demonstrated that the N-terminal domain binds to heme and that this binding is responsible for changes in other protein-protein interactions. As a result, it is important to understand where MFSD7C localizes in order to better characterize which protein-proteins might be formed or

disrupted. An immunoprecipitation experiment revealed that MFSD7C may interact with ATP5H, SERCA2b, and HMOX1, and nearly half of the proteins that were pulled down via co-IP reside in the mitochondria. The localization of the protein to the mitochondria was further supported by a subcellular fractionation experiment which revealed via Western blotting that Mfsd7c in mouse brain, one of the main organs wherein *Mfsd7c* is expressed (Brasier et al. 2004), was only present in the mitochondrial fraction rather than alongside plasma membrane or ER proteins.

Taking into account this localization to the mitochondria, a Seahorse assay examining oxygen consumption and extracellular acidification rates was carried out. The Seahorse assay showed that when MFSD7C was knocked out, cells demonstrated an increased basal rate and an elevated maximal rate of oxygen consumption and extracellular acidification, suggesting global metabolic changes were affected by MFSD7C expression. Furthermore, to assess heme's potential function given the knowledge that it binds to the N-terminal domain, heme was added to both wild-type and knockout cells and it was found that only wild-type cells experienced an increase in basal and maximal oxygen consumption rates in response to heme. The knockout, while already elevated, did not elevate any further when heme was added. This suggested that the metabolic program accomplished by the protein was designed to be modulated by heme, but how the knockout was phenocopying this function remained unclear.

Notably, despite these elevations in oxygen consumption and extracellular acidification, *MFSD7C*-knockout cells did not generate additional ATP relative to the wild-type cells. Instead, the ATP/ADP ratio was ~20% lower in the knockout. This contrast between upregulated extracellular acidification/oxygen consumption rates and lower rates of ATP made us consider that uncoupling might be occurring, but very little uncoupling could be observed via Seahorse assay.

Instead of trying to track the ATP pathway, we instead examined heat generated by using a cellular thermoprobe fluorescent dye. This dye is cell-permeable and capable of reporting on the thermogenic attributes of the cell in which it is contained via fluorescence. We found that the *MFSD7C*-knockout cells demonstrated higher levels of fluorescence consistent with elevated cellular temperatures. Furthermore, this finding could be phenocopied in the wild-type cells via addition of heme. This correlation between heme-treatment to the wild-type and the knockout phenotype itself led us to seek to better characterize how the N-terminus achieves its functions by simply truncating the protein and removing the N-terminal domain altogether. Without the N-terminal domain present on the protein, MFSD7C-positive cells no longer responded to heme.

One additional important finding was a connection between Serca2b and MFSD7C. Specifically, when Serca2b was inhibited with the small molecule thapsigargin, heme-stimulated thermogenesis was abrogated. Because Serca proteins serve as calcium transporters (Ikeda et al. 2017), this indicated that either Serca2b itself or calcium might somehow be implicated in the phenotype; however, deciphering the exact contribution of calcium toward the phenotype has proven difficult.

A notable change in our thinking since the publishing of this paper is the recognition that at least some of the MFSD7C in the cell likely lies on the cell surface. This reinforces the notion that the substrate of the protein, rather than the protein-protein interactions in which it participates, may help drive the previously-described phenotype associated with heme addition and protein knockout. Furthermore, cell signaling and environmental sensing are more likely to be relevant for a transporter located within the plasma membrane. Expression of MFSD7C in alveolar macrophages, immune cells with significant cell-cell communication that reside in a

physiologically niche environment, supports the notion that alveolar macrophages would be a well-suited primary cell type for examining the physiologic role of MFSD7C.

Alveolar macrophages and their environment

When examining MFSD7C expression in knockout mice using GFP recombined to the location of the original gene, Santander et al. noted the presence of GFP in the lungs and surmised it was likely being expressed by alveolar macrophages (Santander et al. 2020). Consistent with this premise, transcriptional analysis of different tissue macrophages supports significantly higher expression of MFSD7C in alveolar macrophages (AMs) versus other macrophages (Gautier et al. 2012). In order to understand why AMs specifically express MFSD7C, it is important to understand their physiologic role as well as the various known differences between AMs and other macrophages.

Development and role in surfactant clearance

Macrophage Overview and Definition of AMs

Macrophages serve a diverse set of roles across numerous tissues, and they are involved not only in innate immunity but also in tissue repair (Bosurgi et al. 2017) and clearance of cellular debris (Herzog et al. 2019). Tissue-resident macrophages arise from varying progenitors in the developing embryo and have been demonstrated to maintain their own populations after birth in several tissues (Yona et al. 2013), but they can also be replaced by blood monocytes (Greenhalgh et al. 2018). Macrophage phenotype and function are affected by both their localized microenvironment as well as their origin (Zhang et al. 2021).

Historically, macrophages were considered to be activated into either the classically-activated M1 or alternatively-activated M2 polarizations, states which were studied by culturing and polarizing macrophages *in vitro* (Mills et al. 2000). M1 macrophages express pro-inflammatory cytokines such as IL-1β and TNF-α, and they are polarized in vitro using lipopolysaccharide (LPS) from bacteria alongside Th1 cytokines such as IFN-γ (Chen at al. 2017). M2 macrophages express anti-inflammatory cytokines such as IL-10 and TGF-β, and they are polarized in vitro using Th2 cytokines such as IL-4 and IL-13 (Gordon et al. 2010). Macrophages can change their polarization in response to the changing needs of the tissue environment, such as switching from a pro-inflammatory M1 to an anti-inflammatory M2 during tissue repair (Novak et al. 2013). It has been demonstrated that macrophages can be repolarized from one phenotype to another with little to no memory of prior polarization (Liu et al. 2020).

Macrophages exposed to bacteria or cytokines *in vivo* often have differing gene and marker expression signatures than those observed when polarizing *in vitro* (Orecchioni et al. 2019). The act of isolating and culturing macrophages *in vitro* itself generates many changes to the macrophage transcriptome (Gosselin et al. 2017). In the tissue microenvironment, different polarization and activation markers of M1 and M2 can exist simultaneously (Orecchioni et al. 2019). Furthermore, high proportions of individual macrophages have been observed to express both M1 and M2 surface markers when observed in certain contexts (Trombetta et al. 2018). As a result, the M1/M2 paradigm is often a less useful model when examining tissue-resident macrophages in their natural microenvironment.

Considering that MFSD7C expression is nearly 100-fold higher in AMs, it is important to characterize what differentiates AMs from other macrophage subsets. AMs can be defined using surface markers (Gautier et al. 2012, Bharat et al. 2016, Gibbings et al. 2017) and by location

within the alveolar airspace (Ogger et al. 2021); they are generally the only macrophage population found in the bronchoalveolar lavage taken from a healthy individual (Svedberg et al. 2019). There are other lung macrophages, such as interstitial macrophages, that have a distinct marker profile from those found in the naïve airway (Bain et al. 2022). Alveolar macrophages express high levels of CD11c, SiglecF, and CD169, while lacking CD11b expression which is unusual for macrophages. During times of inflammation, macrophages with an interstitial phenotype can be found in the airway, and these macrophages express CD11b yet are SiglecF negative. Compared to other macrophages, AMs have unique aspects of development, recruitment, function, and activation.

AM Development, Recruitment, and Maintenance

Prior to birth, AMs (as defined by marker expression) are undetectable in the lung. They appear within the first few days after birth in mice and humans alongside formation of the alveoli and maturation of the pulmonary vasculature (Bharat et al. 2016, Guilliams et al. 2013). Before their appearance, there are two main populations of macrophages residing in the lungs of mice – a $F4/80^{hi}$ $CD11b^{lo}$ population of so-called primitive macrophages that colonizes the lung around E12.5, and a $Ly6C^{hi}$ $CD11b^{hi}$ population of fetal monocytes that colonizes around E16.5. Adoptive transfer experiments identified fetal monocytes, and not primitive macrophages, as the main precursors of AMs. This was further supported by genetic fate mapping experiments wherein tamoxifen-inducible Cre recombinase under different promoters was used to show that yolk sac progenitors provide minimal contribution to AMs (Hoffman et al. 2018)

Consistent with this data, adult Ccr2 knockout mice, which are monocytopenic, still have apparently normal AMs (Hashimoto et al. 2013). Connecting vasculature of such mice to wild-

type mice via parabiosis shows minimal wild-type cellular infiltration into AMs; similar findings were seen using bone-marrow chimeric mice. Moreover, Eguiluz-Garcia et al. demonstrated that lung transplant patients also retain donor AMs when followed over time, suggesting human AMs similarly maintain their own population. However, recent longitudinal experiments in mice have called into question whether the original lineage tracing studies in mice examined AMs in mice after sufficient passage of time. Two separate groups have used alternate reporter mice which suggest that AMs do require replenishing over the life course (Perdiguero et al. 2015, Liu et al. 2019). Byrne et al. also examined lung transplant tissue in humans and found that in their single cell RNAseq experiments (Eguiluz-Garcia et al. had used fluorescence in situ hybridization on a different patient population), the donor AMs were indeed replaced by recipient cells (Byrne et al. 2020). The reason for these conflicting data from experiments in both mice and humans remains unclear, but it may be related to the degree of pathology that occurs across different mouse models, aging over time, and surgical techniques employed.

Following lung injury, the AM population can be affected and cells are sometimes recruited from outside the alveoli to become AMs. Sterile inflammation in mice induced by LPS (Bain et al. 2022) or via diphtheria toxin on AMs expressing diphtheria toxin receptor (Liu et al. 2019) utilizes local proliferation of surviving AMs to repopulate. More significant inflammation as seen in viral influenza (Aegerter et al. 2020) or Sars-Cov-2 infection (Liao et al. 2020) results in monocyte-derived cells repopulating the existing AMs.

AMs Reside in and Recycle Surfactant

Because the alveoli serve as the site of gas exchange, they fulfill a barrier function yet must maintain the delicate thin-walled structures for optimal gas diffusion between air and blood.

Surfactant helps provide this barrier while also preventing alveolar collapse by reducing surface tension at the air-liquid interface (Rodriguez et al. 2014). Alveolar macrophages reside within this surfactant, and they play an integral role helping to recycle it (Malur et al. 2011).

Pulmonary surfactant is a mixture of lipids and proteins, with lipids accounting for 90% of the surfactant by mass (Rodriguez et al. 2014). The exact composition varies between species and physiologic conditions such as temperature (Lang et al. 2005), breathing rate, hibernation (Suri et al. 2012), and pathology (Gunther et al. 1999, Schmidt et al. 2001). The main lipid constituents are phosphatidylcholines (70% of surfactant mass) including dipalmitoylphosphatidylcholine (40%), hydroxylated anionic phospholipids such as phosphatidylglycerol and phosphatidylinositol (10-15% together), and cholesterol (5-8%). The surfactant proteins SP-A, SP-B, SP-C, and SP-D constitute approximately 8.5% of the surfactant mass (Rodriguez et al. 2014). SP-A and SP-D are members of the collectin protein family that bind and eliminate pathogens (Crouch et al. 2001, Johansson et al. 1997, Orgeig et al. 2010). SP-B and SP-C are hydrophobic proteins that embed into surfactant phospholipids and enhance adsorption of molecules into the air-liquid interface, helping to stabilize it (Possmayer et al. 2010).

Surfactant is produced by alveolar type II pneumocytes, which assemble it into specialized membranous organelles called lamellar bodies after which it is secreted into the alveoli (Perez-Gil et al. 2010). They are stimulated to release it via mechanical stretching that occurs during inspiration, where a single stretch can result in elevation of cytoplasmic calcium concentration (Frick et al. 2004). However, there is also evidence that paracrine signaling of ATP from type I pneumocytes can cause surfactant exocytosis by type II pneumocytes (Patel et al. 2005). In the airspace, surfactant can become oxidized or otherwise chemically altered (Olmeda et al. 2017). Clearance of cellular debris and healthy or altered surfactant is accomplished via a variety of

mechanisms, including expulsion from the airway, uptake by type II pneumocytes, and degradation by AMs. In healthy lungs, mucociliary transport up the airways is estimated to clear approximately 15% of the surfactant (Pattenazzo et al. 1988), 65% is recycled by pneumocytes, and 20% is cleared by AMs (Rider et al. 1992). During lung injury, increased vascular permeability may allow some surfactant components to leak into the bloodstream (Cross et al. 2011). The turnover time for surfactant is quite rapid, with 10% recycled each hour (Wright et al. 1990).

Eliminating AM clearance of surfactant leads to progressive deposition of lipids and proteins, resulting in acute respiratory distress syndrome and pulmonary alveolar proteinosis (PAP) (Forbes et al. 2007). PAP is characterized by lipid and protein accumulation in the alveolar space, and it can be phenotypically elicited by altering maturation of AMs by knocking out granulocyte-macrophage colony stimulating factor (GM-CSF) (Malur et al. 2011) or eliminating downstream transcription of Bach2 (Nakamura et al. 2013). Alternately, preventing uptake of surfactant by type II pneumocytes results in activation of AMs, resulting in inflammation and emphysema (Ikegami et al. 2005).

Alveolar macrophages as innate immune sentinels

AM Activation and Resolution

AMs act as sentinel immune cells within the lung, using phagocytosis to defend against bacterial infections and secreting cytokines to recruit more immune cells as needed. AMs move between alveoli to phagocytose bacteria, so migration is a critical component of bacterial clearance (Neupane et al. 2020). This migration appears to be dependent on CD11a, and it is critical in part because there is only one AM for every three alveoli (Kirby et al. 2009). However, Westphalen et

al. demonstrated that there is an AM subpopulation that adheres to the alveolar wall via Cx43 which remains sessile and forms gap junction channels with the epithelium (Westphalen et al. 2014). AMs are vital for protection against pathology from a variety of pathogens, including *Staphylococcus aureus*, *Klebsiella pneumonia*, and influenza (Martin et al. 2011, Brough-Holub et al. 1997, Narasaraju et al. 2011); without AMs, the lung injuries resulting from these infections are more severe and survival is reduced.

However, they can also support pathology in specific contexts such as *Mycobacterium tuberculosis* infection (Cohen et al. 2018), which infects AMs intracellularly, or in ventilator-induced injury whereby they increase inflammation unnecessarily (Eyal at al. 2007). Viral infection can induce long-lasting memory AMs that are more primed to recruit neutrophils (Shibata et al. 2020), which may be protective or pathological depending on subsequent infections, and favorable vs dysfunctional effects on AMs after initial infection seem to be dependent on the particular model employed (Hou et al. 2021).

Fine-tuning AM response to bacteria is critical in part because bacteria are constantly infiltrating into this space (Huffnagle et al. 2017). Over fifty studies have identified bacteria in the lower airways after the first identification of a lung microbiome in healthy subjects in 2010 (Hilty et al. 2010). This microbiome seems to be defined by immigration, elimination, and replication rates (Dickson et al. 2015). Dickson et al. describe how subclinical microaspiration is the primary source of microbial immigration (Dickson et al. 2015), and elimination is accomplished via mucociliary clearance, cough, and immune defenses. Inflammation itself affects regional growth conditions, with vascular leak providing a multitude of nutrients. The result is an ever-changing catalog of bacteria in varying quantities, many of which pose no threat of virulence but rather are

protective against pathogens, inhibit an exaggerated inflammatory response, and reduce asthma and allergy (Stavropoulou et al. 2021).

Separate from the microbiome, AMs themselves can suppress atopic diseases such as asthmatic lung inflammation (Zaslona et al. 2014). When using a house dust mite allergen model in mice, depleting AMs results in exacerbated type II inflammation via IL-13 (Mathie et al. 2014). AMs themselves produce TGF-β, which can help control allergic reactions (Branchett et al. 2021). Similarly, they can help clear allergens themselves via phagocytosis (Zhou et al. 2018). AMs also interact with other immune cells, and they can promote development of regulatory T cells via antigen presentation (Soroosh et al. 2013) and production of retinoic acid after apoptotic cell engulfment (Miki et al. 2021).

Mechanisms of Bacterial Killing

AMs utilize the same methods for killing bacteria as do other macrophages. Macrophages recognize bacteria via pattern recognition receptors (PRRs), which identify the presence of specific microbe-associated molecular patterns. Opsonization of bacteria is facilitated by proteins including SP-A, SP-D, and the mannose-binding lectin, as well as various complement components (Weiss et al. 2015). If the pathogen has infected the host before or if it lingers for sufficient time, antibodies will be produced which can also opsonize the bacteria. Opsonized bacteria can be phagocytosed via opsonic receptors such as C receptors or Fcγ receptors, while non-opsonized bacteria can be taken up by non-opsonic receptors such as scavenger receptors, C-type lectins, lectin-like recognition molecules, and mannose receptors (Uribe-Querolet al. 2017). Toll-like receptors (TLRs), which recognize microorganisms and transduce danger signals, do not

function as phagocytic receptors but can cooperate with non-opsonic receptors to increase phagocytosis (Kawai et al. 2011, Iwasaki et al. 2015).

After receptor engagement, membrane remodeling and changes to the actin cytoskeleton occur, leading to the formation of pseudopods (Kobayashi et al. 1998). Within a few minutes, the target microorganism is surrounded and the membrane protrusions fuse to create the new phagosome (Dart et al. 2012). Over the next 30 minutes, the phagosome matures into a phagolysosome (Allard et al. 2018). The phagolysosome has a variety of mechanisms that contribute toward microorganismal killing and degradation, including their acidity, degradative enzymes, and reactive chemical species. The pH in the mature phagolysosome reaches pH 5 by funneling protons into the organelle using the proton pump V-ATPase, which hydrolyzes cytosolic ATP (Marshansky et al. 2008). The low pH both prevents the use of various nutrients by the microbe (Jabado et al. 2000) and activates host hydrolytic enzymes. The protons also allow for symport divalent cation transport out of the phagolysosome via NRAMP-1, which sequesters Fe^{2+}, Zn^{2+}, and Mn^{2+} out of the phagolysosome and helps to inhibit microbial growth (Cellier et al. 2007). NADPH oxidase on the phagosomal membrane transfers electrons from cytosolic NADPH to oxygen to generate superoxide inside the phagosome (Babior et al. 2004). This enzyme is defective in patients with chronic granulomatous disease, resulting in recurrent infections (Roos et al. 2016). Although not specific to phagolysosomes, macrophages responding to inflammatory signals can also produce nitric oxide radicals in the cytoplasm which can then diffuse across the phagolysosomal membrane and accumulate inside the phagosome. Nitric oxide radicals can react with superoxide radicals in the phagolysosome to form peroxynitrite, which can modify proteins and DNA of the contained microbes (Grosser et al. 2016).

AMs also eliminate bacteria by helping organize the recruitment of additional immune cells, including neutrophils and monocyte-derived macrophages. After detecting bacteria, macrophages secrete IL-8 in humans (KC in mice) alongside prostaglandins and leukotrienes to recruit and activate neutrophils, which then secrete MCP-1 and MIP to recruit monocyte-derived macrophages (Weiss et al. 2015). All three cell populations secrete TNF-alpha, IL-1β, IL-6, IL-12, IL-18, and IL-23 to continue inflammation until counteracted by elimination of the bacteria and/or other anti-inflammatory mediators.

Taking into account that patients with MFSD7C mutations who survive past birth have recurrent lung infections, and MFSD7C is highly expressed within the AMs that act as the sentinel innate immune cells within the alveoli, it seems likely that MFSD7C is important for the proper immune response of AMs. However, it is also possible that the recurrent lung infections are secondary to increased aspiration risk or other behaviors more directly related to the better-defined CNS abnormalities.

It is unknown whether mutations in MFSD7C prevent appropriate AM development or maintenance, impact other AM functions such as surfactant clearance, or if they more specifically affect either AM activation or some specific mechanism of bacterial killing. If such effects are observed, it is reasonable to hypothesize that they may be related to metabolic changes within AMs that may be similar to those our lab has previously observed in cell lines when MFSD7C is knocked out. For example, reduced ATP levels may be observed and might decrease AM ability to phagocytose bacteria or acidify their phagolysosomes. Identification of the substrate for MFSD7C would help demonstrate the most likely pathways by which MFSD7C impacts AMs.

References

Aegerter, H. *et al.* (2020) 'Influenza-induced monocyte-derived alveolar macrophages confer prolonged antibacterial protection', *Nature Immunology*, 21(2), pp. 145–157. doi:10.1038/s41590-019-0568-x.

Al-Murshedi, F. *et al.* (2020) 'Variability of non-lethal Fowler syndrome phenotype associated with FLVCR2 variants', *Clinical Genetics*, 98(5), pp. 520–521. doi:10.1111/cge.13838.

Brasier, G. *et al.* (2004) 'Novel hexad repeats conserved in a putative transporter with restricted expression in cell types associated with growth, calcium exchange and homeostasis', *Experimental Cell Research*, 293(1), pp. 31–42. doi:10.1016/j.yexcr.2003.10.002.

Cellier, M.F., Courville, P. and Campion, C. (2007) 'Nramp1 phagocyte intracellular metal withdrawal defense', *Microbes and Infection*, 9(14), pp. 1662–1670. doi:10.1016/j.micinf.2007.09.006.

Chen, Y. and Zhang, X. (2017) 'Pivotal regulators of tissue homeostasis and cancer: macrophages', *Experimental Hematology & Oncology*, 6(1), p. 23. doi:10.1186/s40164-017-0083-4.

Dart, A.E. *et al.* (2012) 'The motor protein myosin 1G functions in FcγR-mediated phagocytosis', *Journal of Cell Science*, 125(Pt 24), pp. 6020-6029. doi:10.1242/jcs.109561.

De Andrade Costa, A. *et al.* (2022) 'RNA sequence analysis reveals ITGAL/CD11A as a stromal regulator of murine low-grade glioma growth', *Neuro-Oncology*, 24(1), pp. 14–26. doi:10.1093/neuonc/noab130.

Dickson, R.P. and Huffnagle, G.B. (2015) 'The Lung Microbiome: New Principles for Respiratory Bacteriology in Health and Disease', *PLOS Pathogens*, 11(7), p. e1004923. doi:10.1371/journal.ppat.1004923.

Dickson, R.P. *et al.* (2015) 'Spatial Variation in the Healthy Human Lung Microbiome and the Adapted Island Model of Lung Biogeography', *Annals of the American Thoracic Society*, 12(6), pp. 821-830. doi:10.1513/AnnalsATS.201501-029OC.

Duffy, S.P. *et al.* (2010) 'The Fowler Syndrome-Associated Protein FLVCR2 Is an Importer of Heme', *Molecular and Cellular Biology*, 30(22), pp. 5318–5324. doi:10.1128/MCB.00690-10.

Eyal, F.G. et al. (2007) 'Reduction in alveolar macrophages attenuates acute ventilator induced lung injury in rats', Intensive Care Medicine, 33(7), pp. 1212-1218. doi:10.1007/s00134-007-0651-x.

Frick, M. *et al.* (2001) 'Secretion in Alveolar Type II Cells at the Interface of Constitutive and Regulated Exocytosis', *American Journal of Respiratory Cell and Molecular Biology*, 25(3), pp. 306-315. doi:10.1165/ajrcmb.25.3.4493.

Gautier, E.L. *et al.* (2012) 'Gene-expression profiles and transcriptional regulatory pathways that underlie the identity and diversity of mouse tissue macrophages', *Nature Immunology*, 13(11), pp. 1118-1128. doi:10.1038/ni.2419

Grosser, M.R. *et al.* (2016) 'Regulatory Requirements for Staphylococcus aureus Nitric Oxide Resistance', *Journal of Bacteriology*, 198(15), pp. 2043–2055. doi:10.1128/JB.00229-16.

Günther, A. *et al.* (1999) 'Surfactant abnormalities in idiopathic pulmonary fibrosis, hypersensitivity pneumonitis and sarcoidosis', *The European Respiratory Journal*, 14(3), pp. 565–573. doi:10.1034/j.1399-3003.1999.14c14.x.

Hashimoto, D. *et al.* (2013) 'Tissue resident macrophages self-maintain locally throughout adult life with minimal contribution from circulating monocytes', *Immunity*, 38(4), pp. 792-804. doi:10.1016/j.immuni.2013.04.004.

Ikeda, K. *et al.* (2017) 'UCP1-independent signaling involving SERCA2b-mediated calcium cycling regulates beige fat thermogenesis and systemic glucose homeostasis', *Nature Medicine*, 23(12), pp. 1454–1465. doi:10.1038/nm.4429.

Ikegami, M. *et al.* (2005) 'Surfactant protein D influences surfactant ultrastructure and uptake by alveolar type II cells', *American Journal of Physiology-Lung Cellular and Molecular Physiology*, 288(3), pp. L552-L561. doi:10.1152/ajplung.00142.2004.

Jastroch, M. *et al.* (2010) 'Mitochondrial proton and electron leaks', *Essays in Biochemistry*, 47, pp. 53–67. doi:10.1042/bse0470053.

Kawai, T. and Akira, S. (2011) 'Toll-like Receptors and Their Crosstalk with Other Innate Receptors in Infection and Immunity', *Immunity*, 34(5), pp. 637–650. doi:10.1016/j.immuni.2011.05.006.

Kvarnung, M. *et al.* (2016) 'Mutations in FLVCR2 associated with Fowler syndrome and survival beyond infancy: FLVCR2 mutations, pediatric phenotype', *Clinical Genetics*, 89(1), pp. 99–103. doi:10.1111/cge.12565.

Liao, M. *et al.* (2020) 'Single-cell landscape of bronchoalveolar immune cells in patients with COVID-19', *Nature Medicine*, 26(6), pp. 842–844. doi:10.1038/s41591-020-0901-9.

Liu, S.X. *et al.* (2020) 'Trajectory analysis quantifies transcriptional plasticity during macrophage polarization', *Scientific Reports*, 10(1), p. 12273. doi:10.1038/s41598-020-68766-w.

Lopez-Rodriguez, E. and Pérez-Gil, J. (2014) 'Structure-function relationships in pulmonary surfactant membranes: From biophysics to therapy', *Biochimica et Biophysica Acta (BBA) - Biomembranes*, 1838(6), pp. 1568–1585. doi:10.1016/j.bbamem.2014.01.028.

Malur, A. *et al.* (2011) 'Lentivirus-ABCG1 instillation reduces lipid accumulation and improves lung compliance in GM-CSF knock-out mice', *Biochemical and Biophysical Research Communications*, 415(2), pp. 288–293. doi:10.1016/j.bbrc.2011.10.043.

Marshansky, V. and Futai, M. (2008) 'The V-type H+-ATPase in vesicular trafficking: targeting, regulation and function', *Current Opinion in Cell Biology*, 20(4), pp. 415–426. doi:10.1016/j.ceb.2008.03.015.

Martin F.J. *et al.* (2011) 'Participation of CD11c+ Leukocytes in Methicillin-Resistant Staphylococcus aureus Clearance from the Lung', *Infection and Immunity*, 79(5): pp. 1898-1904. doi:10.1128/IAI.01299-10.

McCowan, J. *et al.* (2021) 'The transcription factor EGR2 is indispensable for tissue-specific imprinting of alveolar macrophages in health and tissue repair', *Science Immunology*, 6(65), eabj2132. doi:10.1126/sciimmunol.abj2132.

Meyer, E. *et al.* (2010) 'Mutations in FLVCR2 Are Associated with Proliferative Vasculopathy and Hydranencephaly-Hydrocephaly Syndrome (Fowler Syndrome)', *The American Journal of Human Genetics*, 86(3), pp. 471–478. doi:10.1016/j.ajhg.2010.02.004.

Mills, C.D. *et al.* (2000) 'M-1/M-2 Macrophages and the Th1/Th2 Paradigm', *The Journal of Immunology*, 164(12), pp. 6166–6173. doi:10.4049/jimmunol.164.12.6166.

Mould, K.J. *et al.* (2019) 'Single cell RNA sequencing identifies unique inflammatory airspace macrophage subsets', *JCI Insight*, 4(5), p. e126556. doi:10.1172/jci.insight.126556.

Nakamura, A. *et al.* (2013) 'Transcription repressor Bach2 is required for pulmonary surfactant homeostasis and alveolar macrophage function', *Journal of Experimental Medicine*, 210(11), pp. 2191-2204. doi:10.1084/jem.20130028.

Neupane, A.S. *et al.* (2020) 'Patrolling Alveolar Macrophages Conceal Bacteria from the Immune System to Maintain Homeostasis', *Cell*, 183(1), pp. 110-125.e11. doi:10.1016/j.cell.2020.08.020.

Novak, M.L. and Koh, T.J. (2013) 'Macrophage phenotypes during tissue repair', *Journal of Leukocyte Biology*, 93(6), pp. 875–881. doi:10.1189/jlb.1012512.

Olmeda, B., Martínez-Calle, M. and Pérez-Gil, J. (2017) 'Pulmonary surfactant metabolism in the alveolar airspace: Biogenesis, extracellular conversions, recycling', *Annals of Anatomy - Anatomischer Anzeiger*, 209, pp. 78–92. doi:10.1016/j.aanat.2016.09.008.

Orecchioni, M. *et al.* (2019) 'Macrophage Polarization: Different Gene Signatures in M1(LPS+) vs. Classically and M2(LPS–) vs. Alternatively Activated Macrophages', *Frontiers in Immunology*, 10, p. 1084. doi:10.3389/fimmu.2019.01084.

Orgeig, S. *et al.* (2010) 'Recent advances in alveolar biology: Evolution and function of alveolar proteins', *Respiratory physiology & neurobiology*, 173(0), pp. S43–S54. doi:10.1016/j.resp.2010.04.023.

Patel, A.S. *et al.* (2005) 'Paracrine stimulation of surfactant secretion by extracellular ATP in response to mechanical deformation', *American Journal of Physiology-Lung Cellular and Molecular Physiology*, 289(3), pp. L489–L496. doi:10.1152/ajplung.00074.2005.

Perdiguero, E.G. *et al.* (2015) 'Tissue-resident macrophages originate from yolk-sac-derived erythro-myeloid progenitors', *Nature*, 518(7540), pp. 547-551. doi:10.1038/nature13989.

Possmayer, F. *et al.* (2010) 'Recent advances in alveolar biology: Some new looks at the alveolar interface', *Respiratory Physiology & Neurobiology*, 173, pp. S55–S64. doi:10.1016/j.resp.2010.02.014.

Perez-Gil, J. and Weaver, T.E. (2010) 'Pulmonary Surfactant Pathophysiology: Current Models and Open Questions', *Physiology*, 25(3), pp. 132-141. doi:10.1152/physiol.00006.2010.

Radio, F.C. *et al.* (2018) 'Proliferative vasculopathy and hydranencephaly-hydrocephaly syndrome or Fowler syndrome: Report of a family and insight into the disease's mechanism', *Molecular Genetics & Genomic Medicine*, 6(3), pp. 446–451. doi:10.1002/mgg3.376.

Rider, E.D. *et al.* (1992) 'Localization of alveolar surfactant clearance in rabbit lung cells', *American Journal of Physiology*, 263(2 Pt 1), pp. L201-L209. doi:10.1152/ajplung.1992.263.2.L201.

Santander, N. *et al.* (2020) 'Lack of Flvcr2 impairs brain angiogenesis without affecting the blood-brain barrier', *Journal of Clinical Investigation*, 130(8), pp. 4055-4068. doi:10.1172/JCI136578.

Shibata, T. *et al*. (2020) 'Respiratory syncytial virus infection exacerbates pneumococcal pneumonia via Gas6/Axl-mediated macrophage polarization', *Journal of Clinical Investigation*, 130(6), pp. 3021-3037. doi:10.1172/JCI125505.

Soroosh, P *et al*. (2013) 'Lung-resident tissue macrophages generate Foxp3+ regulatory T cells and promote airway tolerance', *Journal of Experimental Medicine*, 210(4), pp. 775-788. doi:10.1084/jem.20121849.

Stavropoulou, E. *et al.* (2021) 'Unraveling the Interconnection Patterns Across Lung Microbiome, Respiratory Diseases, and COVID-19', *Frontiers in Cellular and Infection Microbiology*, 10, p. 619075. doi:10.3389/fcimb.2020.619075.

Svedberg, F.R. *et al.* (2019) 'The lung environment controls alveolar macrophage metabolism and responsiveness in type 2 inflammation', *Nature Immunology*, 20(5), pp. 571–580. doi:10.1038/s41590-019-0352-y.

Weiss, G. and Schaible, U.E. (2015) 'Macrophage defense mechanisms against intracellular bacteria', *Immunological Reviews*, 264(1), pp. 182–203. doi:10.1111/imr.12266.

Westphalen, K. *et al.* (2014) 'Sessile alveolar macrophages communicate with alveolar epithelium to modulate immunity', *Nature*, 506(7489), pp. 503-506. doi:10.1038/nature12902.

Zasłona, Z. *et al.* (2014) 'Resident Alveolar Macrophages Suppress, whereas Recruited Monocytes Promote, Allergic Lung Inflammation in Murine Models of Asthma', *The Journal of Immunology*, 193(8), pp. 4245–4253. doi:10.4049/jimmunol.1400580.

Zhang, C., Yang, M. and Ericsson, A.C. (2021) ‘Function of Macrophages in Disease: Current Understanding on Molecular Mechanisms’, *Frontiers in Immunology*, 12, p. 620510. doi:10.3389/fimmu.2021.620510.

Zhou, Y. *et al.* (2018) ‘Mannose receptor modulates macrophage polarization and allergic inflammation through miR-511-3p’, *Journal of Allergy and Clinical Immunology*, 141(1), pp. 350-364. doi:10.1016/j.jaci.2017.04.049.

Chapter 2: Alveolar macrophages lacking *Mfsd7c* demonstrate impaired bacterial killing that can be corrected via glucose supplementation

---

Contribution acknowledgments

I wrote this chapter, performed experiments and interpreted the data with the help of Nikola A. Ivica and my thesis advisor Professor Jianzhu Chen.

Abstract

MFSD7C mutations in humans cause Fowler syndrome, a disorder that is generally prenatally lethal, but patients who survive into infancy and beyond are frequently plagued by recurrent respiratory infections. Here we show that a myeloid-specific Mfsd7c knockout results in a deficient ability of mouse alveolar macrophages to combat infections with the bacteria *Mycobacterium smegmatis*, despite an increased inflammatory response by neutrophils. Using transcriptomics, we present evidence that not only are phagocytosis and bacterial killing impaired but that genes associated with lipid catabolism are downregulated while those associated with glycolysis are upregulated. This signature is rather unusual for alveolar macrophages, which are much less prone to glycolysis than other tissue-resident macrophages. Administration of glucose into the usually glucose-starved alveoli alleviates the bacterial-killing deficiency seen in Mfsd7c-knockout alveolar macrophages. Infection of the peritoneum, which generally has glucose levels similar to the blood and significantly higher than those in the alveoli, demonstrates no impairment of Mfsd7c-knockout peritoneal macrophages.

Introduction

Our lab has established an intricate model for how MFSD7C modulates thermogenesis and metabolism *in vitro*, but we have had difficulty demonstrating that the interaction of heme and MFSD7C, or even knockout cells themselves, have any major effect in vivo. We have previously focused mostly on thermogenic effects since we found those to be the most remarkable and potentially therapeutic, but MFSD7C originally caught our interest as a significant tissue-specific marker of alveolar macrophages (AMs).

Establishing that Mfsd7c$^{-/-}$ alveolar macrophages indeed have an impaired bacterial killing phenotype will help us to begin to correlate how the metabolic phenotype we already understand, and which will presumably be at play in these cells to some extent, might exert its influence over other pathways and functions of the cell. Furthermore, infections of the lung can be extremely serious and are a common cause of mortality – today, the COVID pandemic continues to cause significant morbidity even two years after quarantines were first initiated. Identifying pathways involved in host-pathogen interactions will help us to better identify weaknesses in our own systems that we might seek to modulate therapeutically.

Results and Discussion

Mfsd7c in alveolar macrophages increases bacterial killing

In order to investigate the observed lung infection propensity of patients with mutations in *Mfsd7c*, we utilized a mouse model with a myeloid-specific LysM-Cre knockout of the protein (**Supplemental Figure S1**) which results in a deleted exon 2 and early stop codon as described in our previous paper (Li et al. 2020). For the rest of this paper, we will refer to these mice as 7c$^{-/-}$ mice even though the knockout is only present in the myeloid compartment.

Pulmonary infections are some of the most common infections seen in humans and are particularly common in patients with neurological impairment, so we thought it possible that these patients might have global immune deficiencies that just so happen to be frequently recognized as lung infections. As one method to examine this possibility, we performed a series of immunophenotyping experiments wherein we looked at some of the main immune compartments in the mouse to see if any obvious differences emerged within cell counts or markers. Specifically, we used flow cytometry to examine B cells, CD4+ vs CD8+ T cells, NK cells, granulocytes, and macrophages expressing markers for M1 (CD80) vs M2 (CD163) polarization (flow cytometry scheme depicted in **Supplemental Figure S2**). We could not identify any obvious aberrations in the lymph node (**Supplemental Figure S3**), bone marrow (**Supplemental Figure S4)**, spleen (**Supplemental Figure S5)**, or in the blood (**Supplemental Figure S6)**. Each of these compartments demonstrated similar cell proportions and markers for both $7c^{FL/FL}$ and $7c^{-/-}$ mice.

We next considered that because of its established impact on metabolism and ATP levels, it is possible that $7c^{-/-}$ cells need to be stressed in order to exhibit their deficiencies. Phagocytosis is an energy intensive process requiring ATP (Chandak et al. 2010), so we reasoned that these cytoskeletal rearrangements might be most likely to exacerbate a metabolic abnormality. However, despite our previously having observed metabolic alterations in a variety of cell lines and in bone marrow-derived macrophages, we could not demonstrate a significant phagocytic impairment using either THP-1 cells (**Supplemental Figure S7**) nor bone marrow-derived macrophages (**Supplemental Figure S8)**.

Our attention thus fixed on the alveolar macrophage, which we further characterized as both expressing *7c* and having it knocked out in the $7c^{-/-}$ mice (**Supplemental Figure S9**). In consideration of how best to challenge this macrophage, we reasoned that an intracellular bacteria

would represent the broadest variety of challenges for the AM to counter. We selected *Mycobacterium smegmatis,* often used as a model organism for *Mycobacterium tuberculosis,* as a relatively easy-to-use bacteria in the laboratory setting with next to no virulence in humans that may still pose some difficulty to clear from the lungs.

Using intratracheal injections on anesthetized mice, we instilled $5x10^6$ bacteria into each mouse's lungs and sacrificed the mice after 24 hours. Bronchoalveolar lavages (BALs) were then performed, the BALs centrifuged, and the cells that were recovered were then analyzed via flow cytometry (**Figure 1A**). We found that AMs were significantly reduced in number and granulocytes significantly elevated in the *7c*$^{-/-}$ mice **(Figure 1B)**. A fraction of the supernatant from each BAL centrifugation was taken and plated on agar with Hygromycin B, an antibiotic that our strain of *M. smegmatis* is resistant to, in order to quantify the levels of extracellular bacteria. Similarly, a fraction of the cells recovered were incubated with gentamicin for 1 hour in order to kill any residual extracellular bacteria, then those cells were lysed to quantify the levels of intracellular bacteria. We found there were significantly elevated quantities of intracellular bacteria residing in the *7c*$^{-/-}$ cells relative to the floxed controls, but we did not see a significant difference in the quantity of supernatant bacteria that were grown.

We then examined the time-course through which these differences develop (**Figure 1C**), looking at BALs from mice 4, 8, and 12 hours post-injection. BALs taken from *7c*$^{-/-}$ mice 4 hours post-injection tend to have lower quantities of AMs, increased numbers of granulocytes, and elevated intracellular bacteria than the floxed controls, and these differences become more exaggerated over time.

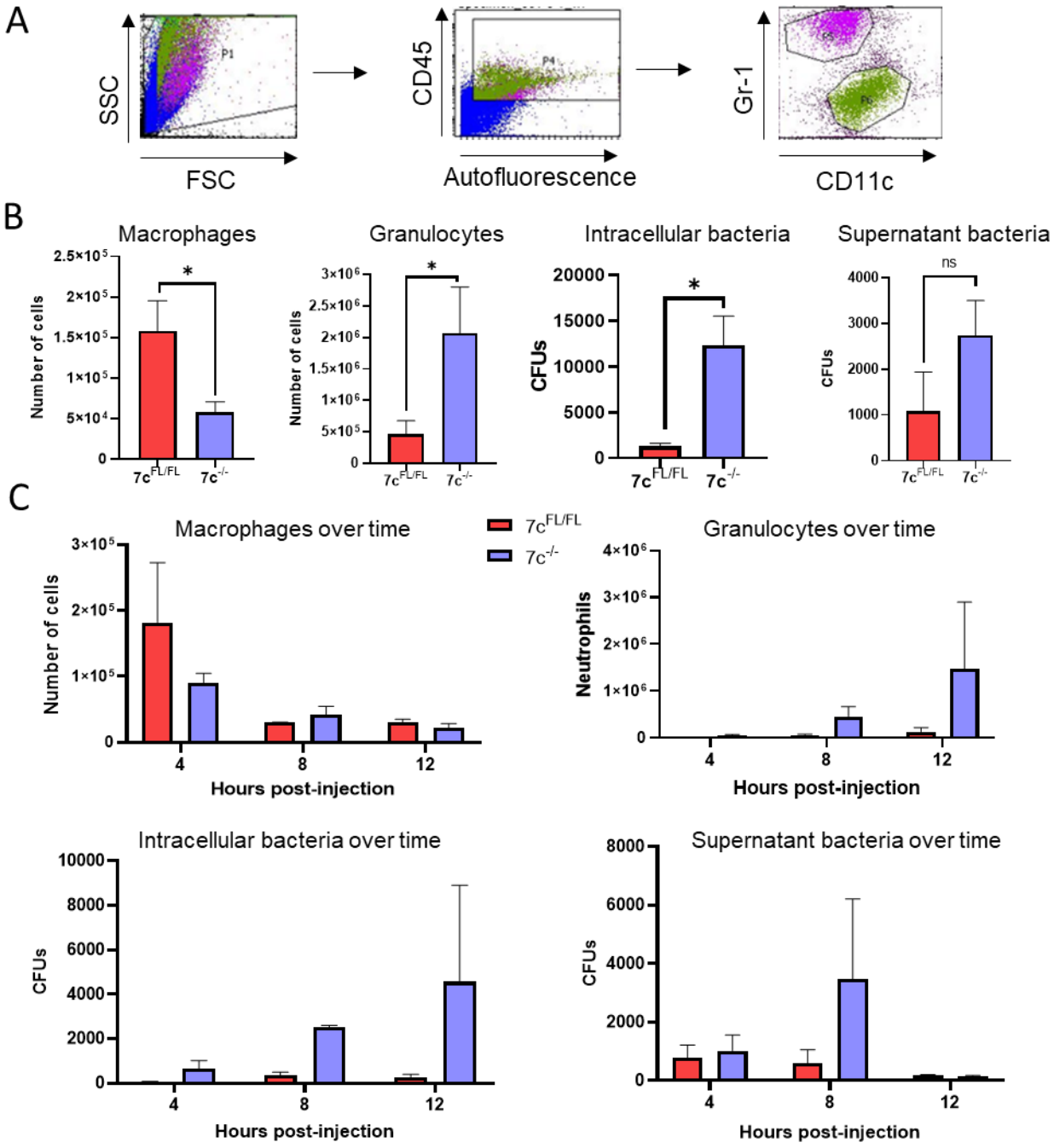

Figure 1 | 7c-deficient AMs demonstrate impaired bacterial killing and increased neutrophil recruitment. **A)** Flow cytometry gating strategy for distinguishing AMs and granulocyte populations from BALs. **B)** AM and granulocyte numbers were obtained 24 hours after intratracheal injection (5 mice per group), and both intracellular and supernatant CFUs of *M. smegmatis* were counted. Macrophage, granulocyte, and intracellular bacteria demonstrate significant (*) differences depending on 7c status (p-values = 0.0033, 0.0317, and 0.0121, respectively; ns = not significant). **C)** Differences between AM and granulocyte numbers, as well as intracellular vs supernatant bacteria, adjust over time. BALs taken 4, 8, and 12 hours post-injection with 3 7c-floxed and 2-3 7c-deficient mice per timepoint.

Mfsd7c in alveolar macrophages suppresses inflammation and neutrophilic infiltration

We next considered the mechanism by which such significant increases in inflammation as measured by neutrophil infiltration might occur. One possibility is that the *7c*$^{-/-}$ mice had an altered vascular permeability; as previously discussed, *7c* knockout in developing neural endothelial cells results in malformed vessels with altered characteristics. Furthermore, an altered vascular permeability might result in BALs uncharacteristic of the actual alveolar environment if the *7c*$^{-/-}$ mice allow for easier rupture of weakened vessels.

BAL supernatant samples taken from previously examined mice were analyzed for their cytokine profiles (**Supplemental Figure S10**), and they revealed that IFN-gamma is significantly downregulated and Cxcl1 is significantly upregulated in *7c*$^{-/-}$ mice (**Figure 2A**). IFN-gamma is an important cytokine for combating intracellular pathogens, while Cxcl1 is a major chemoattractant for neutrophils. This supported the notion that the observed changes in neutrophils in our BAL samples were truly indicative of an alveolar environment with heightened neutrophil recruitment. To further demonstrate this, we recreated the 24-hour infection phenotype but rather than performing BALs on the mouse lungs, we fixed them in formalin and examined the histology representative of the observed phenotype (**Figure 2B, C**). These specimens (**Supplemental Figure S11**) further indicated that neutrophils were being recruited to *7c*$^{-/-}$ lungs in high quantities.

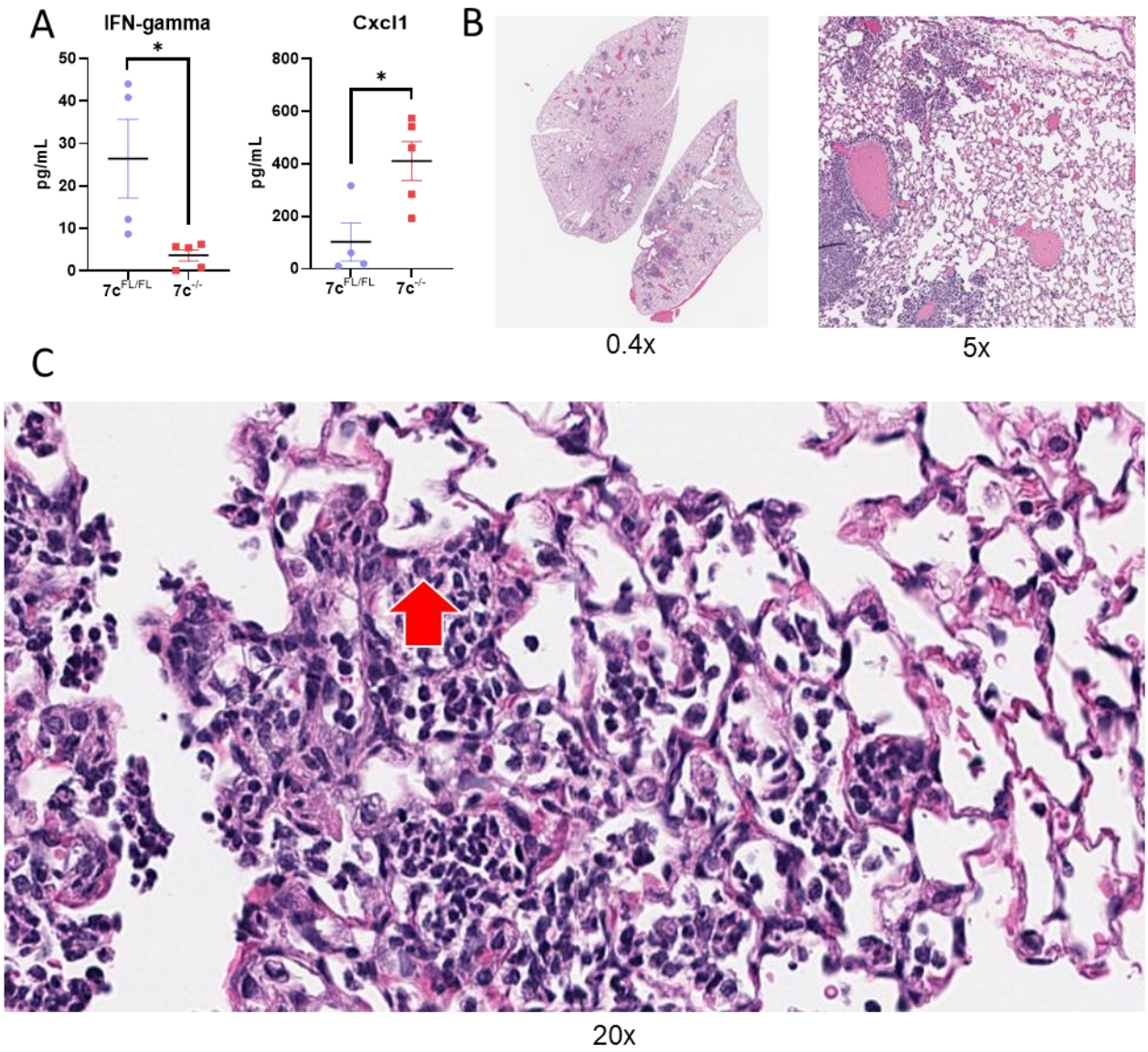

Figure 2 | Alveoli of mice with 7c-deficient AMs have an altered cytokine profile and increased neutrophilic infiltration 24 hours post-infection. A) IFN-gamma is decreased ($p = 0.0287$) and Cxcl1 is elevated ($p = 0.0223$) in BAL samples obtained 24 hours post-injection (4 mice for 7c-floxed and 5 mice for 7c-deficient). **B)** Histology of lungs taken from a mouse with 7c-deficient AMs 24 hours-post injection shows regions of leukocytic infiltration at 0.4x (left) and 5x (right) magnification. The same lungs are examined at 20x (**C**) to validate that leukocytes are polymorphonuclear; one granulocyte is identified above the red arrow.

We were somewhat surprised to find such a significant infiltration of neutrophils in *7c*$^{-/-}$ mice considering that the intracellular CFUs are also significantly elevated in these mice (and thus not being adequately killed by infiltrating neutrophils). While this may be due to the inability of

neutrophils to help kill intracellular pathogens within a macrophage, a different possibility that we considered is that the neutrophils also have an impaired killing phenotype due to their usual expression of LysM; they would therefore also have *7c* knocked out and potentially develop an impaired killing phenotype. We examined this possibility that neutrophil killing of *M. smegmatis in vitro* was impaired (**Supplemental Figure S12**), but found similar levels of bacterial killing by $7c^{FL/FL}$ and $7c^{-/-}$ granulocytes in the assay we performed.

Mfsd7c expression affects phagolysosomal, lipid-processing, and glycolytic genes

Having established that $7c^{-/-}$ mice recreate the observed Fowler Syndrome propensity for pulmonary infections, we next set out to identify what might be causing this. RNAseq was performed analyzing three $7c^{-/-}$ and three $7c^{FL/FL}$ batches of AMs from BALs. We chose to examine uninfected AMs rather than infected AMs because we supposed the number of confounding factors for infected AMs (any preexisting differences prior to infection, differences that occur specifically during infection, and differences resulting from the altered inflammatory landscape of the infected lungs) would make them far more difficult to analyze. We chose to characterize AMs taken directly from lavages rather than first sorting the cells because we were concerned that the sorting processing would have significant effects on the AM transcripts. Furthermore, we knew that lavages were >90% AMs and could confirm this to be the case by taking a small fraction out of each sample we submitted.

HiSeq sequencing using 40BP single-end reads was performed and the resulting data normalized and clustered according to most differentially expressed genes **(Supplemental**

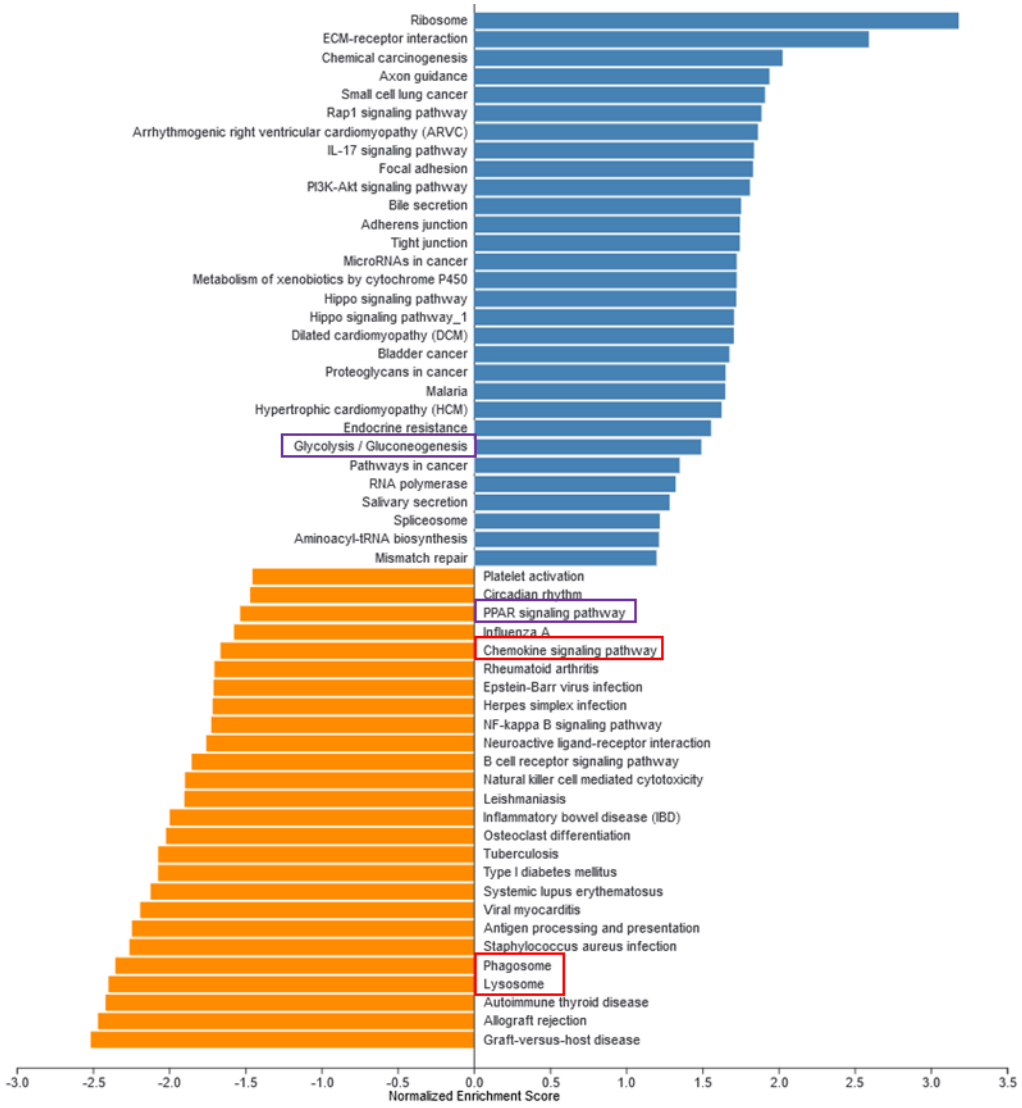

Figure 3 | Gene set enrichment analysis of uninfected 7c-deficient versus 7c-floxed AMs. Uninfected $7c^{-/-}$ AMs have various pathways upregulated (top, blue) or down-regulated (bottom, orange) when compared with uninfected $7c^{FL/FL}$ AMs as calculated by a normalized enrichment score for each pathway. Shown are the most significant gene enrichment changes between the two (3 $7c^{-/-}$ and 3 $7c^{FL/FL}$) sets of mice. The boxed pathways designate enrichments relevant to bacterial killing (red) and metabolism (purple).

Figure S13A). Top pathways within each cluster were identified, and an overrepresentation analysis of all the differentially expressed genes taken together **(Supplemental Figure S13B**) provided some evidence for the importance of the peroxisome proliferator-activated receptor (PPAR) signaling pathway. Potential upstream regulators were identified **(Supplemental Figure**

S13C, D) and a pathway map connecting differentially expressed genes was created describing the relevance and contribution of genes like TGF-β and VEGF **(Supplemental Figure S13E).**

The transcriptional differences between the mice were made clearer using a gene set enrichment analysis (GSEA) **(Figure 3).** The GSEA demonstrated that there were changes in the *7c*$^{-/-}$ AMs not only related to the PPAR signaling pathway but also to the phagosome, lysosome, chemokine signaling pathway, and glycolysis. We separated these changes into two categories – alterations directly related to an impaired bacterial killing phenotype (i.e. phagolysosomal modifications) and those related to AM metabolism (the PPAR gamma pathway and glycolysis).

When examining expression of transcripts pertaining to the phagosome (identified using the mouse KEGG phagosome pathway) (Kanehisa et al. 2021), we observed global downregulation of most phagosomal-related genes that were sequenced (**Figure 4A**). Of note was the downregulation of the NADPH oxidase complex, which would reduce the ability of AMs to generate free radicals capable of killing *M. smegmatis*. Because these genes were identified using GSEA rather than looking specifically at the most differentially regulated genes, it was important to consider the actual fold-change of each gene of consideration (**Figure 4B).** Quantification of the exact nature of the phagosomal pathway change demonstrated that nearly half of the implicated genes were downregulated by at least 2-fold. The lysosomal **(Supplemental Figure S15)** and endocytosis **(Supplemental Figure S16)** sets of transcripts, which have some degree of overlap, had similarly strong perturbations. Perhaps as a result of reduced phagolysosomal activation, antigen processing and presentation genes associated with the MHCII presentation pathway were downregulated **(Supplemental Figure S17**).

We further explored the metabolic perturbations that had been identified **(Figure 5)**. Lipid pathways downstream of PPARs showed mostly downregulation (**Figure 5A**), but there was a

A

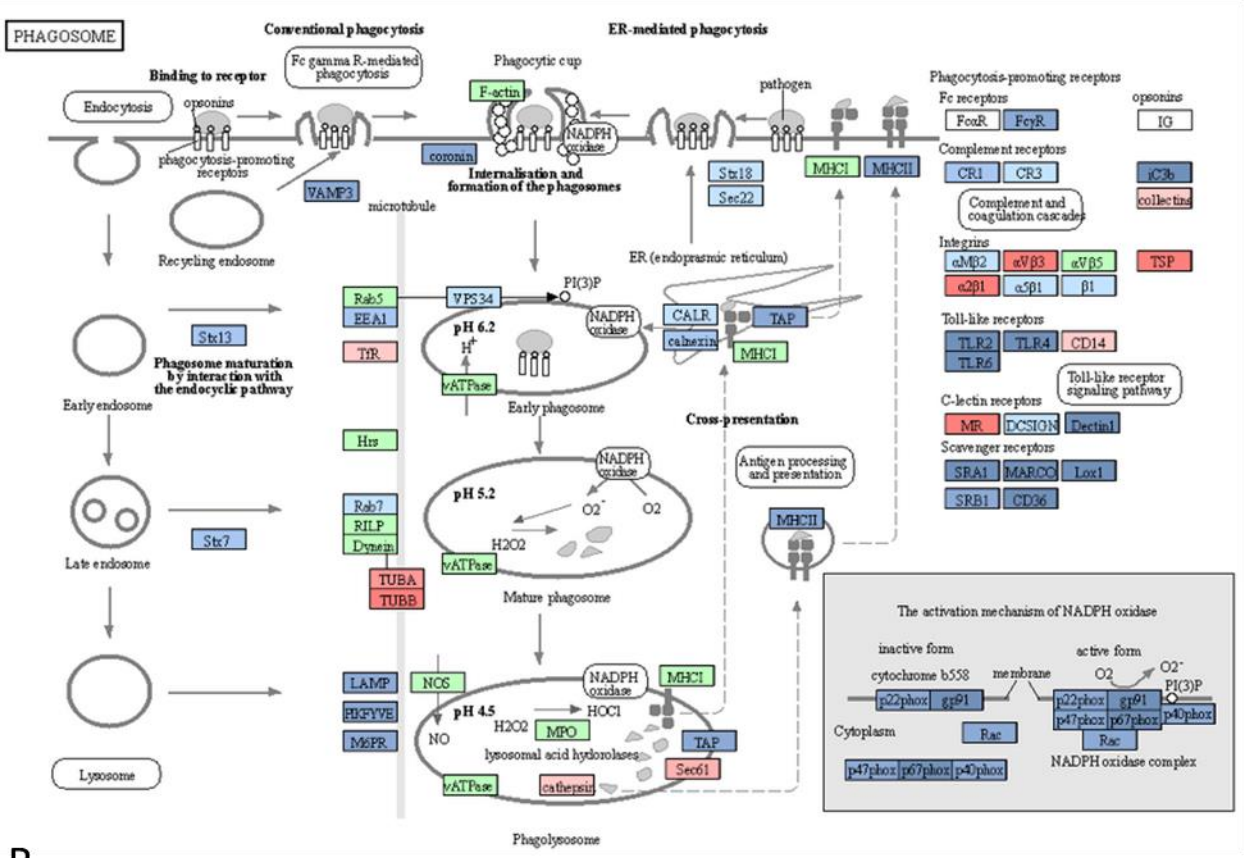

B

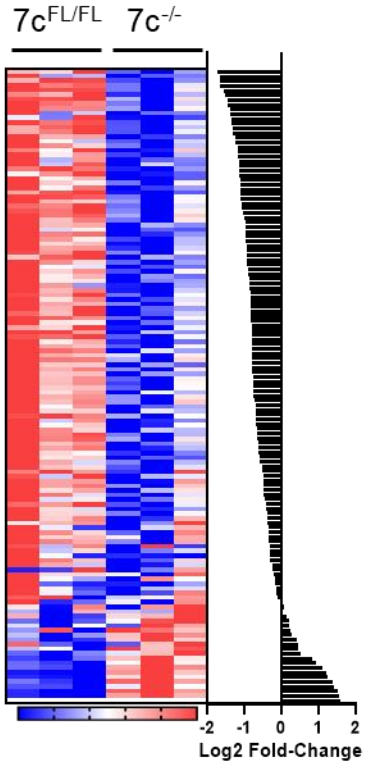

Figure 4 | 7c$^{-/-}$ AMs exhibit reduced expression of transcripts related to the phagosome. A) Pathway map illustrating multiple pathways of phagocytosis and the genes/transcripts relevant to them. Blue boxes indicate that the transcript is downregulated at least 25% in 7c$^{-/-}$ AMs vs 7c$^{FL/FL}$ AMs (dark blue indicates >2-fold decrease), while red indicates that the transcript is upregulated at least 25% in 7c$^{-/-}$ AMs vs 7c$^{FL/FL}$ AMs (bright red indicates >2-fold increase). White and green boxes represent transcripts that were altered <25% between 7c$^{-/-}$ and 7c$^{FL/FL}$ AMs or not detected in sufficient abundance from RNAseq (green boxes show genes that differ significantly among species; shown here is a mouse pathway map). **B)** Heat-map (left) and graph depicting fold-change (right) for all genes represented in the phagocytosis pathway from **A.** Red indicates upregulation vs. the average expression level and blue indicates decreased expression vs. the average.

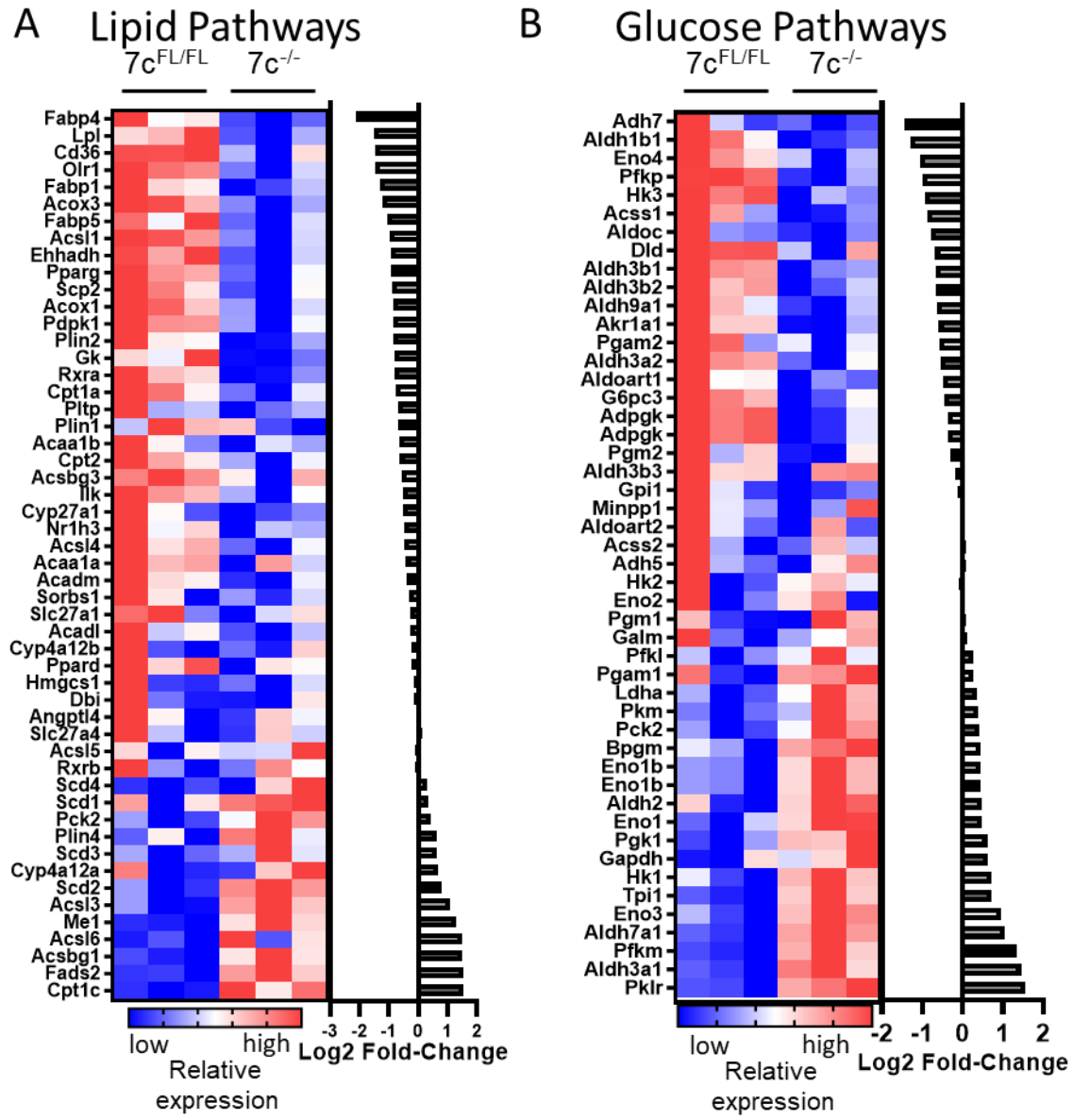

Figure 5 | Transcriptional changes for genes relating to lipid and glucose-utilizing pathways. Comparison of transcriptional expression for uninfected $7c^{-/-}$ and $7c^{FL/FL}$ AMs examining **A)** a lipid-centric set of genes, obtained from KEGG mmu03320 for describing PPAR downstream effects, and **B)** a glucose-centric set of genes, obtained from KEGG mmu00010 for analyzing glycolysis, gluconeogenesis, and the citric acid cycle. Red boxes indicate expression levels above the average and blue boxes indicate expression levels below the average. The bar chart to the right of each heat map depicts the log2-fold change for each gene with positive values representing increased expression in the knockout AMs.

cluster of genes that were upregulated. By examining the pathways associated with these genes (**Supplemental Figure S18**), we recognized that genes associated with fatty acid transport and lipogenesis remain activated but those related specifically to fatty acid oxidation were downregulated. This is supported by downregulation of various genes in the peroxisome related not only to fatty acid oxidation but to receptor recycling and ROS metabolism (**Supplemental Figure S19**).

While genes pertaining to fatty acid degradation were downregulated in *7c*$^{-/-}$ AMs, many of those in the glycolytic pathway **(Figure 5B**) were upregulated. Examination of the exact pathways of genes involved **(Supplemental Figure S20)** demonstrates that those genes forming the core of glycolysis from glucose entry into the cell (Glut1) to pyruvate seem to be upregulated.

The RNAseq data characterized the *7c*$^{-/-}$ AMs as those less capable of phagocytosing and fighting pathogens, while simultaneously expressing an altered metabolic gene profile. In order to better characterize which of these might be more likely to be driving the observed phenotype in AMs, we examined lysosomal acid lipase as a suitable marker that might be perturbed by either lysosomal changes or fatty acid pathway changes. Despite changes observed at the transcriptional level downregulating various genes pertaining to the lysosome, *7c*$^{-/-}$ AMs still maintained similar levels of lysosomes to *7c*$^{FL/FL}$ AMs as measured by the fluorescent probe lysotracker green **(Figure 5A)**. A fluorescent probe indicating the activity of lysosomal acid lipase itself, however, demonstrated significant downregulation of lipase activity in the *7c*$^{-/-}$ AMs **(Figure 5B).** An overriding relevance of the underlying metabolic genes was further supported by our lab's previous work examining 7c, wherein the most consistent phenotype observed in cell lines was altered metabolism. One example of this was the altered metabolite profile seen in *7c*$^{-/-}$ THP-1 cells **(Supplemental Figure S21)**, which upon reexamination in the context of altered lipid metabolism

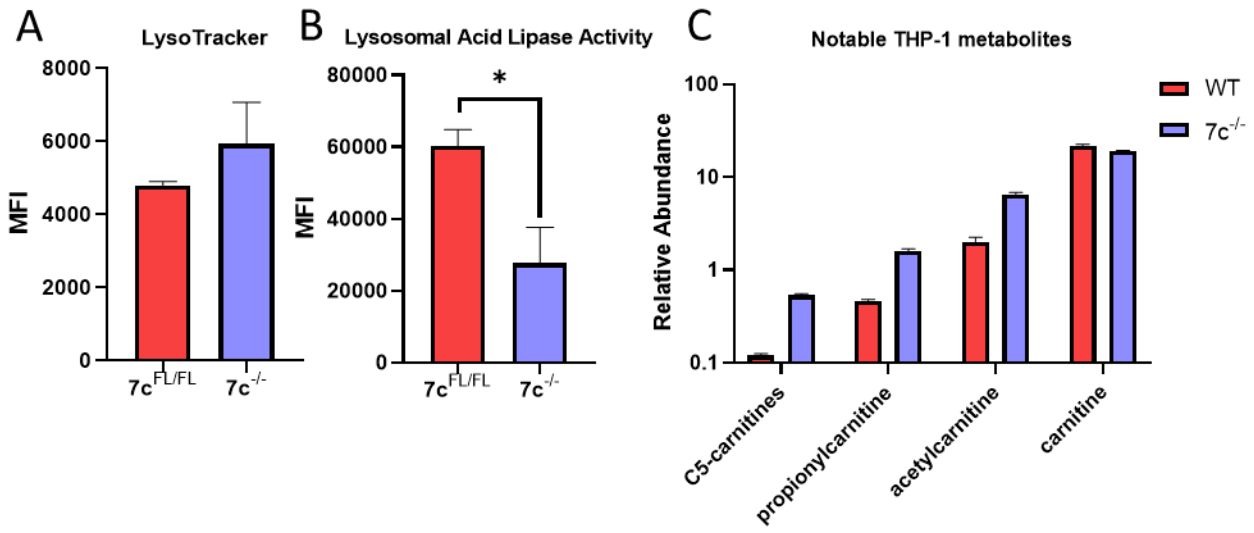

Figure 5 | 7c-deficient cells reveal markers supporting dysregulation of fatty acid oxidation. **A)** LysoTracker did not show significant alterations in lysosomal counts between $7c^{-/-}$ and $7c^{FL/FL}$ AMs, so a **B)** flow cytometry-based lysosomal acid lipase assay was performed revealing significantly ($p = 0.0402$) decreased lipase activity in $7c^{-/-}$ AMs. **C)** HILIC metabolite analysis from the monocytic THP-1 cell line demonstrates upregulation of most carnitine ions detected (except carnitine itself).

reveals significant ($p<0.01$) upregulation of various carnitines including C5-carnitines, propionylcarnitine, and acetylcarnitine, supporting potential dyslipidemia **(Figure 5C).**

Glucose supplementation rescues bacterial killing by Mfsd7c-deficient alveolar macrophages

Taking into consideration that *7c*$^{-/-}$ AMs exhibited downregulated fatty acid oxidation genes on RNAseq, we examined whether immune functions such as phagocytosis might be differentially affected between *7c*$^{-/-}$ and *7c*$^{FL/FL}$ AMs depending on the media provided to the AMs during the experiment. We compared phagocytosis of GFP-expressing *M. smegmatis*, as measured by an increase in the GFP fluorescence observed on flow cytometry. *M. smegmatis* was only coincubated with AMs for one hour (and at MOI 25 to increase uptake within such a short amount

of time), reducing the likelihood that AMs would have sufficient time to break through the mycobacterial wall after killing the bacteria and degrade the intrabacterial GFP. We can thus consider this experiment to be measuring phagocytosis rather than bacterial killing.

We observed that across medias examined (RPMI, a linoleic acid/BSA fatty acid media, and PBS), a similar number of both *7c*$^{FL/FL}$ and *7c*$^{-/-}$ AMs seemed to phagocytose sufficient bacteria above their high level of autofluorescence in the GFP channel **(Figure 6A).** However, when we examined the mean fluorescent intensity for each of those bacteria-positive AMs, we found that *7c*$^{FL/FL}$ AMs phagocytosed significantly larger quantities of *M. smegmatis* particularly in the fatty acid media **(Figure 6B).** This supports the notion that the phagocytosis impairment of *7c*$^{-/-}$ AMs is at least partially dependent on the surrounding environment and metabolic substrates that are available to utilize.

Considering that the alveolar environment is high in lipids and low in glucose, we designed an experiment to examine whether the inhibited *7c*$^{-/-}$ AM bacterial killing phenotype could be rescued with administration of glucose. Due to the increased granulocyte infiltration into the *7c*$^{-/-}$ lungs relative to the *7c*$^{FL/FL}$ lungs during infection, we were concerned that the presence of glucose would support the activity of that larger population of neutrophils and provide us an inaccurate snapshot regarding glucose's ability to rescue the AMs themselves. We utilized a dye that we had previous experience with (pHrodo) that would allow us to mark macrophages as having once phagocytosed bacteria even if they eliminate any intrabacterial GFP. Essentially, whereas the GFP might be degraded by the AMs during the experiment, the pHrodo dye will remain and mark those AMs as having successfully acidified and degraded their once intracellular *M. smegmatis*. We would stain *M. smegmatis* bacteria being used for the infection with the pHrodo dye just prior to intratracheal injection, and then any bacteria that are phagocytosed would leave an increased

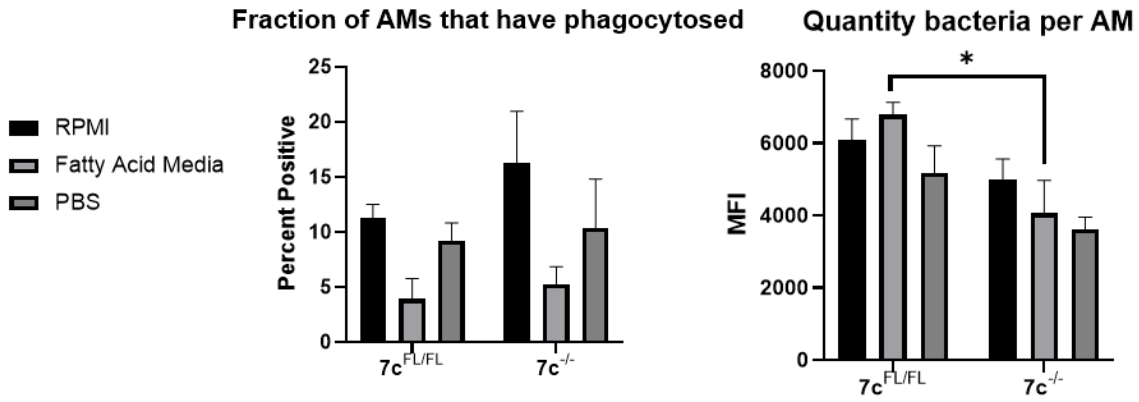

Figure 6 | Glucose-free media diminishes 7c$^{-/-}$ AM phagocytic capacity in vitro.· RPMI, a fatty acid media, and PBS were compared for incubation of a 1 hour phagocytosis assay of GFP-expressing *M. smegmatis* (MOI 20) using AMs from three 7c$^{-/-}$ and three 7c$^{FL/FL}$ mice. **A)** The fraction of AMs that have uptaken any *M. smegmatis,* as assessed by an MFI above the uninfected AM threshold, is similar between 7c$^{FL/FL}$ and 7c$^{-/-}$ in each of the medias. **B)** The quantity of bacteria phagocytosed by the AM populations from **A** was measured using the MFI from each *M. smegmatis*-positive population. The 7c$^{-/-}$ AMs demonstrate a lower MFI than the 7c$^{FL/FL}$ AMs in the fatty-acid media (p=0.0484).

pHrodo intensity on the AM when it is later analyzed on flow cytometry. By comparing the change in pHrodo signal versus the change in GFP signal for each cell, we can observe whether that cell is more likely to have killed bacteria or have allowed them to survive and/or proliferate. This ability to discriminate between cells that have definitely phagocytosed *M. smegmatis* by using the pHrodo dye **(Figure 7A)** is particularly important because the high level of autofluorescence in the GFP channel makes it difficult to examine AMs infected with the relatively low quantities they experience *in vivo* **(Figure 7B)**.

Using these pHrodo-stained *M. smegmatis* bacteria, we then injected mice with either stained bacteria in PBS or stained bacteria in 100mg/dL glucose (using a 50µL intratracheal injection). 100mg/dL represents a typical blood glucose level, although it will presumably be

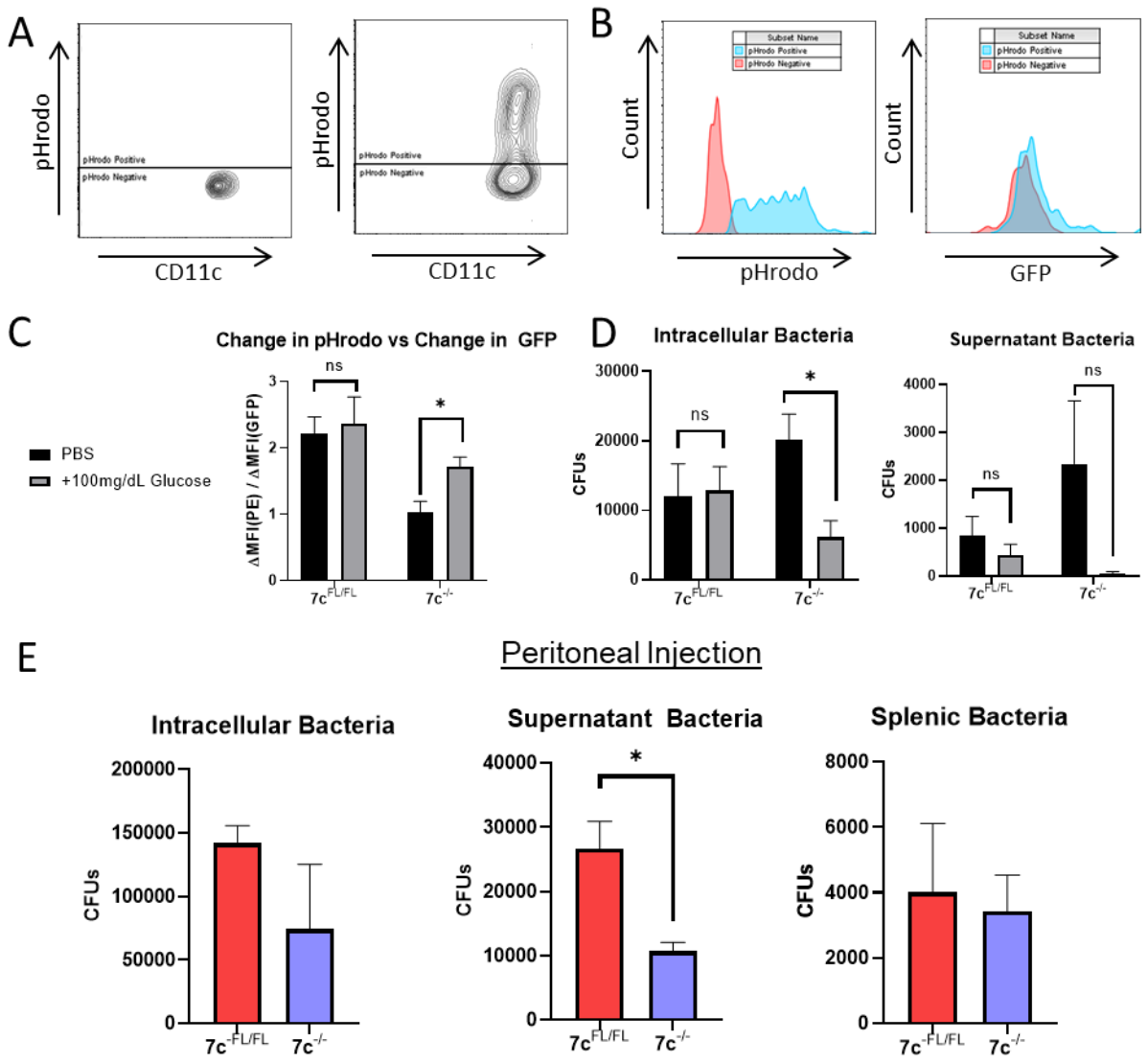

diluted within the lungs and taken up by cells quite rapidly. For this reason, we limited this experiment to 8 hours rather than examining the 24-hour timepoint that gives more significant differences between the *7c*$^{-/-}$ and *7c*$^{FL/FL}$ AMs.

The ratio of change in pHrodo versus change in GFP was significantly upregulated in the *7c*$^{-/-}$ AMs who received 100mg/dL glucose alongside the *M. smegmatis* during the intratracheal injection instead of simply PBS **(Figure 7C).** In further support of the ability of glucose to rescue the inhibited bacterial-killing phenotype of *7c*$^{-/-}$ AMs, the CFUs from the intracellular

Figure 7 | Glucose eliminates the impaired bacterial killing of $7c^{-/-}$ macrophages. AM phagocytosis of *M. smegmatis* coated with pHrodo dye (**A**, right) increases the PE signal well above the autofluorescent background of uninfected AMs (**A**, left). Coating this dye to *M. smegmatis* used for intratracheal injections allows for identification of any macrophages that have participated in phagocytosis (**B**, blue) because they will have a higher PE MFI than those that have not (**B**, red) even if the GFP is degraded by the AM. **C**) Comparing the ratio of the changes in the pHrodo MFI vs GFP MFI of infected AMs 8 hours after intratracheal injection reveals $7c^{-/-}$ AMs are not killing the bacteria they phagocytose as effectively when bacteria are injected in PBS relative to when they are injected with 100mg/dL glucose ($p = 0.0365$; 3 mice per condition). This rescue of $7c^{-/-}$ bacterial killing can also be observed by the changes in intracellular (**D**, left, $p = 0.0329$) CFUs with glucose administered alongside the bacteria; the changes in the supernatant bacteria (**D**, right) were not significant. **E**) An intraperitoneal injection was performed using 3 $7c^{-/-}$ and 3 $7c^{FL/FL}$ mice and CFUs assessed after 24 hours peritoneal infection. The $7c^{-/-}$ peritoneal macrophages reduced the supernatant CFUs more effectively than the $7c^{FL/FL}$ macrophages ($p = 0.0253$).

fraction of the lavage were significantly decreased in mice that received glucose alongside the *M. smegmatis* rather than just PBS **(Figure 7D).**

In consideration of how else to indicate that 7c's function is important to macrophages primarily in the lipid-rich alveolar surfactant, we performed intraperitoneal infections in order to compare whether there would be any phenotypic effects for $7c^{-/-}$ macrophages within the peritoneal space, which is characterized by glucose concentrations similar to those seen in the blood. The intraperitoneal infections were examined after 24 hours and showed that $7c^{-/-}$ peritoneal macrophages did not demonstrate any impaired bacterial killing in the intracellular fraction of the peritoneal lavage or in bacteria migrated to the spleen, but actually exhibited significantly increased bacterial killing on the extracellular bacteria obtained via the supernatant fraction of the lavage (**Figure 7E).**

The successful rescue of the impaired bacterial killing of $7c^{-/-}$ AMs by glucose supports the notion that metabolic alterations are the main drivers of the observed pathology, but some questions remain open. One interesting finding from these experiments was the upregulated levels of IFN-gamma seen in the $7c^{FL/FL}$ lungs that the knockout mice were unable to elevate. IFN-gamma

is extremely relevant to our examination of intracellular bacterial killing, but we did not identify the reason for why it would be decreased in the *7c*$^{-/-}$ mice. It is unlikely that IFN-gamma, commonly released by T cells and NK cells, is released by the AMs themselves, so that suggests that either the neutrophils being recruited are indeed affected by *7c* knockout and are no longer using cytokines appropriately, or there is some signaling that would normally occur to elicit IFN-gamma from other cells but the *7c*$^{-/-}$ cells are no longer able to achieve.

Methods

Mice. C57BL/6 N embryonic stem (ES) cells cloned with floxed exon 2 of Mfsd7c were purchased from EuMMCR (European Mouse Mutant Cell Repository, ES cell Clone ID: HEPD0572_8_F01). After removal of the neomycin resistance cassette, the Koch Institute Swanson Biotechnology Center injected blastocysts with the ES cells and transferred these into pseudopregnant mice. 7c$^{WT/FL}$ heterozygous mice were interbred to generate homozygous 7c$^{FL/FL}$ mice, which were then bred with LysM-Cre mice (Jackson Laboratory, Stock No: 004781) to generate the myeloid-specific 7c knockout mice used in our experiments. Mice were maintained in the animal facility at MIT and all animal studies and procedures were carried out following federal, state, and local guidelines under an MIT IACUC-approved animal protocol.

Genomic DNA extraction and genotyping. A small piece of mouse ear or tail was cut using scissors, placed in 200 μL of 25mM NaOH with 0.2mM EDTA and digested for 1 hour at 95°C. Digested tissue was centrifuged at 13,000×g for 5 min, and the cleared supernatant was used directly for genotyping. For genomic DNA from cells rather than tissue (e.g. BMDMs, AMs,

neutrophils), a GenElute Mammalian Genomic DNA Miniprep Kit (Sigma-Aldrich) was used and followed according to manufacturer's instructions. 7C flox was validated using either GT1 (GAACTGTGTATCAGTCAAGTTGTCAAGG) and FL1R (GAGCTCATTGGCCAGCCAGC), wild-type=197bp and ko=414bp, or GT1 and FL2R (GACAGGGTAGTAGTCTGGCTGC), wild-type=907bp, floxed=1341bp, and ko=459bp. LysM-Cre was validating using LYWT (TTACAGTCGGCCAGGCTGAC), LYCR (CCCAGAAATGCCAGATTACG), and LYCO (CTTGGGCTGCCAGAATTTCTC) in a 3-primer PCR; Cre-negative=350bp and Cre^{+}=700bp.

Immunophenotyping. For assessment of immune compartments in $7c^{-/-}$ mice, the blood, lymph nodes, bone marrow, and spleen were examined. Flow cytometry was performed in 10% FBS in PBS on ice, and anti-CD16/32 was used for 15 minutes prior to the regular staining to block Fc receptors. Fluorescently labeled antibodies were then added at 1:400 dilutions to 200µL cell solutions for 30 minutes staining at 4°C, after which 1mL staining solution was added to all samples to wash away unbound and nonspecific antibodies. One additional wash was performed (400g/5min/4°C), and then cells were analyzed by flow cytometry.

Blood was obtained via cardiac puncture – mice were euthanized via CO2 asphyxiation followed by rapid exposure of the heart and puncture of the right atrium by a 20G needle while providing negative pressure via 5mL syringe. This generally yielded around 150µL blood, which would then be exposed to 1mL ACK lysis buffer prior to significant clot formation. After 5 minutes lysis, 10mL complete RPMI were added to the white blood solution and pushed through a 70µm filter into a 15mL conical tube. This tube was centrifuged at 400g/5 min/4°C and the cells were resuspended for staining for flow cytometry.

Inguinal lymph nodes were used to examine lymphocyte populations. Briefly after CO2 euthanasia the mouse skin was incised in the center and then carefully pulled back to reveal the inguinal lymph nodes at the branching of subcutaneous vessels. Each lymph node was isolated and then resuspended in 1mL complete RPMI by puncturing the capsule with a 200µL pipet tip and repeatedly pipetting fluid up and down over the exposed node. The lymph node solution was then filtered over a 70µm cell strainer to remove lingering stromal cells and connections. This solution was then spun down (400g/5min/4°C) and was used for flow cytometry staining.

For collecting bone marrow, femurs were removed and washed in 70% ethanol for 1 minute, after which time the bone marrow was flushed out using 5 mL of cold RPMI media. Bone marrow cells were collected by centrifugation (1200g for 5 min at 4 °C) and resuspended in 3 mL of ACK lysis buffer. After incubation at room temperature for 3 min, ACK buffer was neutralized by the addition of 10 mL of cold DMEM media, passed through a 70µm cell strainer, and cells were centrifuged at 1200g for 5 min at 4 °C. Cells were then ready for flow cytometry.

For examining the spleen, the organ was harvested from the mouse and pulverized against a 70µm cell strainer using a 5mL syringe plunger. Once the organ had become a paste, 10mL of RPMI were passed over the cell strainer to push only cells through and create a cell suspension suitable for flow cytometry. The suspension was then centrifuged for 1200g/5min/4°C and the pellet was resuspended in 3mL ACK lysis buffer. After 3 minutes lysis, 10mL RPMI were added and the new suspension was again strained through a 70µm filter. This new cell pellet was resuspended in flow cytometry buffer and used for staining.

Knockout validation using microscopy. $7c^{FL/FL}$ and $7c^{-/-}$ AMs were isolated via bronchoalveolar lavage, spun down and resuspended in complete RPMI, and plated (10^5 cells per well) onto a 8-

well chambered cover glass (Thermo Scientific #155360). After 30 minutes, cells were washed with PBS and fixed using 4% paraformaldehyde solution for 15 minutes at room temperature. After 15 minutes, cells were gently washed three times using PBS and permeabilized in 0.3% Triton X-100 in PBS for 30 minutes at room temperature. Cells were gently washed (5 minutes/wash) in PBS and anti-CD16/32 was added to the cells in 1% BSA and allowed to react for 30 minutes. The cells were washed three times in PBS and then biotinylated anti-Mfsd7c (Biorybt #orb455755) was added 1:50 in 1% BSA and 0.3% Triton X-100 in PBS and stained for 2 hours at room temperature. The cells were then washed three times in 1% BSA in TBS (50mM Tris, 150mM NaCl, pH 7.4), Streptavidin-APC was added to 1% BSA in TBS (1:200) and staining proceeded for 1 hour at room temperature. Cells were then washed three times in 1% BSA in TBS, and DAPI counterstain was added at 500ng/mL and allowed to stain for 3 minutes. The DAPI was then washed away using 1% BSA in PBS and cells were imaged using a Deltavision Ultra DIC microscope.

M. smegmatis. Mycobacterium smegmatis MC2155 expressing GFP under selection by Hygromycin B (HyB), obtained from Bryan Bryson here at MIT, is grown in growth medium (LB, 0.05% Tween-80, 50µg/mL HyB) for 24+ hours at 37°C/225rpm until mid-log phase (OD600 of 0.5-1.0 is reached). Culture is allowed to sit for 20 minutes at room temperature to allow clumps to settle, then supernatant is spun at 4°C/3000rpm/10min to pellet bacteria. Bacteria is washed twice in PBS and then resuspended in sterile PBS. Suspension is adjusted for intratracheal injections to an OD600 of 2.0 (0.2) obtained via nanodrop, which corresponds to a concentration of 10^8 bacteria/mL.

Intratracheal injections. Intratracheal injection protocol was adapted from one designed by Vandivort et al., 2016. Mice are anesthetized using isoflurane. After confirming sedation, mouse is suspended by upper incisors on positioning platform; tape is used to help maintain positioning. Sterilized blunt end forceps are used to gently grip and pull the tongue out of the oral cavity; the tongue is then depressed. Using an illuminator to visualize the trachea, a 22G catheter attached to a syringe containing 60uL PBS without a plunger (a makeshift spirometer) is guided down the natural path of the trachea. The rise and fall of the PBS is used to confirm proper placement. The catheter is inserted 5mm, then tongue depression is ended to help keep catheter in place. The PBS-containing syringe is removed from the catheter, and then 50uL injection solution containing bacteria is administered to the catheter lumen via pipette. A syringe with the plunger set to 300uL air is then attached to the catheter. Then 300uL air is administered to move the injection solution down the catheter into the trachea. Finally, the PBS-containing syringe without a plunger (the makeshift spirometer) is replaced onto the catheter to confirm proper placement is still present at the end of the procedure. The catheter and tape are removed and the mouse is moved to a warm dry place to recover.

Bronchoalveolar lavage. Mice are euthanized using CO2 asphyxiation and the skin is cut open using scissors. The peritoneal cavity is opened with an incision just below the sternum, and the peritoneum is cut laterally just below the diaphragm across the front of the mouse. The liver is moved out of the way so that the mediastinum can be visualized through the diaphragm, and the diaphragm is punctured toward the mediastinum to avoid cutting the lung tissue. The diaphragm is then peeled back as the lungs deflate, and the ribs and front of the thorax are removed. The salivary glands are pushed aside and the muscles overlying the trachea are cut. 4.0 nylon suture is

passed beneath the trachea and a surgeon's knot is prepared around the trachea, but not tightened. A small incision is then made on the front of the trachea and a catheter is pushed in exactly 5mm (marked on the catheter to keep it at the correct location). The suture is then tightened around trachea and catheter. Pre-warmed 37°C lavage buffer consisting of 2mM EDTA and 0.5% FBS in PBS is then used to lavage the lungs five times by injecting 1mL at a time in a syringe, slowly inflating the lungs (which is visually observed) and deflating them with each mL. The first mL is generally kept separate from the other four mL obtained and has importance in specific protocols. After 5 1mL washes have been performed, approximately 4mL of lavage is generally recovered and can be used for further experiments.

In vivo bacterial killing assays. M. smegmatis, cultured as previously described, is adjusted to an OD of 2.0 and used for intracheal injection (each mouse receiving 50µL injection). The mice are then rested and at the desired time point euthanized using CO2 asphyxiation. Bronchoalveolar lavage is performed and the first sample set aside for use in supernatant bacteria assays and sometimes cytokine profiling. The four-lavage and single-lavage tubes are both spun down at 400g/5min/4°C, and the supernatant from the first lavage is set aside. This lavage is serially diluted onto 50µg/mL Hygromycin B LB agar plates and assessed for bacterial counts of bacteria that were not contained within cells. The cell pellets from the single-lavage and four-lavage tubes are combined, and half are used for flow cytometry and half are used for assessing intracellular bacteria. For intracellular bacteria, some *M. smegmatis* has spun down but is not located within cells, so a gentamicin protection assay is performed. 50µg/mL gentamicin in complete RPMI are added to these cells and they are incubated at 37°C for 1 hour. After this time, they are spun down and resuspended up and down in 100µL 0.1% Triton X-100. After 5 minutes in Triton X-100,

900µL PBS are added to prevent further lysis that may affect the bacteria, and the lysed cell solution is serially diluted and plated on Hygromycin B LB agar plates. Flow cytometry is performed to determine the profile and quantity of macrophages vs neutrophils, and in some experiments beads were used to quantify the number of cells; in other experiments, they were simply counted via hemocytometer. Cells were stained and the macrophages were identified based on high autofluorescence and CD11c positivity, whereas the Gr1 was an effective stain for identifying the neutrophil population. Cells were blocked using 1:200 anti-CD16/32 in 1% BSA in PBS for 30 minutes on ice, then they were stained using the previously described antibodies (all 1:200) for 30 minutes on ice. After staining, cells were washed once in PBS and flow cytometry was performed.

Cytokine analysis. Supernatants from the first sample of bronchoalveolar lavage were sent to Eve Technologies (Calgary, CA) for an 18-plex mouse high sensitivity assay measuring GM-CSF, IFNγ, IL-1α, IL-1β, IL-2, IL-4, IL-5, IL-6, IL-7, IL-10, IL-12p70, IL-13, IL-17A, KC/CXCL1, LIX, MCP-1, MIP-2, and TNFα.

Histology. After CO2 euthanasia, mice were prepared as usual for bronchoalveolar lavage. However, instead of performing the lavage as usual, 1mL of 10% neutral-buffered formalin was instead slowly instilled into the lungs over a period of two minutes. After allowing for 5 minutes of formalin-filled lung, the lung was carefully excised from the surrounding anatomy and placed in a histology cassette for 2 additional days fixation. After 48 hours, the cassette was transferred to 70% ethanol and submitted to the histology core for H&E staining as well as unstained samples to be used for later analyses.

Neutrophil bacterial killing assay. Neutrophils were isolated from bone marrow using a commercial isolation kit (Biolegend #480057), and purity was confirmed using flow cytometry. Cells were then primed and bacterial killing was assayed mostly following the protocol of Ellson et al. (Ellson et. al, 2006). Neutrophils were resuspended in DPBS+ (PBS with Ca2+ and Mg2+, 1 g/liter glucose, and 4 mM sodium bicarbonate) and primed at 37°C with 500 U/ml mTNF-α, 100 ng/ml mGM-CSF, and 10% mouse serum for 1 hour. Mouse serum was obtained by collecting mouse blood via intracardiac puncture and allowing blood to clot over 45 minutes at room temperature, followed by centrifugation at 1500g/10min/room temperature. $5x10^5$ neutrophils for 3 $7c^{FL/FL}$ and 3 $7c^{-/-}$ mice were used for bacterial killing assessment. Each set of neutrophils in DPBS+ (in 50µL) was added to $5x10^5$ freshly-grown *M. smegmatis* in DPBS+ (in 50µL) and they were co-incubated at 37°C in 100µL total solution with rapid orbital mixing. After 1 hour, cells were lysed via administration of 0.1% Triton X-100 in PBS and serial dilutions performed to plate surviving bacteria on Hygromycin B agar plates.

.*RNAseq sample preparation and sequencing.* Bronchoalveolar lavage samples were obtained and after removing 10% of the samples, they were spun down at 400g/5 min/4°C and resuspended in RLT lysis buffer. The lysed AMs were then flash frozen in liquid nitrogen and stored for later RNA isolation. The 10% of samples that had been removed was split into two categories, one to validate that each sample had high purity of AMs and one to verify the genotype of the AMs using PCR. RNA isolation was performed using a commercial kit (Qiagen RNEasy miniprep #NC9307831) directly before submitting to the MIT BioMicroCenter core for RNAseq via Illumina HiSeq using 40BP SE primers. A NEB ribodepletion kit was used by the core to improve

mRNA purity, and sample quantity and purity were validated using the Bioanalyzer system before proceeding to sequencing.

RNAseq Data Analysis. Sequencing data was counted and normalized, thresholding counts per million above 10 due to the relatively low number of counts obtained from our samples. dgeObj package for R (https://cran.r-project.org/web/packages/DGEobj/index.html) was used to examine dispersion and create a non-hierarchical clustering of the most differentially expressed genes. Gene ontology was used to identify the most represented processes within each cluster. Using fold-change values, p-values, and FDR values obtained by the analysis, we performed a canonical pathway analysis on the most differentially expressed genes (combining down-regulated and up-regulated data) using Ingenuity's proprietary software. Gene set enrichment analysis was performed using the WebGestalt toolkit (Liao et al.,2019). KEGG (Kyoto Encyclopedia of Genes and Genomes) maps were used to visualize and impute RNAseq data onto specific pathways of interest (Kanehisa et al., 2021).

Heme preparation. For each experiment, a small quantity (~3mg) of hemin chloride (Sigma Aldrich #3741) was freshly diluted in 100uL 100mM NaOH with 25mM Tris-HCl. A 1:100 dilution in PBS was used to examine the absorbance at 385nm, and the prepared solution's heme concentration was determined using an extinction coefficient of 58,440 $M^{-1}cm^{-1}$ (Hofbauer et al., 2015).

Lysotracker and lysosomal acid lipase activity. Commercial kits were used for both lysotracker (Fisher Scientific #L7526) and lysosomal acid lipase activity (Abcam #ab253380) measurements.

For lysotracker, AMs were not plated but incubated directly with the lysotracker reagent for 15 minutes at 37°C in complete RPMI before being placed on ice and brought to flow cytometry. For lipase activity measurement, AMs were plated $2x10^4$ / well on non tissue-culture treated 48-well plates in RPMI and allowed to adhere for 30 minutes. After that, media was washed away and manufacturer instructions were followed for adherent cells (the lipase reagent was coincubated with AMs for 2 hours), with the main change being that before measuring cellular fluorescence AMs had to be lifted from wells in a specific manner – cells were washed using PBS and then incubated in accutase for 1 hour to lift them. Both measurements were determined using the FITC channel.

THP-1 phagocytosis assays. The B11 THP-1 $7c^{-/-}$ clone previously developed by our lab was compared with a WT THP-1 clone. Both cell types were grown in complete RPMI supplemented with 2μM β-mercaptoethanol. For phagocytosis assays, 10^5 cells in 100μL media were added to each well of a 96-well U-shaped-bottom plate. Dead *E. coli* bioparticles stained with Alexa 488 (Invitrogen #E13231) were either used directly or after opsonization (Invitrogen # E2870) according to the manufacturer's directions. Bioparticle numbers were determined by manually counting via microscope so that an appropriate number could be added to each well to provide the appropriate multiplicity of infection. Bioparticle concentrations were corrected to 11x the desired end result, and then 10μL bioparticle solution was added to each well containing 100μL THP-1 cells 1 hour after the THP-1 cells had been plated. At each time point (1, 2, 4, and 8 hours), the THP-1 cells were spun down at 400g for 5 minutes, then washed once in PBS + 1% BSA. Cells were then analyzed via flow cytometer to determine the extent of bioparticle uptake.

Bone marrow-derived macrophage (BMDM) phagocytosis assay. Mice were euthanized using CO2 asphyxiation. Femurs were removed and washed in 70% ethanol for 1 minute, after which time the bone marrow was flushed out using 5 mL of cold DMEM media. Bone marrow cells were collected by centrifugation (1200g for 5 min at 4 °C) and resuspended in 3 mL of ACK lysis buffer. After incubation at room temperature for 3 min, ACK buffer was neutralized by the addition of 10 mL of cold DMEM media and cells were centrifuged at 1200g for 5 min at 4 °C. Cells were resuspended in BMDM media (DMEM media containing 10% FBS, 20% L929-conditioned media, 2 mM L-glutamine, 2 mM pyruvate, non-essential amino acids at 100 μM each, 0.55 mM 2-mercaptoethanol, and penicillin/streptomycin), and passed through a 40μm Falcon cell strainer (VWR) to remove large aggregates.

Bone marrow cells were then counted and seeded in 10 cm non tissue-culture treated plates at 10^6 cells per plate in 10 mL of BMDM media. Two days later, an additional 10 mL of BMDM media was added. On days 4 and 6, old media was removed and 10 mL of fresh media was added. On day 7, fully differentiated BMDMs were lifted in PBS supplemented with 10 mM EDTA for 5 min at 37 °C, then centrifuged and resuspended in BMDM media to a density of $5x10^5$ / mL. $2x10^5$ BMDMs were added to each well of a 48-well non tissue-culture treated dish and allowed to adhere for 24 hours. *E. coli* bioparticles (either opsonized or not) were then added at MOIs 5 and 10 to assess BMDM phagocytosis. After 8 hours, BMDM media was removed, BMDMs were washed once in PBS, and PBS with 5mM EDTA was added to lift cells from the plate. After 5 minute incubation at 37°C, cells were lifted and GFP intensity assessed using the FITC channel via flow cytometry.

In vitro AM phagocytosis assay using varying medias. AMs were isolated as previously described with one exception – when culturing cells into varying medias, the cells are resuspended into PBS containing 1% BSA rather than RPMI. This means that following the 5min/400g/4°C spin after collecting all the lavages, cells are resuspended in PBS/1% BSA and counted. $2x10^4$ AMs are added to each well of 48-well non culture-treated plate and allowed to adhere and remain in that solution after plating and 30 minute incubation at 37°C. After removing the PBS, either complete RPMI without antibiotics, 10mg/mL BSA conjugated to linoleic acid in PBS (10x dilution of Sigma #L9530), or 1% BSA in PBS was used as the new media and *M. smegmatis* was added to appropriate wells at an MOI of 25. After 1 hour infection, cells were washed twice with 1% BSA in PBS and lifted for 1 hour using 100µL pre-warmed Accutase solution (Sigma #a6964) per well at 37°C. Plate was then moved onto ice and 50µL 1µg/mL DAPI solution was added to each well 2 minutes prior to lifting (pipetting up and down) and assessing AMs and GFP intensity via flow cytometry.

Measurements of ROS production in AMs. 10^4 AMs per well were allowed to adhere to a tissue-culture treated black 96-well fluorescence plate. After 30 minutes in cell culture incubator at 37°C, media was removed, 200uL HHBS was added and removed to wash cells, and 100uL solution of HHBS containing ROS red stain (abcam #ab186027) prepared according to manufacturer's instructions was added to each well. After 1 hour incubation at 37°C, *M. smegmatis* was added to fraction of wells at an MOI of 10 (10^5 bacteria in PBS) via 10µL addition of bacterial solution. Fluorescence measurements were taken at 2, 4, 6, and 24 hours using Ex/Em = 520/605 nm.

pHrodo-stained M. smegmatis intratracheal injections. pHrodo red AM (Invitrogen #P35372) was diluted in 150µL of DMSO. Freshly grown and washed *M. smegmatis* was resuspended into 475µL 100mM $NaHCO_3$ solution to an OD of 4.0, then 25µL pHrodo stock solution was added and allowed to react with bacteria for 2 hours at room temperature on a shaker in the dark. pHrodo-stained bacteria were then washed three times in PBS at 4°C/3000rpm/10min and the OD adjusted to 2.0 (0.2 on nanodrop). The previously described intratracheal infection and characterization protocol with glucose rescue was then followed, before euthanizing mice after 8 hours infection and using PE (pHrodo) and FITC (GFP) channels to analyze change in bacterial uptake vs change in bacterial counts.

Peritoneal infections. 0.1mL of M. smegmatis (adjusted to OD600 of 1.0 or $5x10^7$ CFUs/mL in PBS) is injected intraperitoneally without anesthesia using 30G needle. After 24 hours, mice are euthanized via CO_2 asphyxiation and asphyxiation is confirmed by lack of breathing and heartbeat. Mouse abdomen is sterilized using ethanol, then skin is cut open and pulled such that peritoneum is visualized. 5mL PBS with 5mM EDTA is injected into peritoneal cavity using 28G needle. Peritoneum is massaged for 15 seconds, then fluid is pushed to side of cavity and withdrawn using 20G needle (~4mL can be recovered). Lavage is spun down at 4°C/400g/5min to separate cells – supernatant is collected and serial dilutions are used to assess CFUs recovered by plating on LB agar with 50µg/mL HyB and allowing to grow for 2-3 days at 37°C. The cell pellet is resuspended in 1mL cold complete RPMI at 4°C, after which a fraction is used to count cells via hemocytometer. Cells are spun down at 4°C/400g/5min and washed again with 1mL PBS. Finally, cells are lysed in 200uL PBS + 0.1% Triton-X (pipetting up and down). Cell-lysed solution is serially diluted in PBS and plated onto 50µg/mL HyB LB agar plates as described previously. The

spleen is weighed and 0.025g spleen excised and crushed through 70uM strainer using 5mL syringe plunger. 10mL complete RPMI is used to wash cells through into 10mL conical tube, after which cells are spun down at 4°C/400g/5min, and suspended into 200uL PBS. Cell-lysed solutions are serially diluted and plated for CFUs.

Data analysis and reproducibility – Prism 8.0 by GraphPad was generally used for evaluating data and Student's t-test was used to compare averages. SEMs were plotted on graphs.

References

Chandak, P.G. *et al.* (2010) 'Efficient Phagocytosis Requires Triacylglycerol Hydrolysis by Adipose Triglyceride Lipase *', *Journal of Biological Chemistry*, 285(26), pp. 20192–20201. doi:10.1074/jbc.M110.107854.

Ellson, C.D. *et al.* (2006) 'Neutrophils from p40phox-/- mice exhibit severe defects in NADPH oxidase regulation and oxidant-dependent bacterial killing', *The Journal of Experimental Medicine*, 203(8), pp. 1927–1937. doi:10.1084/jem.20052069.

Hofbauer, S. *et al*. (2015) 'Structure and heme-binding properties of HemQ (chlorite dismutase-like protein) from Listeria monocytogenes', *Archives of Biochemistry and Biophysics*, 574, pp. 36–48. doi:10.1016/j.abb.2015.01.010.

Kanehisa, M. *et al.* (2021) 'KEGG: integrating viruses and cellular organisms.' *Nucleic Acids Research*. 49(D1), D545-D551. doi:10.1093/nar/gkaa970.

Liao, Y. *et al.* (2019) 'WebGestalt 2019: gene set analysis toolkit with revamped UIs and APIs', *Nucleic Acids Research*, 47(W1), pp. W199–W205. doi:10.1093/nar/gkz401.

Appendix 1: Supplementary figures

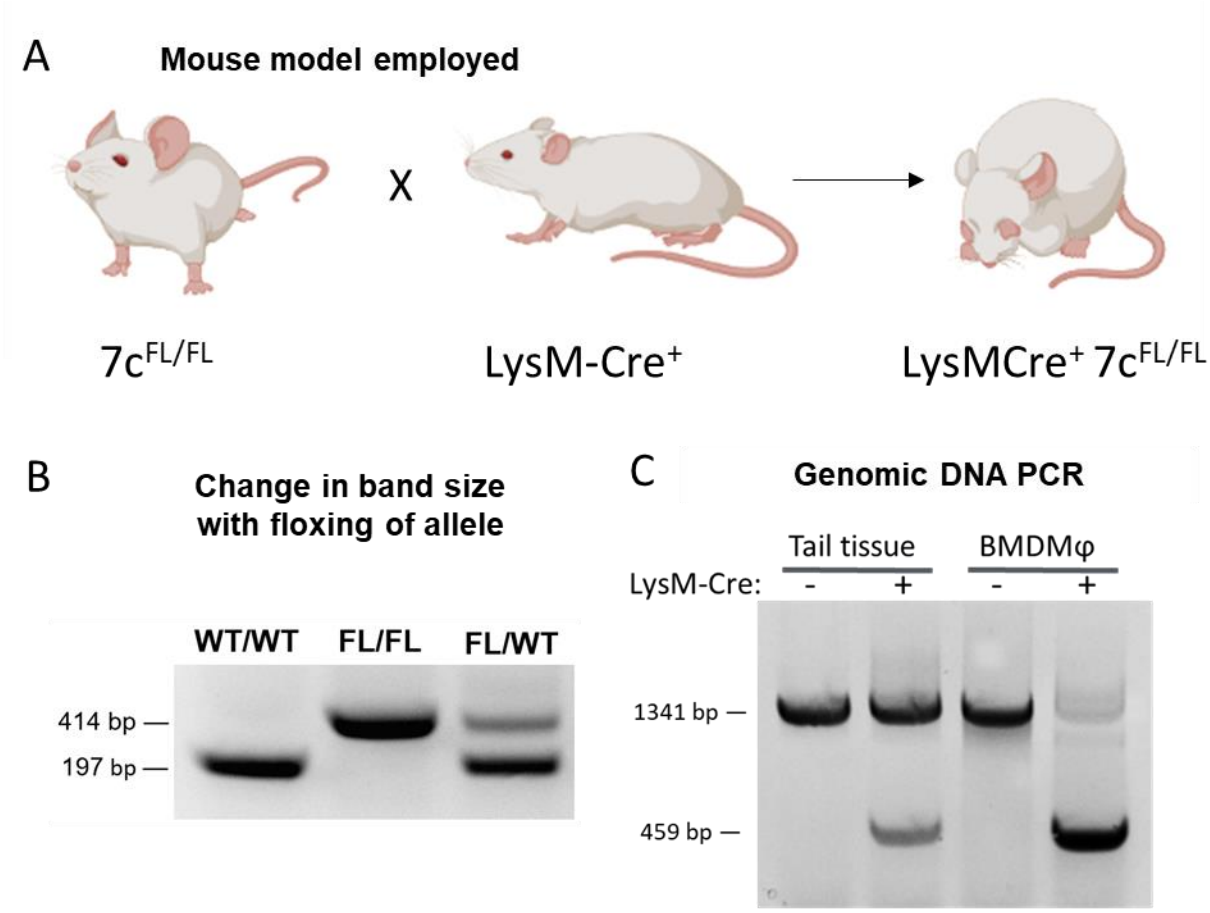

Figure S1 | Macrophage Mfsd7c-knockout model. A) By crossing 7c-floxed mice with LysMCre-positive mice, we generated a LysM-dependent knockout. **B)** Genotyping primers for verifying whether mice are 7c-floxed or not. **C)** LysMCre successfully produces a knockout band when genotyping from tail tissue, and the knockout is complete when genotyping bone marrow-derived macrophages (BMDMs). In this paper, all $7c^{-/-}$ mice discussed are LysMCre conditional deletions.

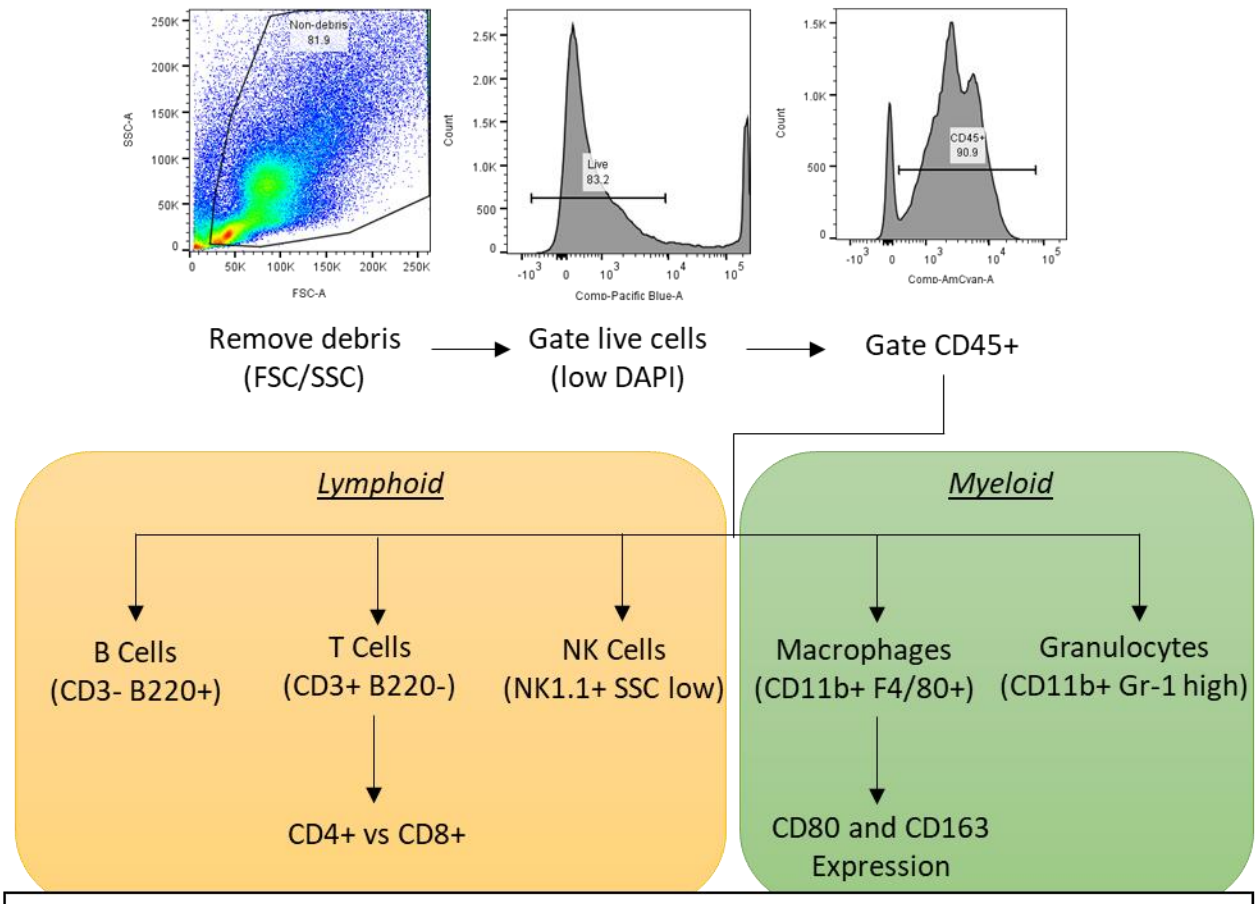

Figure S2 | Flow cytometry gating strategy for immunophenotyping myeloid and lymphoid organs. This will be used for blood, lymph nodes, bone marrow, and spleen.

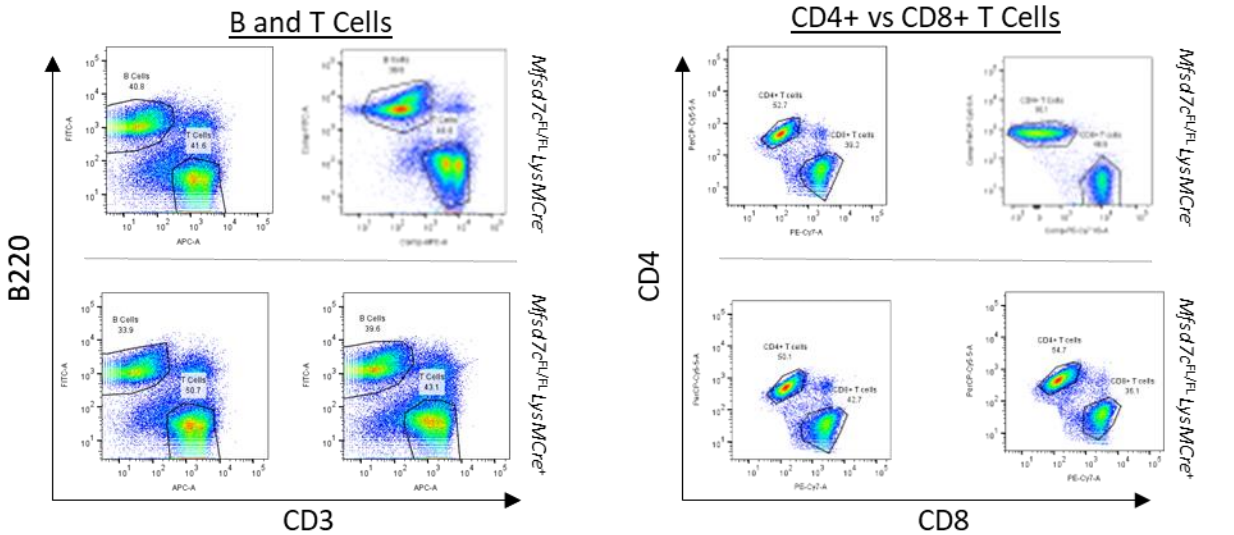

Figure S3 | Immunophenotyping of lymph node. B and $CD4^{+}/CD8^{+}$ T cells were isolated and gated from the lymph node. Counts of each were similar in $7c^{FL/Fl}$and $7c^{-/-}$ mice.

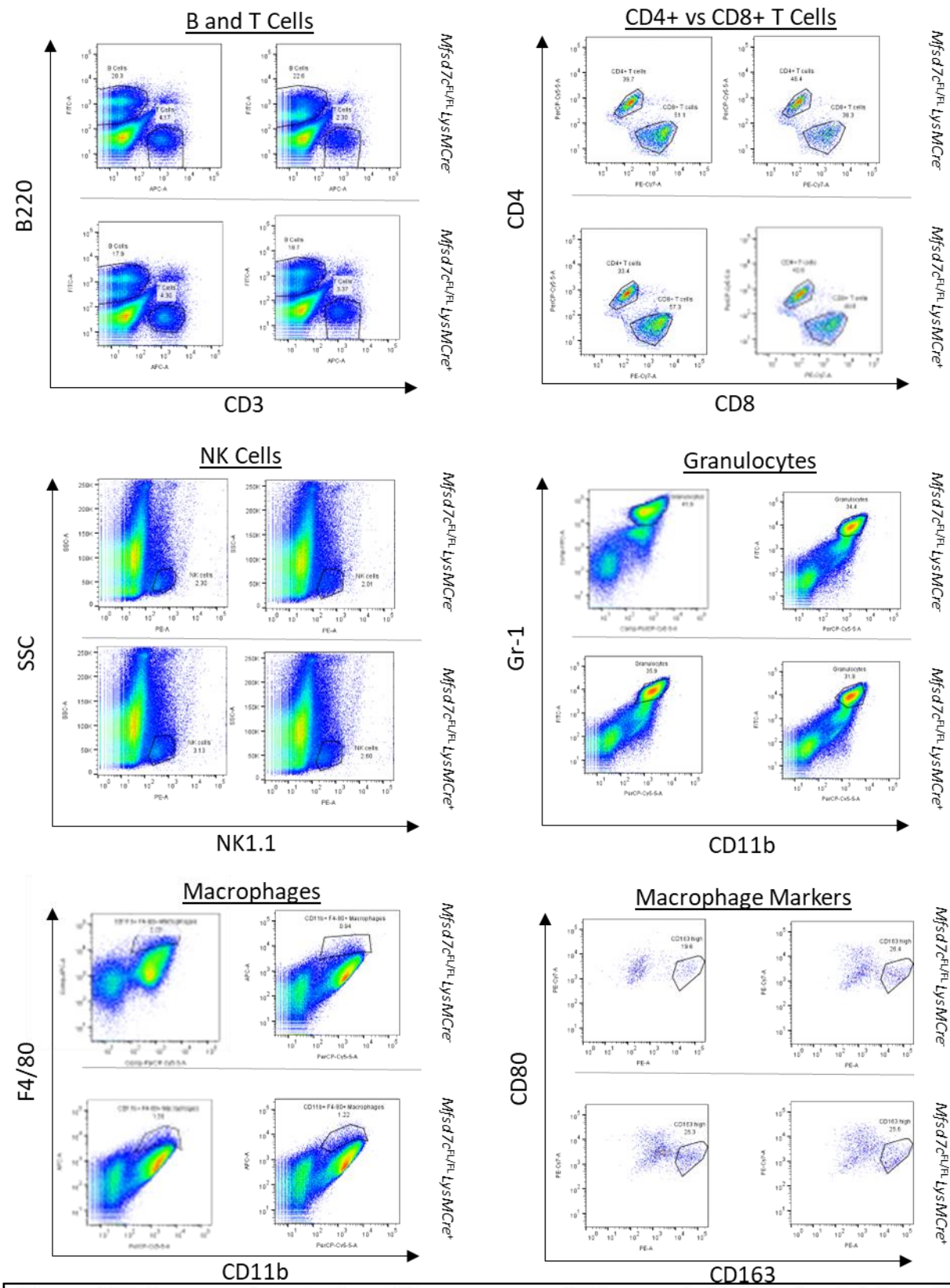

Figure S4 | Immunophenotyping of bone marrow. Cells were isolated and gated from the bone marrow. Counts of each were similar in $7c^{FL/Fl}$ and $7c^{-/-}$ mice.

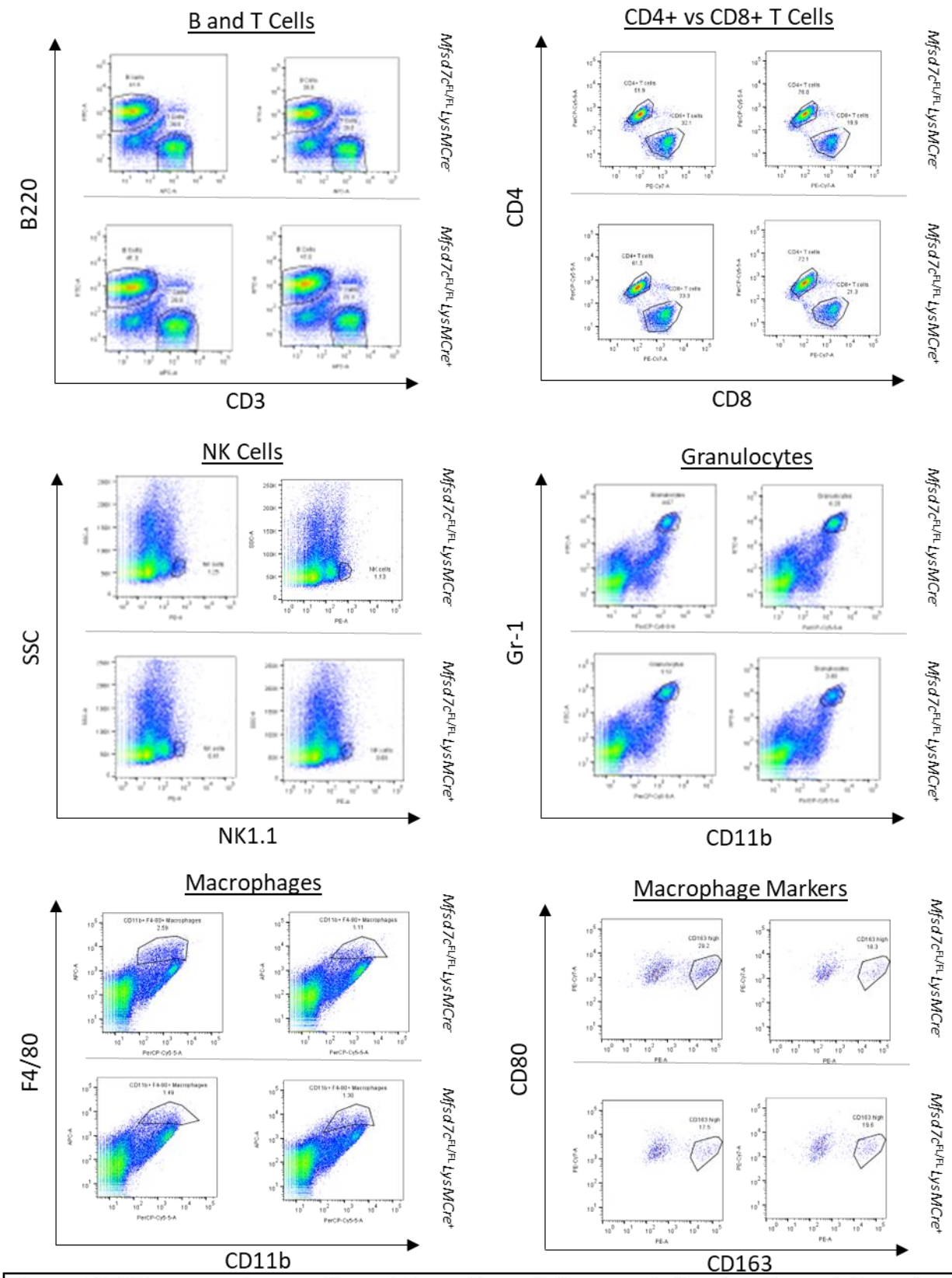

Figure S5 | Immunophenotyping of the spleen. Cells were isolated and gated from the spleen. Counts of each were similar in $7c^{FL/Fl}$ and $7c^{-/-}$ mice.

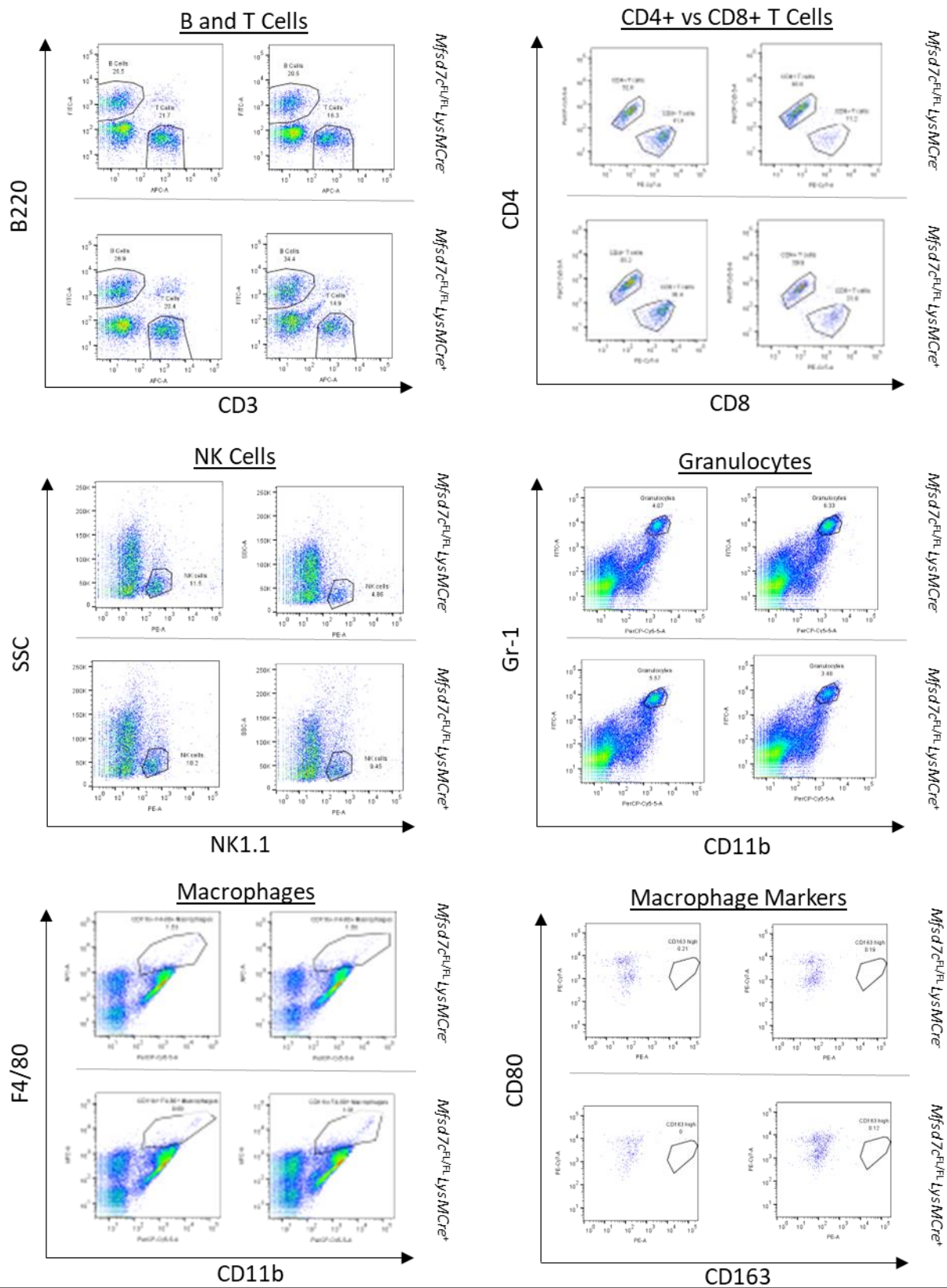

Figure S6 | Immunophenotyping of blood. Cells were isolated and gated from the blood. Counts of each were similar in $7c^{FL/Fl}$ and $7c^{-/-}$ mice.

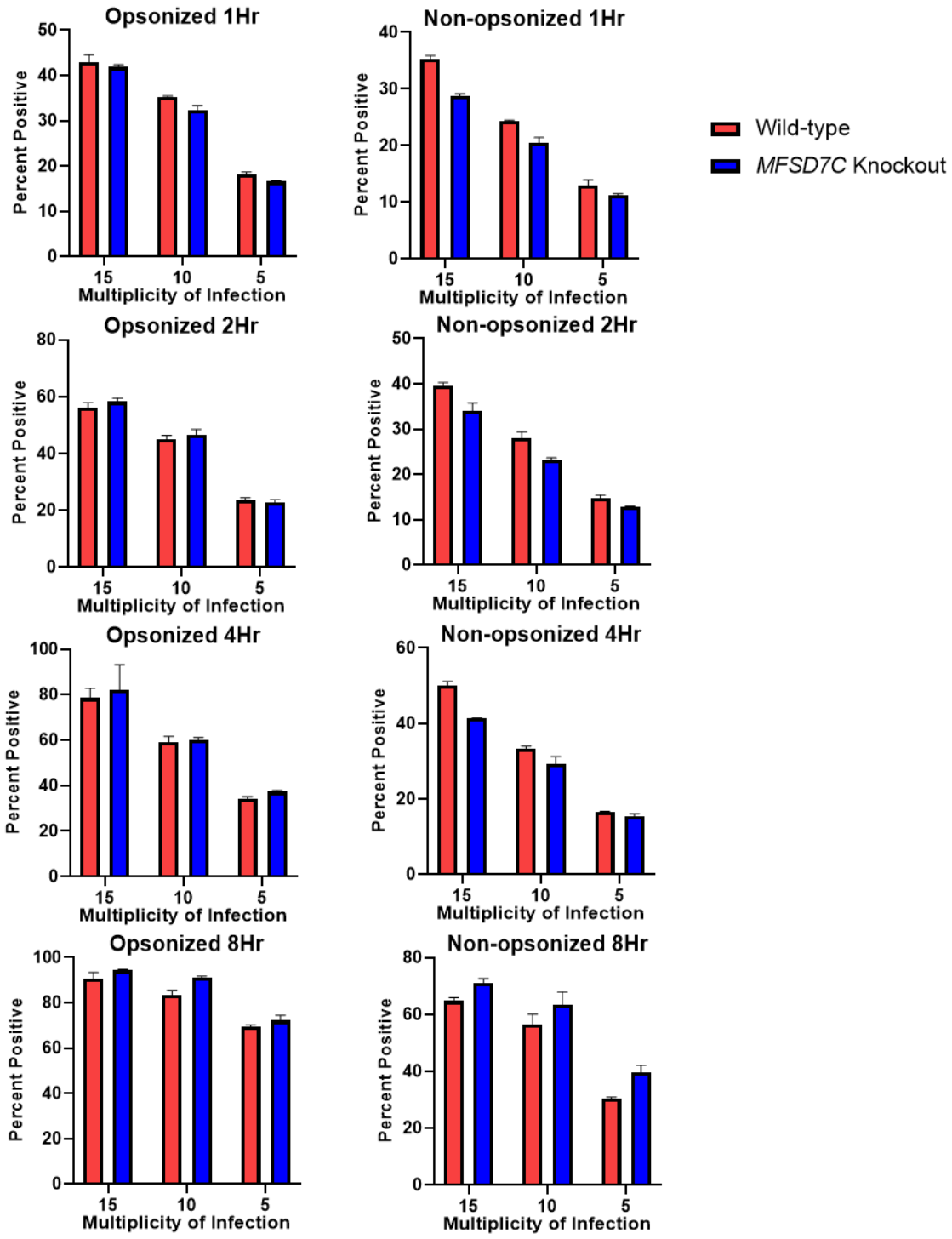

Figure S7 | Phagocytosis of dead *E. coli* bioparticles by WT or 7c$^{-/-}$ THP-1 cells. This assay was repeated multiple times and the 7c-knockout cells tended to have slightly reduced phagocytosis in early time points and then would surpass WT cells by 8 hours. Despite their reproducibility, the differences were never very intense.

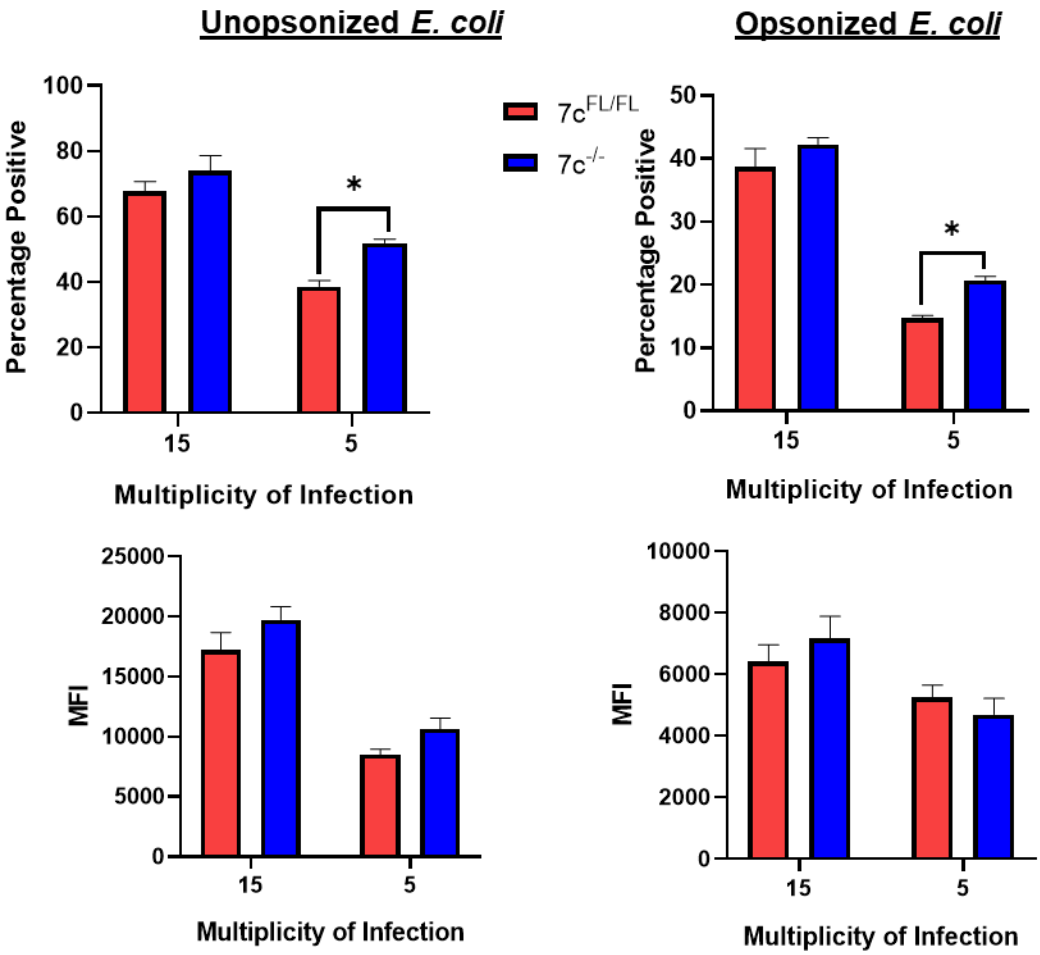

Figure S8 | Bone marrow-derived macrophages phagocytose with similar propensity regardless of 7c status. Most metrics examined showed similar phagocytosis in WT and 7c-deficient BMDMs, but the MOI of 5 taken at 8 hours had a significantly elevated percentage positive, or number of BMDMs with at least one bacteria, for both the unopsonized ($p = 0.0005$) and opsonized ($p = 0.0002$) *E. coli* bioparticles.

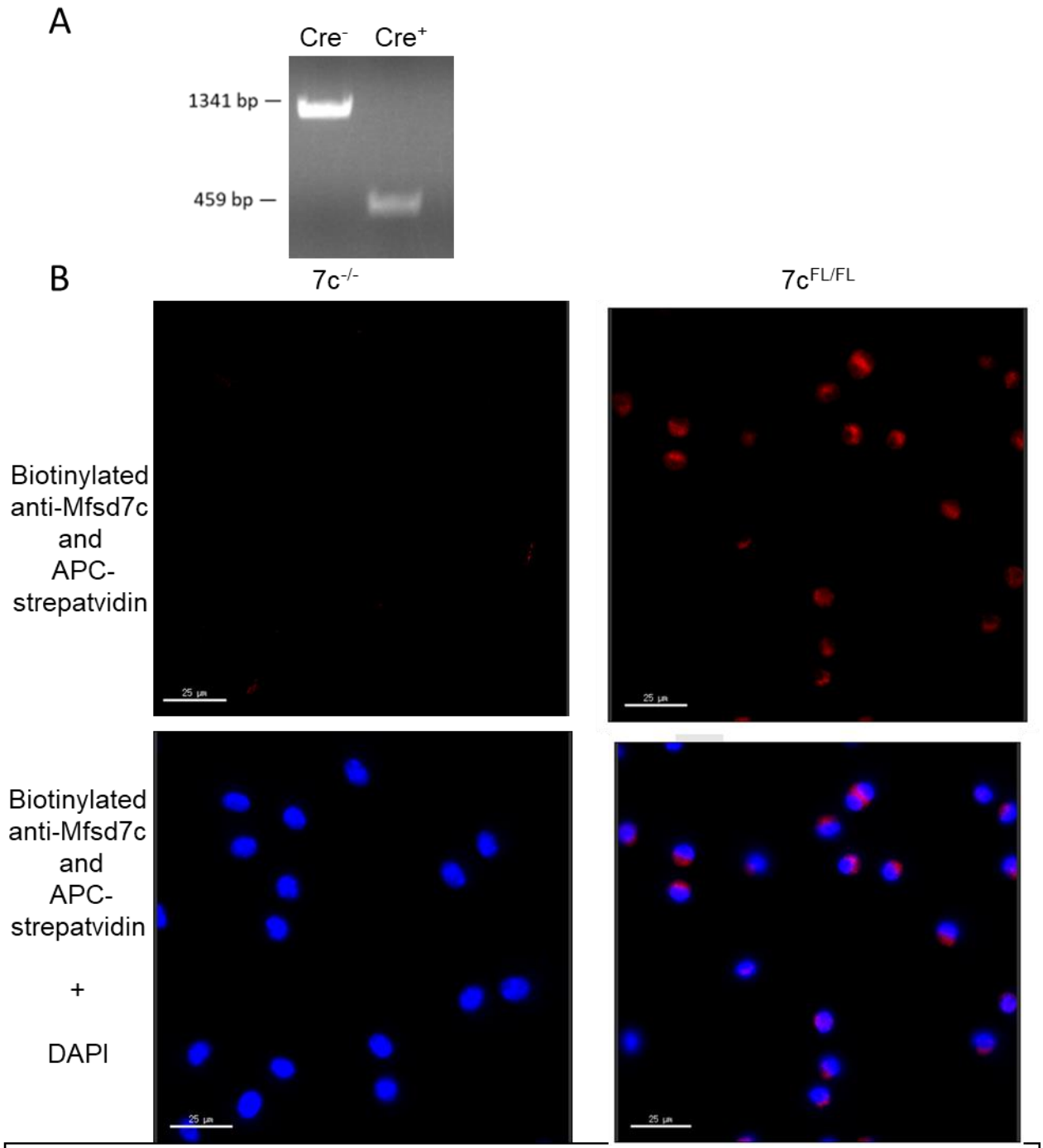

Figure S9 | MFSD7c is knocked out in AMs. A) The PCR band corresponding to the length across the floxed 7c exon 2 is replaced by a shorter band corresponding to the recombined allele when LysMCre is expressed. **B)** AMs were fixed and permeabilized, then stained against MFSD7C with biotinylated antibody on permeabilized AMs and used APC-labled streptavidin to label the biotin (top); the levels on the microscope were thresholded so that the minimum level for detection on the APC channel corresponded to little to no APC visible. This distorts the shown pattern on the $7c^{FL/FL}$ greatly, so the staining pattern should not be utilized for localization. DAPI counterstain was added and both channels put together (bottom).

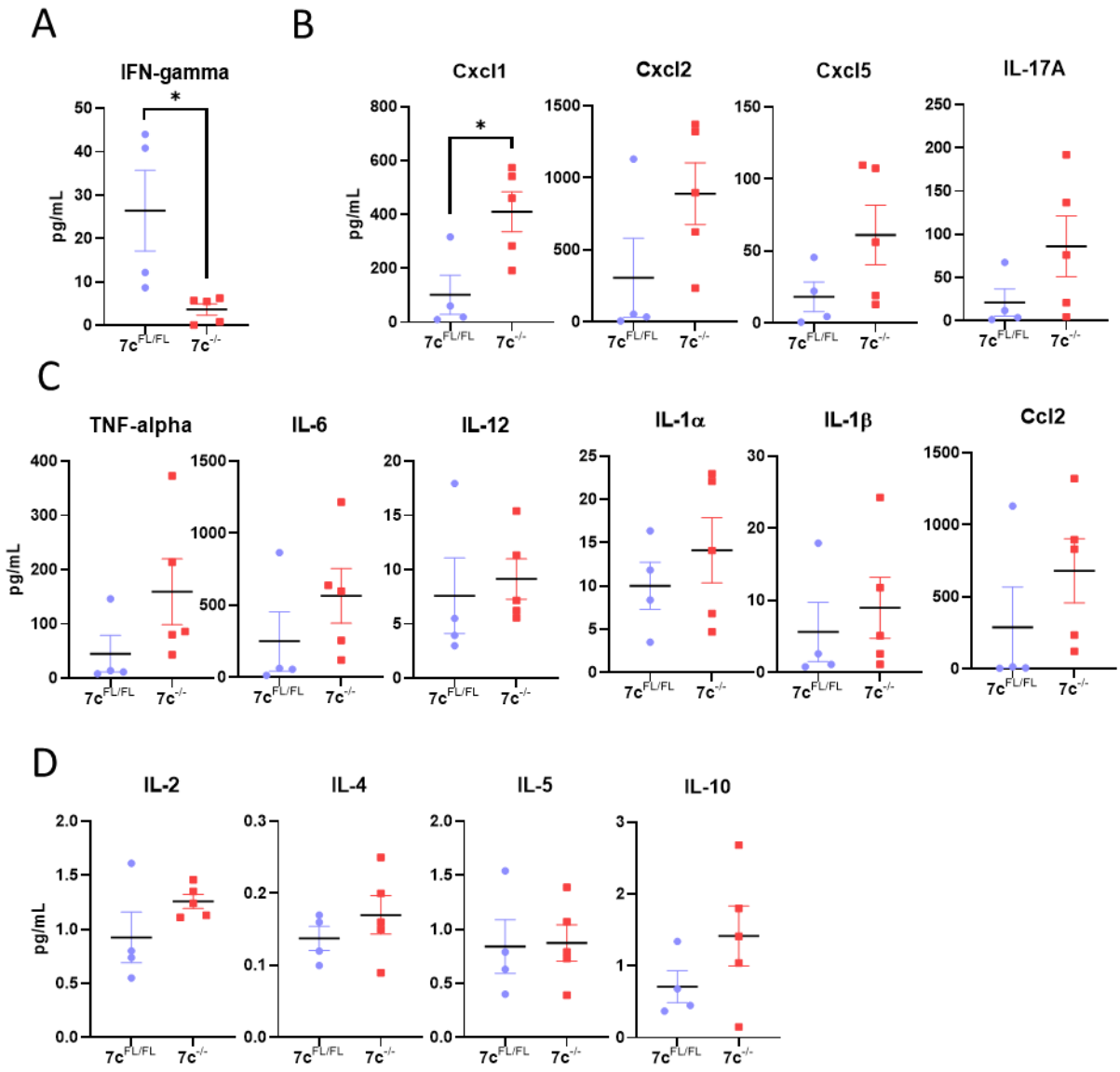

Figure S10 | Cytokine profile of $7c^{FL/FL}$ versus $7c^{-/-}$ lung surfactants after 24 hours *M. smegmatis* infection. The only significant changes are downregulation of IFN-gamma (**A**, p = 0.0287) and upregulation of Cxcl1 (p = 0.0223) in $7c^{-/-}$ AMs. The cytokines in **B** represent neutrophil chemoattractant, the cytokines in **C** are proinflammatory, and the cytokines in **D** are T cell-secreted and modulate the nature of the immune response.

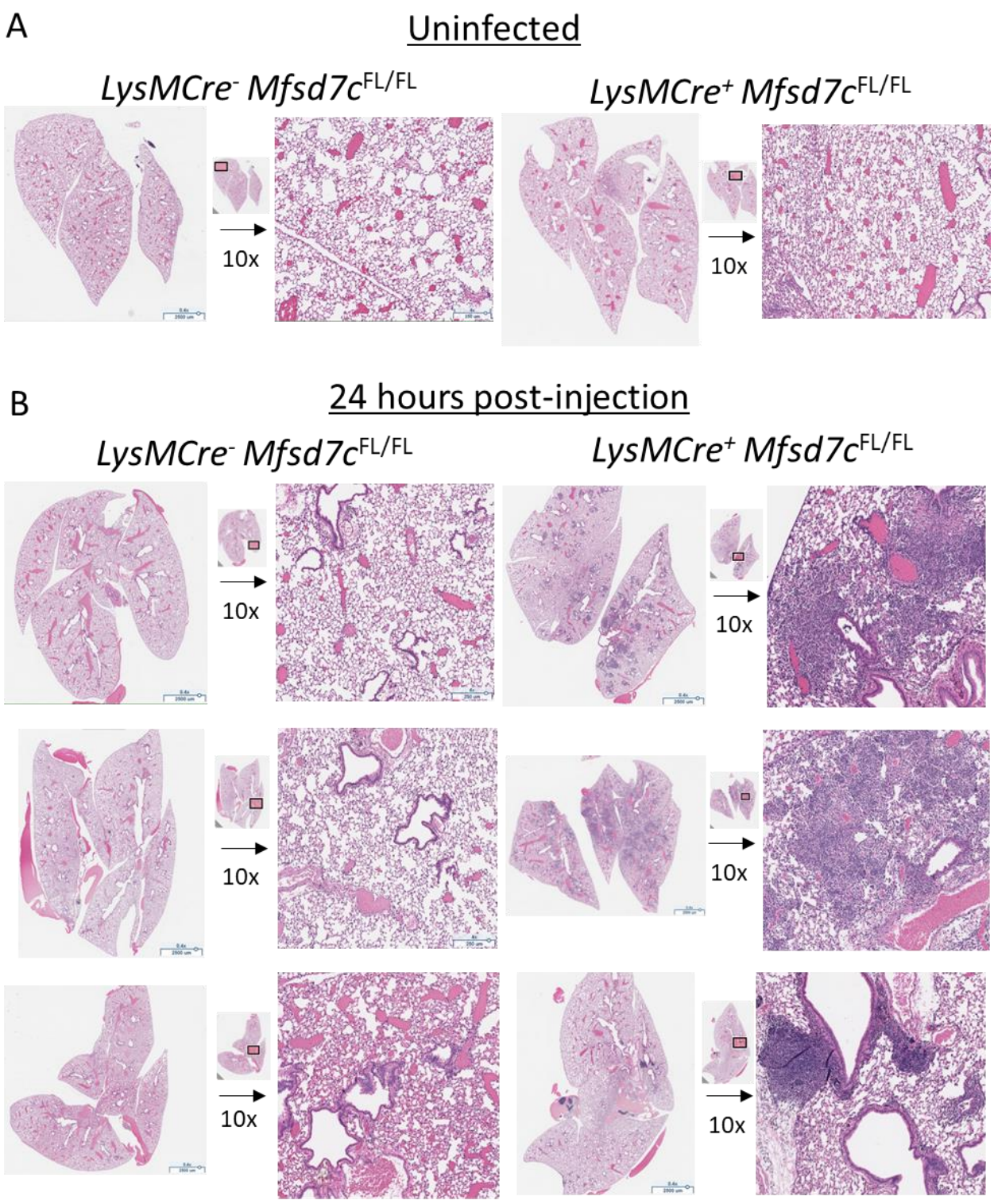

Figure S11 | $7c^{-/-}$ lungs infected with *M. smegmatis* demonstrate increased leukocyte infiltration. A) Uninfected $7c^{FL/FL}$ (left) and $7c^{-/-}$ (right) lungs both appear normal. **B)** Lungs harvested 24 hours after intratracheal injection with *M. smegmatis* reveal that lungs from $7c^{-/-}$ mice have increased leukocyte infiltration.

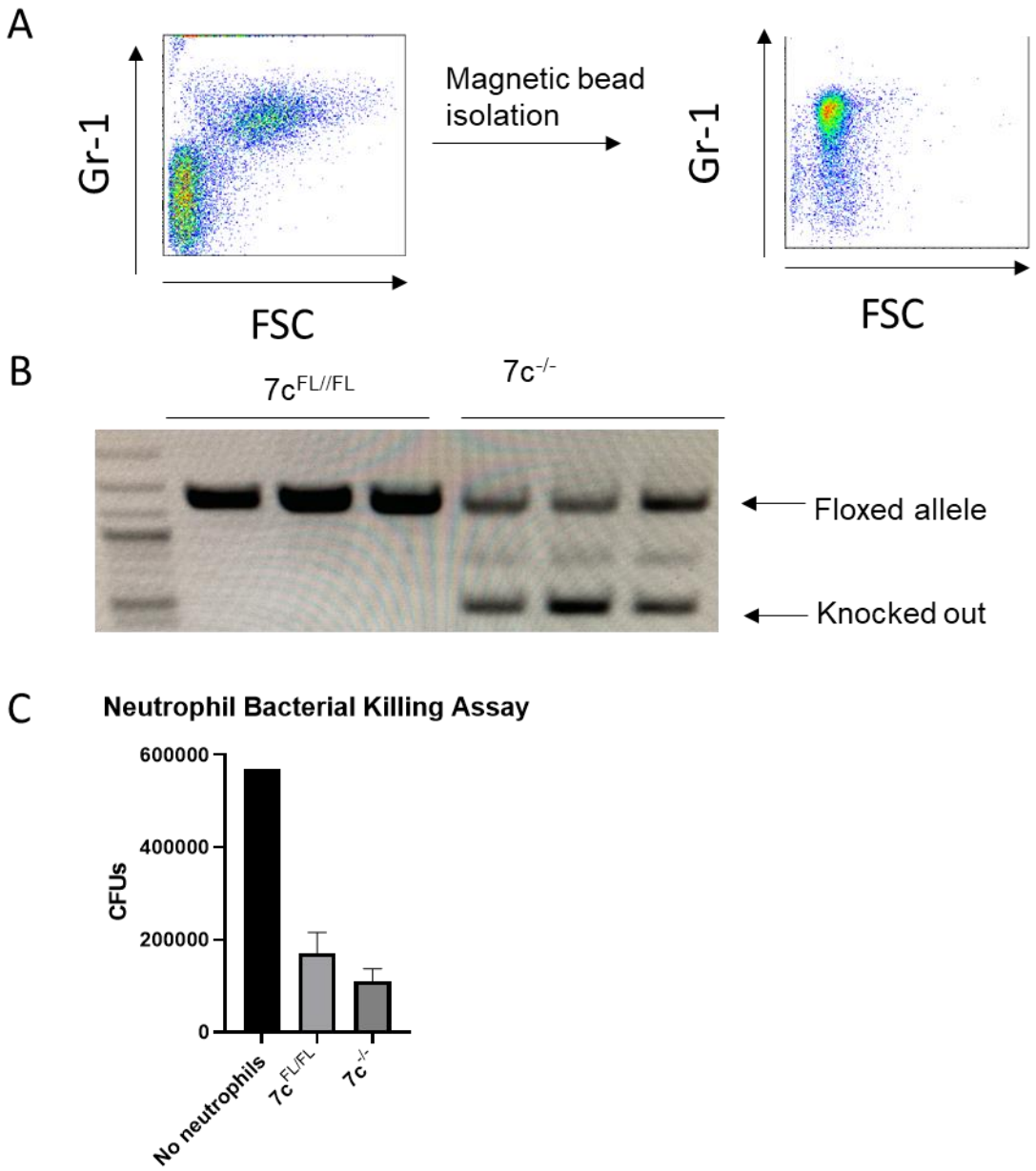

Figure S12 | 7c is knocked out in neutrophils but 7c$^{-/-}$ neutrophils do not demonstrate inferior bacterial killing in vitro. A) Neutrophils were isolated from bone marrow and purified using a magnetic isolation kit; purity of each sample was ~90% neutrophils. **B)** Neutrophils were genotyped and it was demonstrated that 7c$^{-/-}$ mice do generate neutrophils with PCR bands corresponding to knocked out 7c. **C**) Neutrophils were activated and bacterial killing of *M. smegmatis* was assayed for 1 hour at an MOI of 1; 7c$^{-/-}$ neutrophils did not demonstrate impaired killing associated with an elevated CFU count.

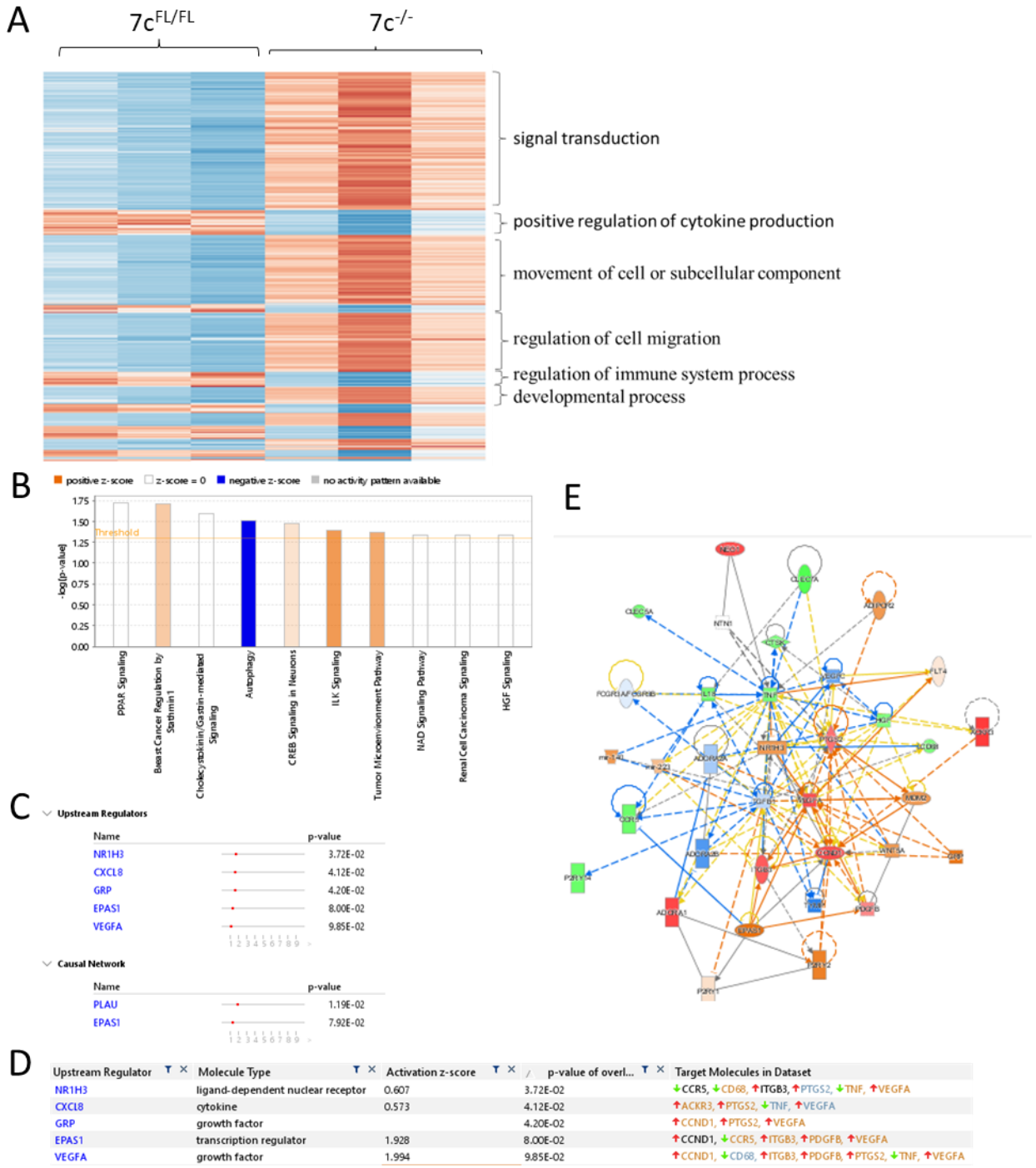

Figure S13 | Examination of most significantly differentially expressed genes between 7c$^{FL/FL}$ AMs and 7c$^{-/-}$ AMs. A) Clustering followed by overrepresentation analysis showed the most common pathways associated with each cluster for only the most significantly differentially expressed genes. **B)** These genes were also used in an Ingenuity Pathway Analysis canonical pathway analysis; significant pathways are displayed. **C)** Potential upstream regulators or causal networks were associated with the observed transcriptional changes, and **D**) information obtained pertaining to those upstream regulators. **E)** A pathway was created to explain some data found in the analysis.

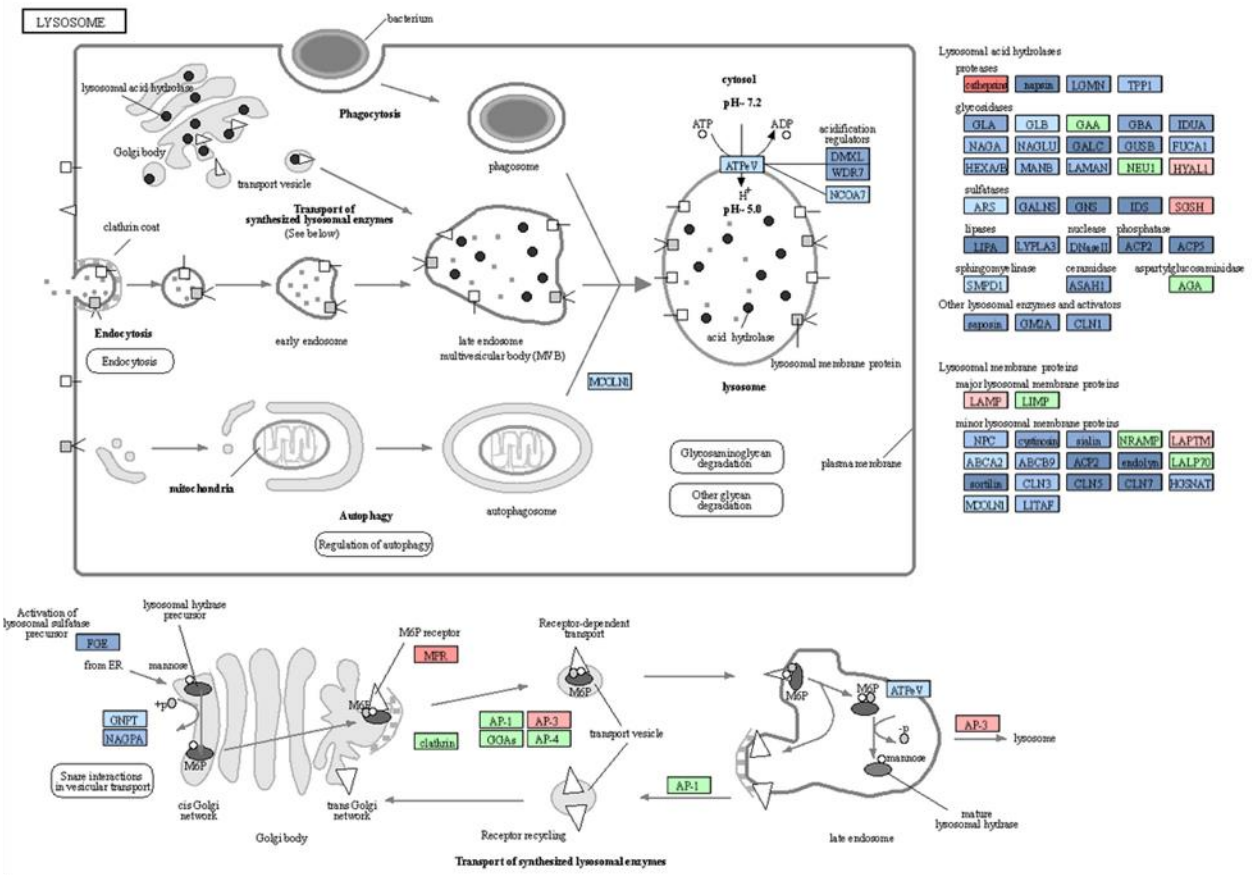

Figure S15 | Changes in transcript values in $7c^{-/-}$ versus $7c^{FL/FL}$ AMs for KEGG Lysosome Pathway (mmu04142) . Blue boxes indicate that the transcript is downregulated at least 25% in $7c^{-/-}$ AMs vs $7c^{FL/FL}$ AMs (dark blue indicates >2-fold decrease), while red indicates that the transcript is upregulated at least 25% in $7c^{-/-}$ AMs vs $7c^{FL/FL}$ AMs (bright red indicates >2-fold increase). White and green boxes represent transcripts that were altered <25% between $7c^{-/-}$ and $7c^{FL/FL}$ AMs or not detected in sufficient abundance from RNAseq (green boxes show genes that differ significantly among species; shown here is a mouse pathway map).

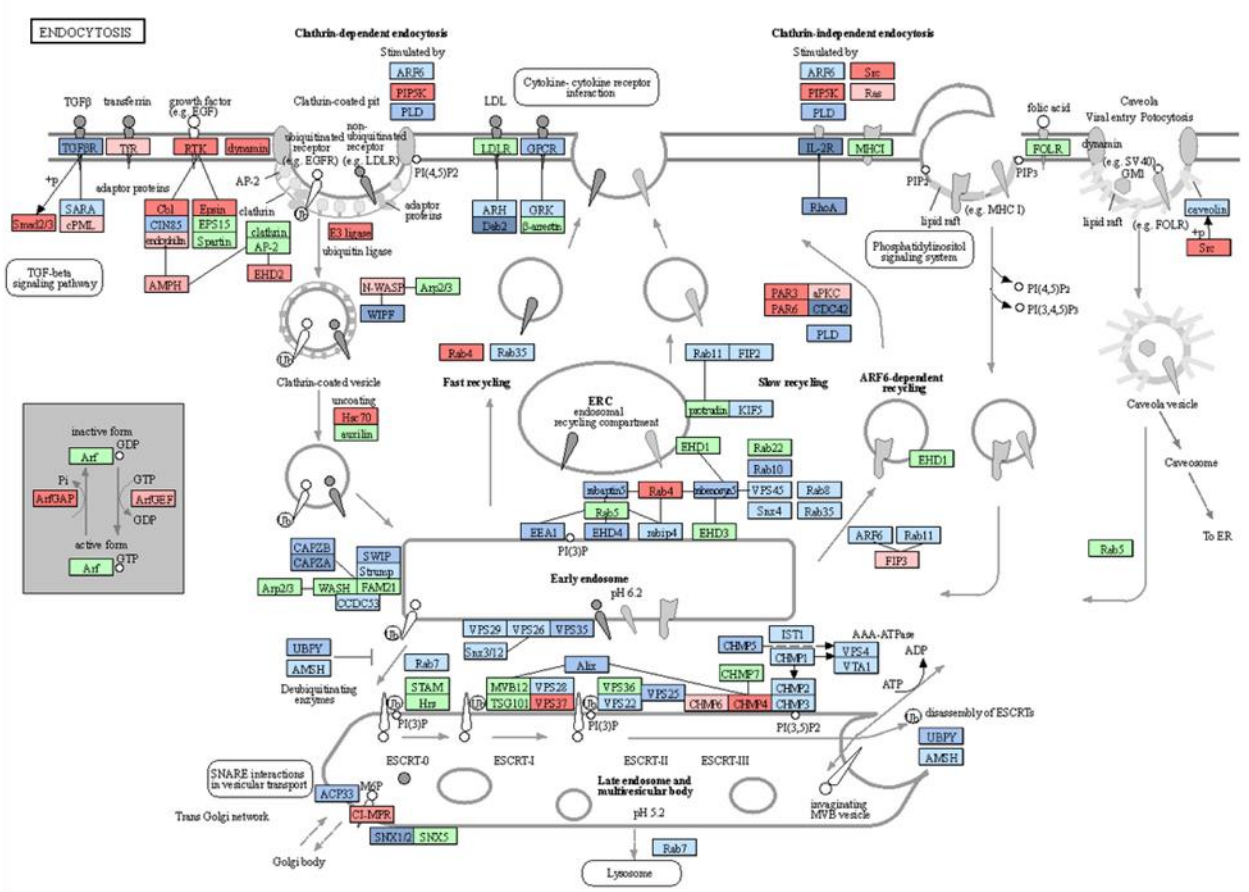

Figure S16 | Changes in transcript values in $7c^{-/-}$ versus $7c^{FL/FL}$ AMs for KEGG Endocytosis Pathway (mmu04144) . Blue boxes indicate that the transcript is downregulated at least 25% in $7c^{-/-}$ AMs vs $7c^{FL/FL}$ AMs (dark blue indicates >2-fold decrease), while red indicates that the transcript is upregulated at least 25% in $7c^{-/-}$ AMs vs $7c^{FL/FL}$ AMs (bright red indicates >2-fold increase). White and green boxes represent transcripts that were altered <25% between $7c^{-/-}$ and $7c^{FL/FL}$ AMs or not detected in sufficient abundance from RNAseq (green boxes show genes that differ significantly among species; shown here is a mouse pathway map).

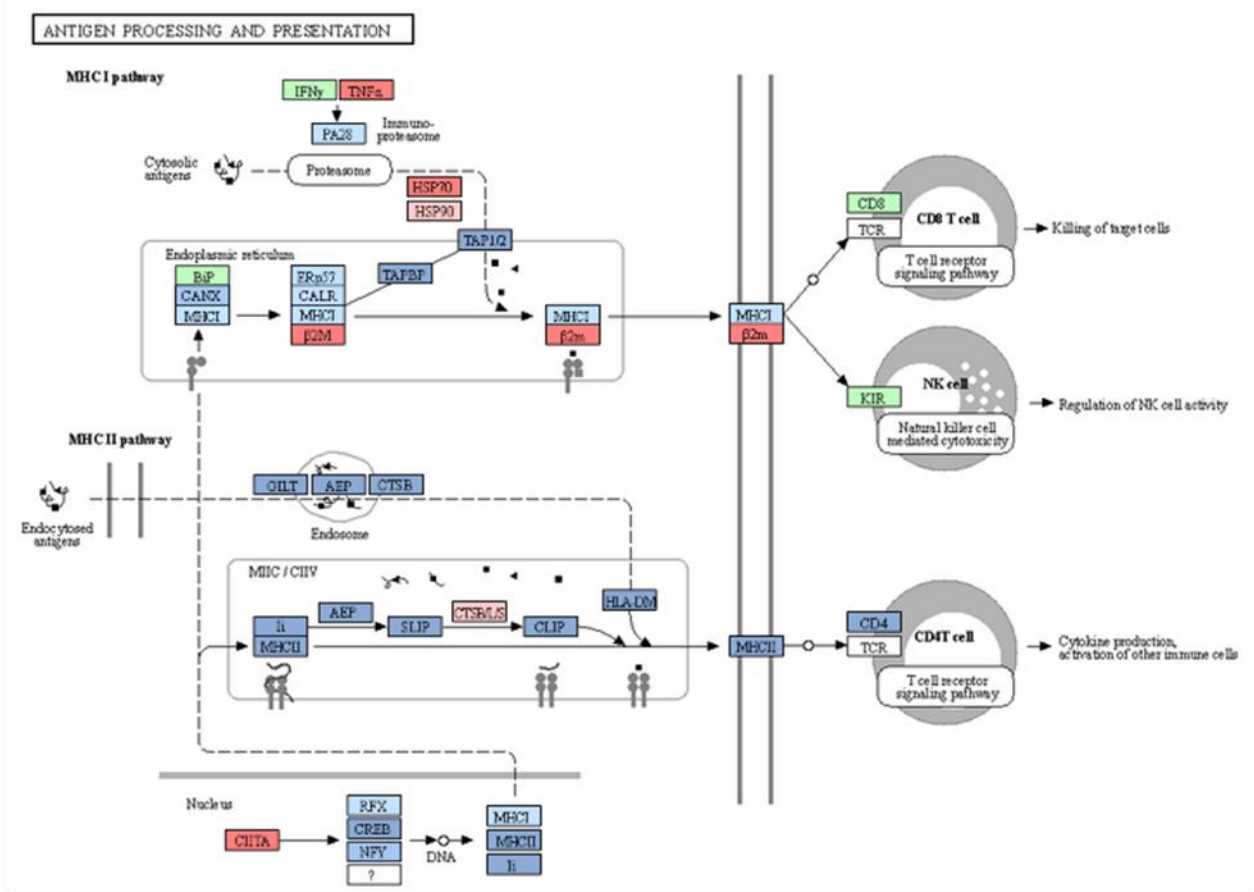

Figure S17 | Changes in transcript values in $7c^{-/-}$ versus $7c^{FL/FL}$ AMs for KEGG Antigen Processing and Presentation Pathway (mmu04612) . Blue boxes indicate that the transcript is downregulated at least 25% in $7c^{-/-}$ AMs vs $7c^{FL/FL}$ AMs (dark blue indicates >2-fold decrease), while red indicates that the transcript is upregulated at least 25% in $7c^{-/-}$ AMs vs $7c^{FL/FL}$ AMs (bright red indicates >2-fold increase). White and green boxes represent transcripts that were altered <25% between $7c^{-/-}$ and $7c^{FL/FL}$ AMs or not detected in sufficient abundance from RNAseq (green boxes show genes that differ significantly among species; shown here is a mouse pathway map).

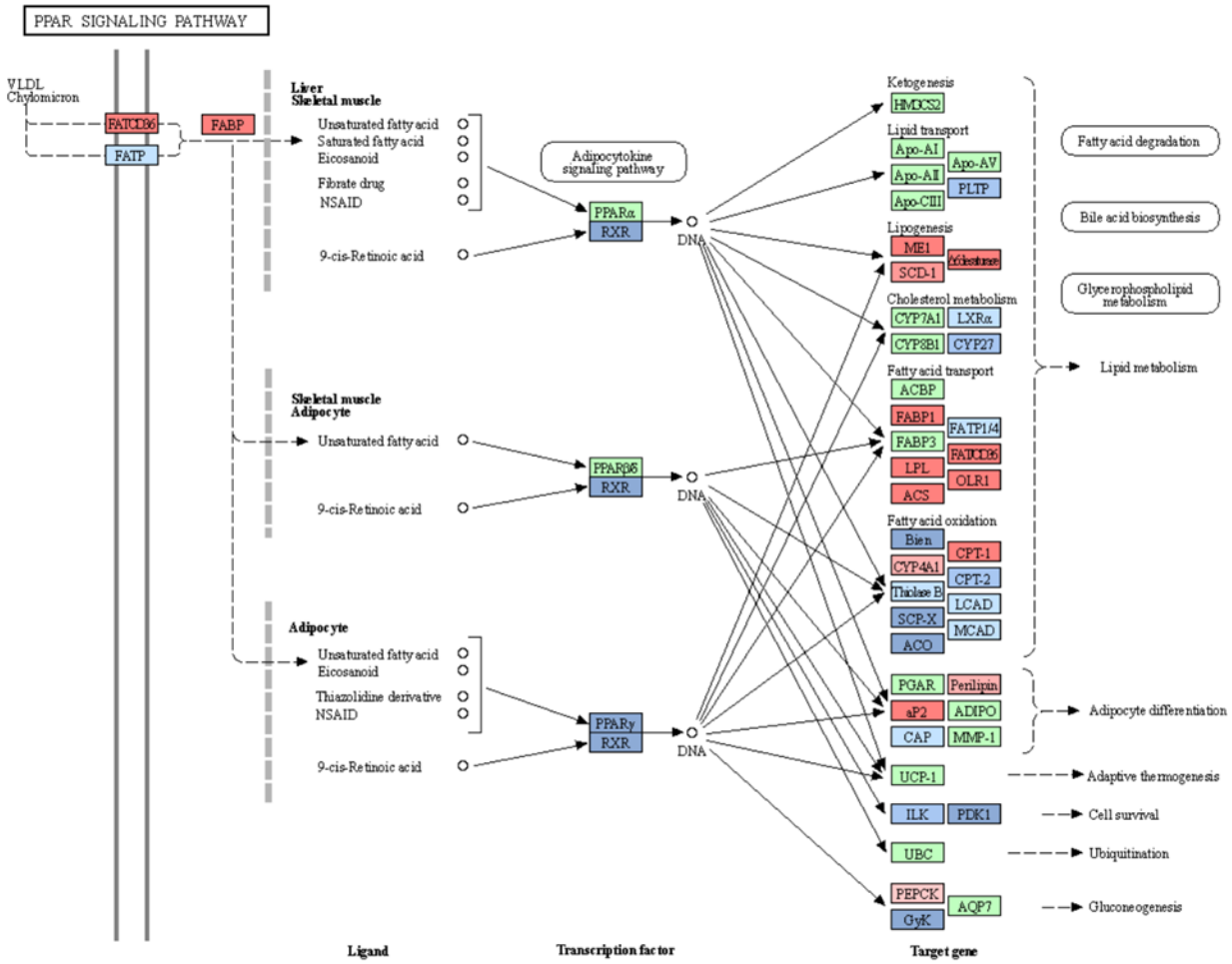

Figure S18 | Changes in transcript values in $7c^{-/-}$ versus $7c^{FL/FL}$ AMs for KEGG PPAR Signaling Pathway (mmu03320) . Blue boxes indicate that the transcript is downregulated at least 25% in $7c^{-/-}$ AMs vs $7c^{FL/FL}$ AMs (dark blue indicates >2-fold decrease), while red indicates that the transcript is upregulated at least 25% in $7c^{-/-}$ AMs vs $7c^{FL/FL}$ AMs (bright red indicates >2-fold increase). White and green boxes represent transcripts that were altered <25% between $7c^{-/-}$ and $7c^{FL/FL}$ AMs or not detected in sufficient abundance from RNAseq (green boxes show genes that differ significantly among species; shown here is a mouse pathway map).

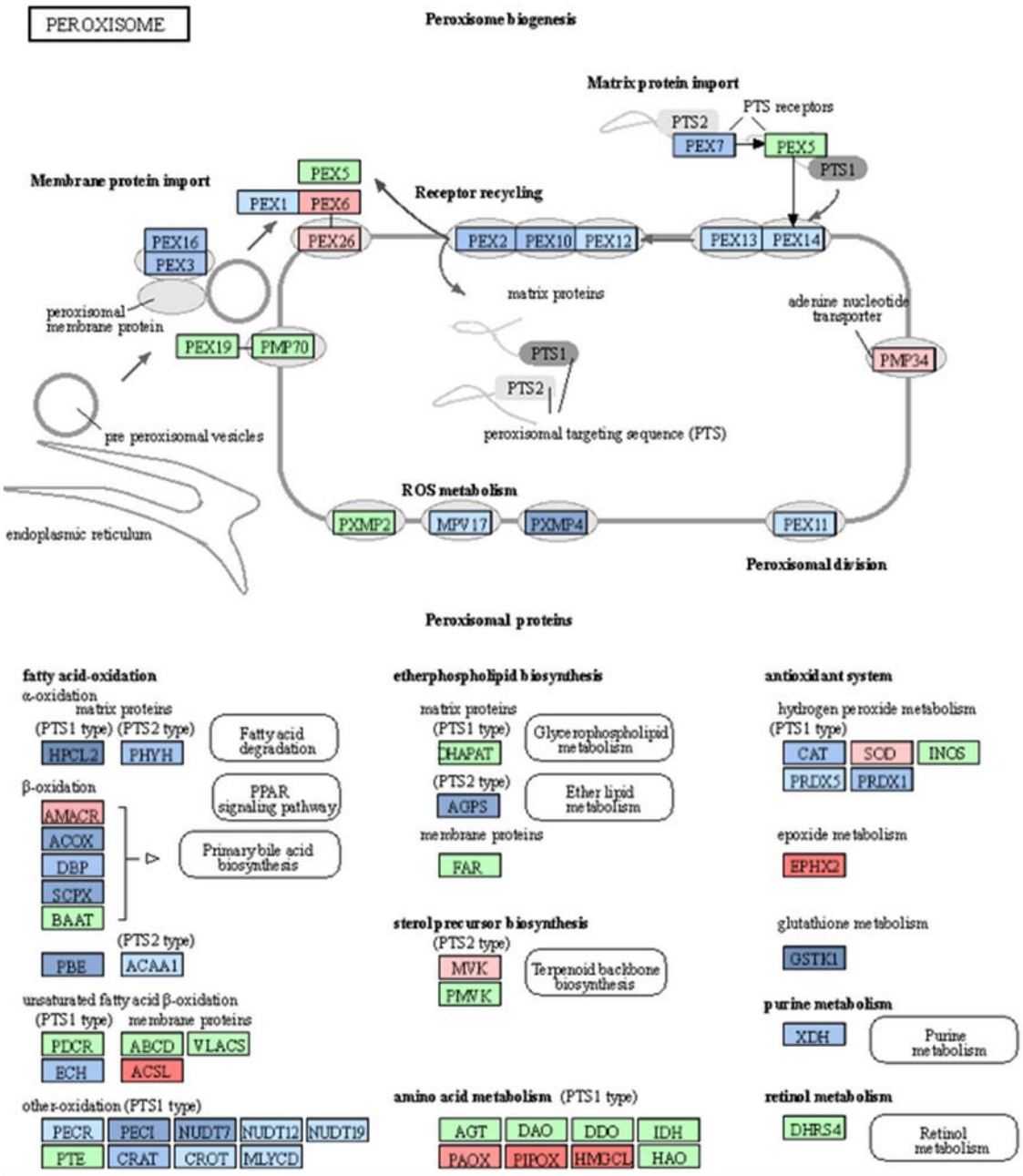

Figure S19 | Changes in transcript values in $7c^{-/-}$ versus $7c^{FL/FL}$ AMs for KEGG Peroxisome Pathway (mmu04146) . Blue boxes indicate that the transcript is downregulated at least 25% in $7c^{-/-}$ AMs vs $7c^{FL/FL}$ AMs (dark blue indicates >2-fold decrease), while red indicates that the transcript is upregulated at least 25% in $7c^{-/-}$ AMs vs $7c^{FL/FL}$ AMs (bright red indicates >2-fold increase). White and green boxes represent transcripts that were altered <25% between $7c^{-/-}$ and $7c^{FL/FL}$ AMs or not detected in sufficient abundance from RNAseq (green boxes show genes that differ significantly among species; shown here is a mouse pathway map).

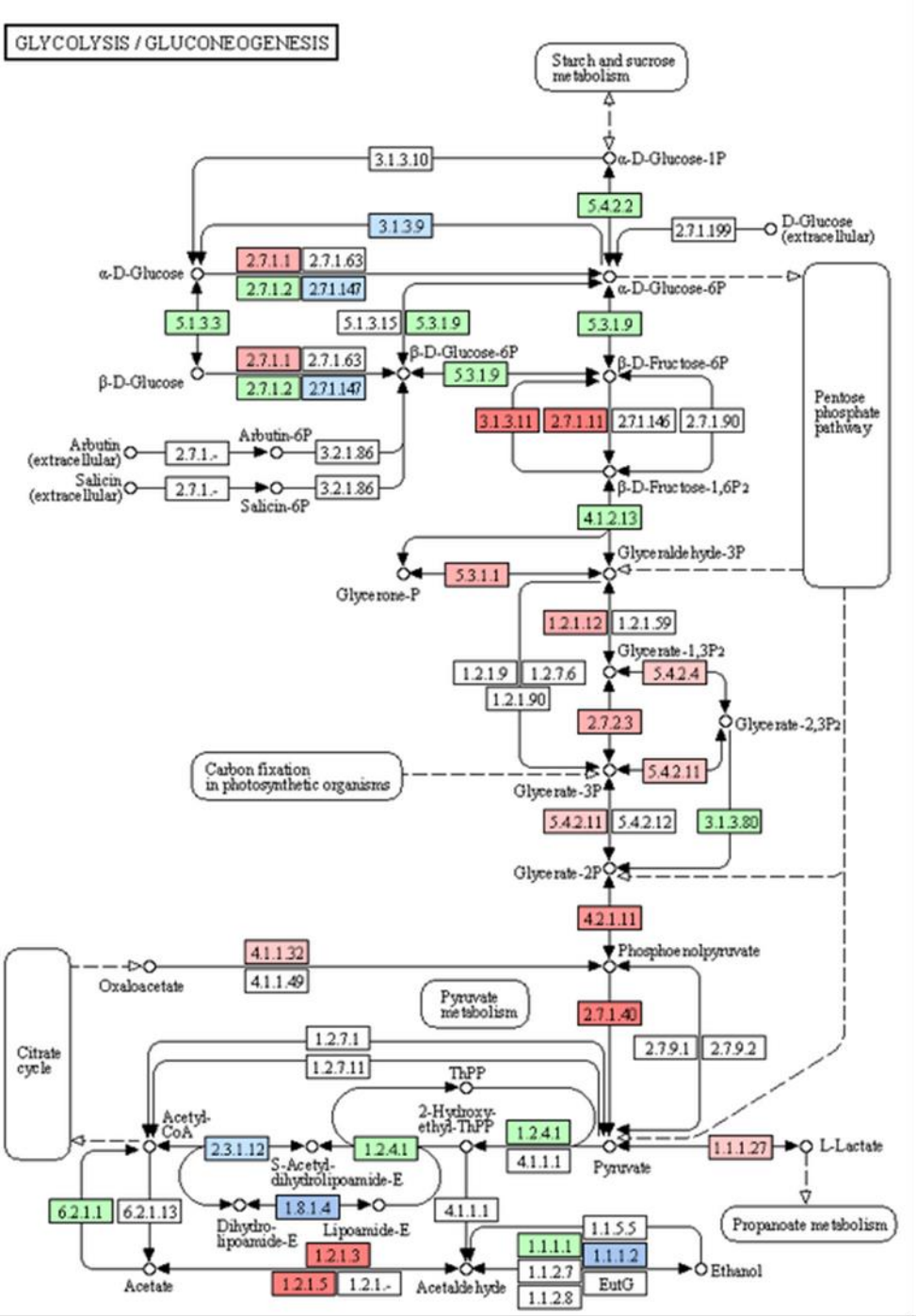

Figure S20 | Changes in transcript values in 7c$^{-/-}$ versus 7c$^{FL/FL}$ AMs for KEGG Glycolysis/ Gluconeogenesis Pathway (mmu00010) . Blue boxes indicate that the transcript is downregulated at least 25% in 7c$^{-/-}$ AMs vs 7c$^{FL/FL}$ AMs (dark blue indicates >2-fold decrease), while red indicates that the transcript is upregulated at least 25% in 7c$^{-/-}$ AMs vs 7c$^{FL/FL}$ AMs (bright red indicates >2-fold increase). White and green boxes represent transcripts that were altered <25% between 7c$^{-/-}$ and 7c$^{FL/FL}$ AMs or not detected in sufficient abundance from RNAseq (green boxes show genes that differ significantly among species; shown here is a mouse pathway map).

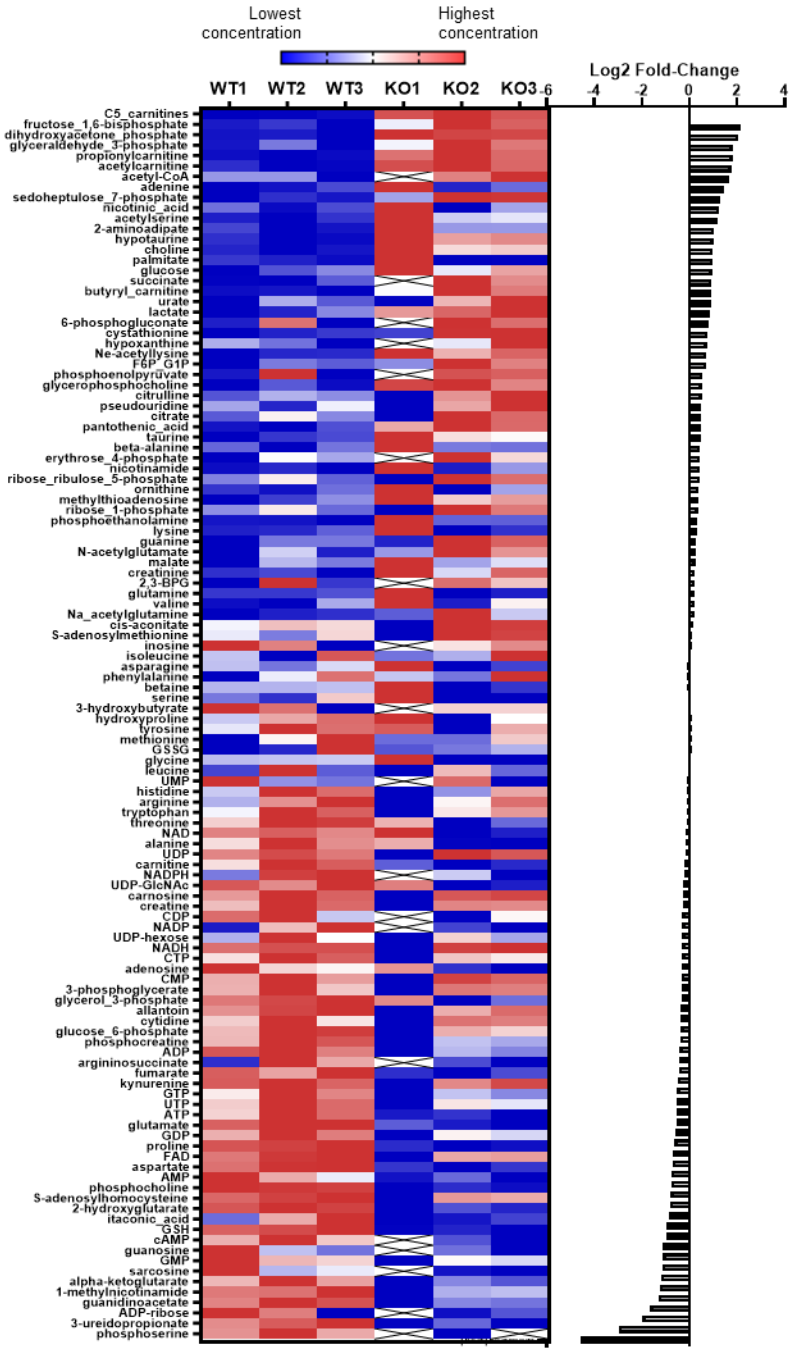

Figure S21 | Changes in metabolite concentrations obtained from three replicates of THP-1 7c$^{-/-}$ versus WT THP-1 cells. HILIC positive-ion LC/MS was performed and metabolites compared between WT and 7c$^{-/-}$ (KO) THP-1 cells. For the heat map on the left, red boxes indicate metabolite levels above the average and blue boxes indicate expression levels below the average. The bar chart to the right depicts the log2-fold change for each metabolite with positive values representing increased concentrations found in the 7c-knockout THP-1 cells.

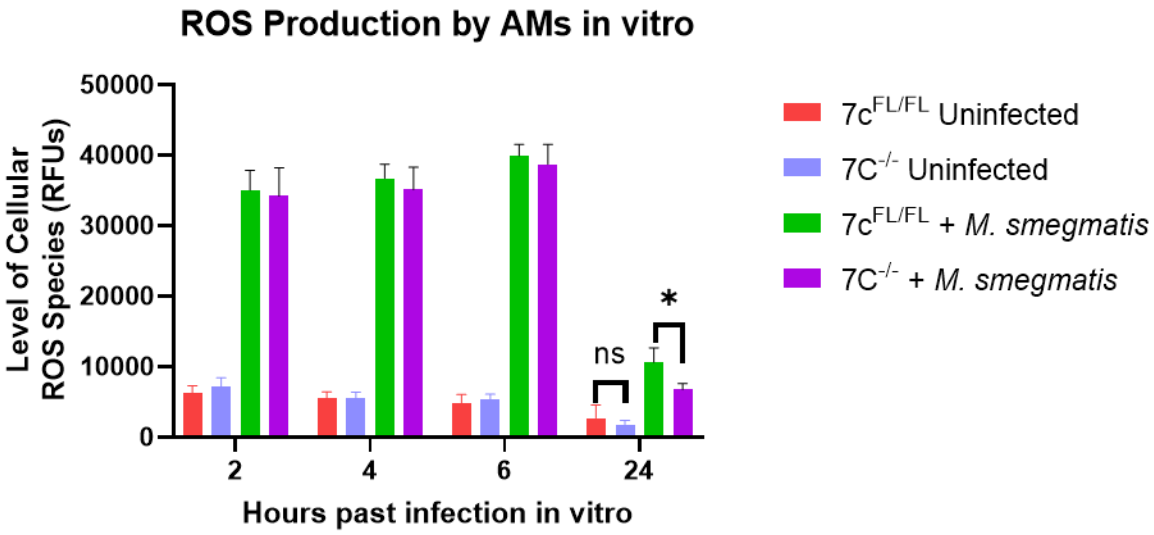

Figure S22 | Comparison of cellular ROS production between $7c^{-/-}$ and $7c^{FL/FL}$ AMs in vitro. 10^4 AMs from three mice per genotype were used to compare ROS production by both uninfected and *M. smegmatis*-infected (MOI 10) AMs. Only at the 24hr time point was any significant difference observed, wherein infected $7c^{FL/FL}$ continued to produce ROS at higher levels than the $7c^{-/-}$ AMs ($p = 0.0358$).

Chapter 3: Mfsd7c affects ATP transport in alveolar macrophages

Contribution acknowledgments

I wrote this chapter, performed experiments and interpreted the data with the help of Nikola A. Ivica, Yuwen Yin, and my thesis advisor Professor Jianzhu Chen. Nikola A. Ivica isolated the protein MFSD7C and optimized the protocol for thermal shift.

Abstract

Despite having previously demonstrated metabolic effects of MFSD7C$^{-/-}$ cells *in vitro* and now Mfsd7c$^{-/-}$ alveolar macrophages *in vivo*, the substrate of this transporter remains unclear. We perform a substrate screen using a thermal shift design with purified MFSD7C in order to assess potential candidates based on their ability to stabilize the protein against denaturation at a normally destabilizing temperature. From this screen, we identify ATP as a potential substrate and validate MFSD7C's ability to impute 32P-ATP uptake into bacteria that express it. We find that heme increases this rate of uptake and based on the observed kinetics examine whether heme affects ATP transport in mouse alveolar macrophages. We find that heme is able to significantly and rapidly upregulate ATP secretion in Mfsd7c-expressing macrophages, suggesting potential mechanisms for how it might affect metabolism *in vivo* as well as providing an immediate answer as to how heme might rapidly increase thermogenesis *in vitro* utilizing MFSD7C.

Introduction

Despite the report by Duffy et al. in 2010 (Duffy et al. 2010) that MFSD7C is a heme importer, numerous groups have had difficulty reconciling their results with that notion (Ponka et al. 2017). Our lab could not replicate those results in cell lines, and assessing ZnMP (a fluorescent heme analog used in the original experiments) uptake in AMs yields the same finding once again (**Supplemental Figure S23**). Based on our group's prior insight into MFSD7C, and now with new insight into the protein's role *in vivo*, the determination of the transport substrate would clarify many of the findings and phenotypes we have witnessed.

Our data from cell lines supports a knockout phenotype characterized by decreased ATP levels, increased oxygen consumption, and increased thermogenesis. We still do not understand whether this is due to a phenotype of uncoupling of the mitochondria, whereby the proton gradient across the mitochondrial inner membrane is utilized for heat generation rather than ATP production, or due to activity by a SERCA ATPase whereby calcium gradients are created and eliminated with the only functional contribution of this cycle being generation of heat (Primeau et al. 2018). Furthermore, certain components of this phenotype seem to be somewhat at odds with our hypotheses, particularly the role of heme addition to *MFSD7C*-expressing cells in phenocopying the *MFSD7C*$^{-/-}$ phenotype. The intuitive explanation would be that heme inhibits MFSD7C, but this is not necessarily what we have observed in other assays. To help clarify how exactly MFSD7C creates the observed phenotypes, we aim to identify its substrate and better understand the protein's mechanism of action.

Results and discussion

Thermostability shift assay screen reveals ATP is a candidate substrate for MFSD7C

In order to identify MFSD7C's substrate, a thermal shift screen was designed based on Majd et al's published strategy (Majd et al. 2018) for determining the substrate of a transmembrane transporter. Critical to this method's success is the existence of cysteine residues hidden away from a reactive dye until thermal denaturation begins, five of which are present in MFSD7C's structure. Using aliquots of previously purified MFSD7C protein, we add protein, CPM (a cysteine-reactive dye that increases in fluorescence following an irreversible reaction), and substrate to be screened to each well of a 96-well PCR plate. We then examine the fluorescence of each well over time as the temperature of the plate is slowly increased in a qPCR instrument (Roche Lightcycler 480). As the protein begins to denature, the hidden cysteine residues become exposed and react with the CPM dye, resulting in an increase in fluorescence. When the protein's substrate is present, the bonds between substrate and transporter stabilize the transporter's conformation and elevate the temperature required to achieve denaturation. This is apparent on the qPCR machine by an increase in the temperature required to achieve increased fluorescence from the CPM dye.

Using this methodology, we examined the denaturation curve of purified MFSD7C in buffer with only the vehicle buffer present (no candidate substrates) to establish the baseline curve and relevant inflection point from which to later identify changes. However, purified MFSD7C protein contained two such inflection points **(Figure 8A**) which were more apparent when examining the derivative of the curve (**Figure 8B**). This indicates that the different domains of MFSD7C (the structure includes two six-transmembrane domains characterized as duplicates of a

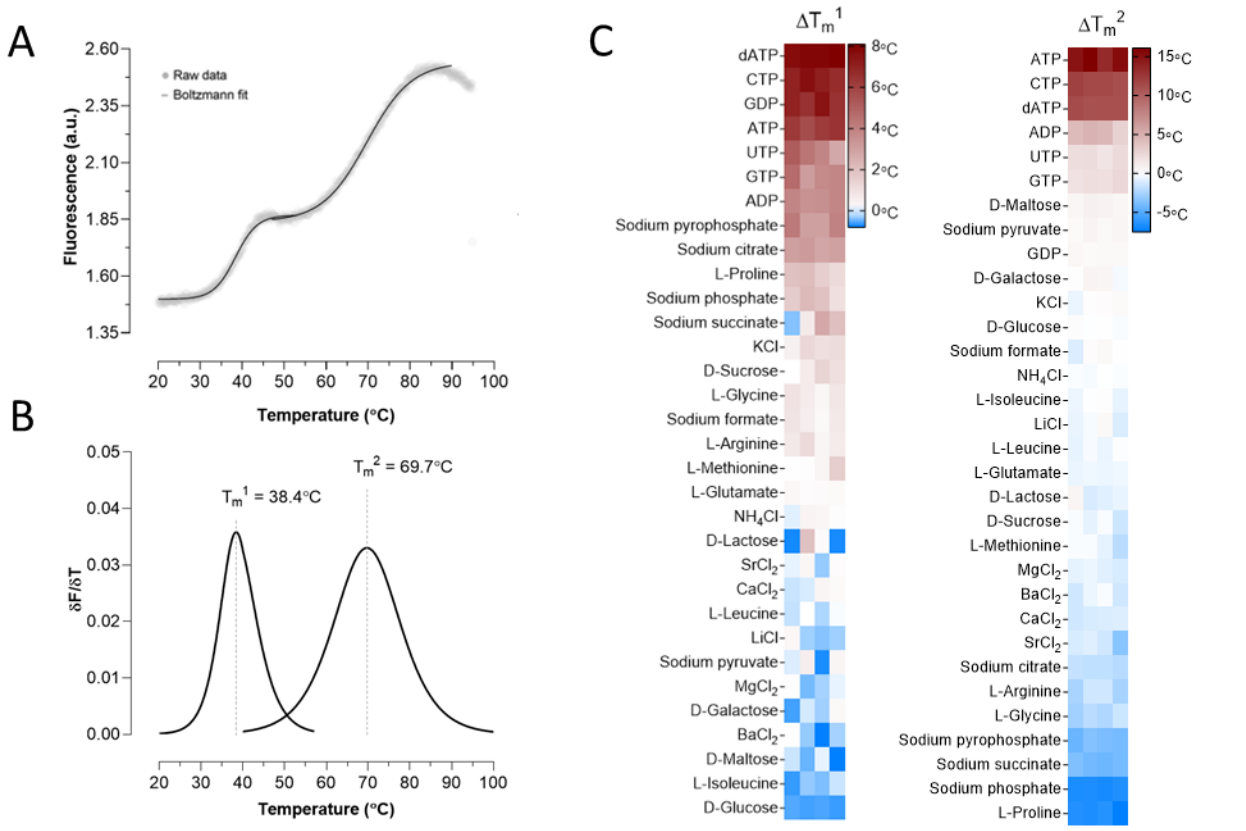

Figure 8 | A thermal shift screen for the substrate of MFSD7C suggests ATP as a candidate. **A)** Purified human MFSD7C protein in detergent demonstrates a bimodal thermal denaturation profile characterized by two distinct inflection points in the fluorescence absorption that increases as the protein unfolds. **B)** The derivative of the denaturation profile marks the locations of the two inflection points, an early point at 38.4°C and a later point at 69.7°C. **C)** Putative substrates were screened and the observed alterations to the two inflection points were characterized based on the extent and direction to which the compound shifted each point (blue = shifted inflection temperature down; red = shifted inflection temperature up). dATP most significantly increased the first inflection point, or T_m^1, and ATP most significantly increased the second inflection point, or T_m^2.

once three-transmembrane domain, as seen on all MFS proteins). The existence of these two separate peaks indicated that each potential ligand would be assessed for its ability to modulate each inflection point separately, because thermal shifts did not necessarily affect both curves equally (though they generally did**, Figure 8C)**. The screen was conducted with substrates at 10mM concentrations and revealed that nucleotide phosphates were most strongly able to elevate the inflection point of the denaturation curves.

The inflection temperature for the T_m^2 curve is more similar to previously reported melting temperatures for membrane proteins in this assay (Majd et al. 2018) than that of T_m^1, so the candidates that affect T_m^2 were considered more promising than those that perturb T_m^1. The compound that stabilized T_m^2 most strongly was ATP, increasing the melting temperature by approximately 15°C, and ATP was also one of the top hits for T_m^1. With this in mind, we pursued a strategy to better address whether ATP was indeed the substrate for MFSD7C.

E. coli expressing MFSD7C uptake increased levels of 32P-ATP

Klein et al. previously reported AXER was an ATP-transporting protein by using a system of 32P-ATP uptake by *E. coli* that is increased when bacteria express an ATP transporter (Klein et al. 2018). The central methodology is that *E. coli* membranes are impermeable to ATP under normal conditions, so adding a protein that allows for 32P-ATP uptake indicates that the protein is likely to transport ATP. The radioactivity from ATP contained within the *E. coli* can be assessed after a relatively rapid wash of the extracellular ATP, which is important if the protein rapidly transports ATP because the gradients will be altered once the wash is initiated. The protocol we employed involved first coincubating an appropriate quantity of bacteria with the specified concentration of α-32P ATP, then moving the ATP and bacteria together into a syringe filter directly before the endpoint of the uptake. The extracellular ATP was then rapidly flushed away via the filter, and the *E. coli* left behind as well as any residual wash buffer (which now might start receiving ATP down the concentration gradient) were eluted in scintillation fluid for radioactivity quantification via liquid scintillation counting.

We initialized our experiments by assessing whether *E. coli* induced to express higher levels of MFSD7C using IPTG could uptake higher levels of 32P ATP than either the uninduced *E. coli* expressing low levels of MFSD7C or negative control bacteria expressing an empty plasmid

(**Figure 9A**). We found that the bacteria containing the MFSD7C plasmid that were induced to express high levels of protein did indeed uptake the highest quantity of ATP, but the rates of uptake were more rapid than expected (the induction comparison was performed after only 5 minutes coincubation with ATP).

We then set out to assess how rapidly the *E. coli* induced to express high levels of 32P ATP would uptake it, using radioactivity as our proxy measurement. We found that the induced bacteria reached saturation in just 10 minutes (**Figure 9B**), but that the radioactivity of the empty vector also exposed to an induction protocol would randomly shift around at relatively low counts per million (CPM), likely indicating nonspecific binding rather than gradual uptake.

Using the 5-minute time point for ease of reproducibility as well as levels below radioactivity saturation, we assessed whether heme levels proximal to our previously described k_d of 1μM on the N-terminal domain were capable of modulating ATP. We found that there was an increase in the radioactivity measured at 5 minutes when levels of heme at 5uM or above were added to the *E. coli* 3 minutes prior to 32P ATP coincubation **(Figure 9C**). With this knowledge, we assessed the kinetics of 32P uptake on bacteria either expressing MFSD7C and exposed to heme or just PBS or bacteria expressing an empty vector and exposed to heme or PBS **(Figure 9D).** We found that heme increased the rate of 32P ATP entry into the cell, repeating the time points taken at 3 minutes, when levels were quite different between *E. coli* expressing empty vector, expressing MFSD7C but untreated, and expressing MFSD7C and exposed to heme to demonstrate significance and reproducibility **(Figure 9E**).

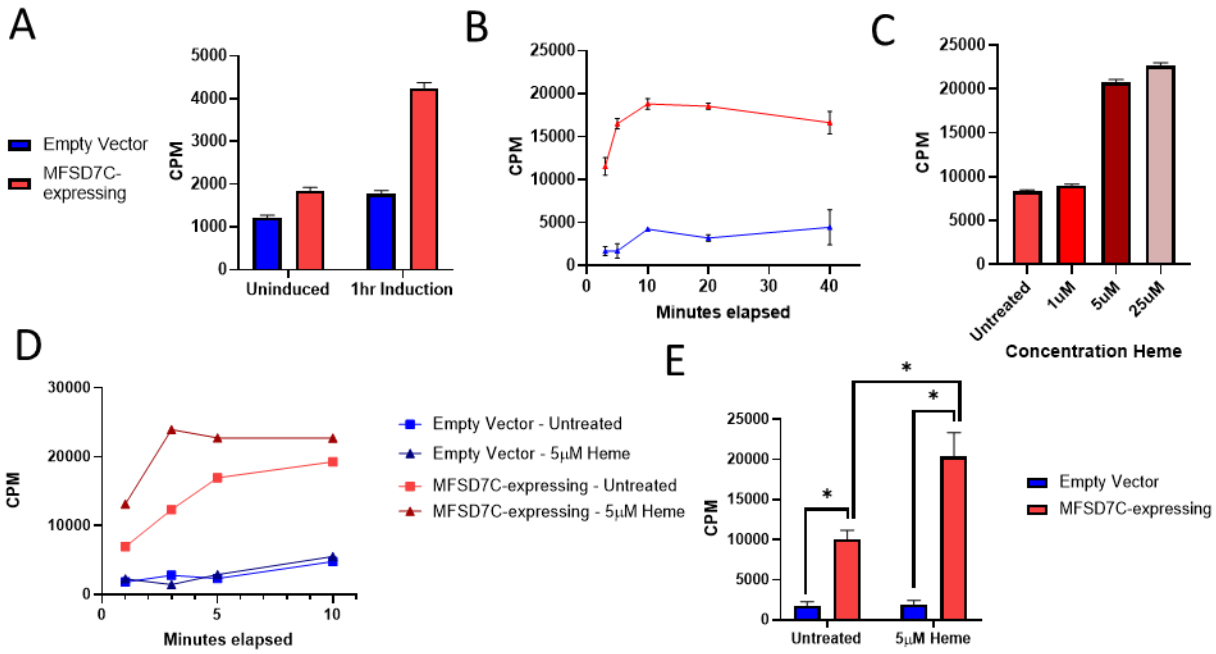

Figure 9 | *E. coli* expressing MFSD7C demonstrate increased rates of 32P-ATP uptake and can further increase their 32P-ATP uptake rate in the presence of heme. A) *E. coli* expressing either high (induced) or low (uninduced) amounts of MFSD7C were compared with *E. coli* transformed using an empty vector and subjected to the same induction or lack thereof. Each was assessed for 32P-ATP uptake after 5 minutes coincubation using a liquid scintillation counter. Induced bacteria were used for the following experiments. **B)** Time points were taken from 3-40 minutes coincubation in two experiments comparing MFSD7C-expressing and empty vector-expressing *E. coli*; each timepoint exhibited a significant difference between the two curves (independent p-values = 0.0068, 0.0024, 0.0011, 0.0006, 0.0193). **C)** Heme was added to MFSD7C-expressing bacteria in varying concentrations three minutes prior to initiating 32P-ATP uptake with five minutes coincubation. **D)** 5μM heme was added to both MFSD7C-expressing and empty vector-expressing *E. coli*, and their 32P-ATP uptake was assessed with four timepoints over 10 minutes. **E)** The 3-minute time point for 32P-ATP uptake was repeated twice for each sample, and the differences were shown to be significant (untreated empty vs MFSD7C: p = 0.0028; 5μM heme-treated empty vs MFSD7C: p = 0.0039; untreated MFSD7C vs 5μM heme-treated MFSD7C: p = 0.0335).

Alveolar macrophages expressing Mfsd7c secrete ATP in response to heme

Now knowledgeable about the rapid kinetics of MFSD7C-mediated ATP release and the heme concentration capable of modulating that rate of ATP transport, we sought to validate

whether or not *7c*$^{-/-}$ AMs exhibited altered levels of ATP release compared with *7c*$^{FL/FL}$ AMs. We used a particular ATP luciferase (RealTime Glo) developed for long-lasting ATP monitoring in cell culture and added it to AMs directly after their adherence to a 96-well plate, 30 minutes after isolation via BAL. BALs were performed in pairs of mice (one *7c*$^{FL/FL}$ and one *7c*$^{-/-}$) to keep conditions as similar as possible for both sets of AMs. However, we observed no significant differences in rates of ATP release as the ATP in solution is slowly consumed over a course of three hours **(Figure 10A)**. Directly after the ATP Glo is added to the AMs, a high degree of luminescence is observed, likely corresponding to significant amounts of dead cells and debris that is present on the tissue culture-treated plate even after washing once with PBS. This high level of luminescence is slowly quenched, however, indicating that it is not representative of the rate of ATP export of any cells but rather represents a process occurring outside equilibrium transport. At three hours post-monitoring, levels of luminescence and therefore ATP were quite stable and 5μM heme was added to the cells **(Figure 10B).**

Heme addition provoked a rapid increase in luminescence from the *7c*$^{FL/FL}$ AMs and a less strong increase in the *7c*$^{-/-}$ AMs; the rate of transport comparing the luminescence obtained 90 seconds after heme addition was compared to that prior to heme addition and shown to be significantly higher in *7c*$^{FL/FL}$ AMs than in *7c*$^{-/-}$ AMs **(Figure 10C)**. After 20 minutes of ATP monitoring, levels returned relatively close to baseline and cells were lysed to assess intracellular ATP levels **(Figure 10D).** Although there may be true differences in these intracellular ATP levels, the results varied too strongly between samples to create significance.

With new evidence of Mfsd7c as a heme-gated ATP transporter, we examined purinergic receptors as a class of proteins that may interact with and mediate some of the

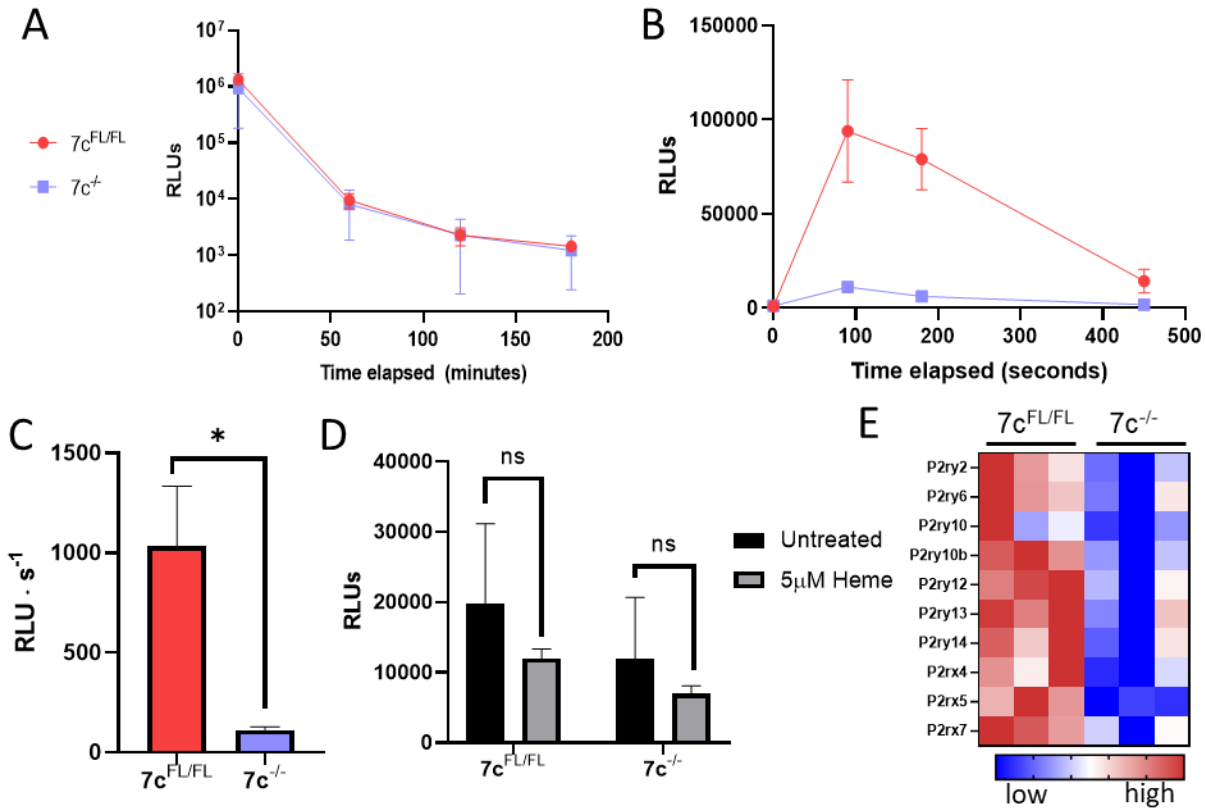

Figure 10 | 7c-expressing AMs secrete ATP in response to heme treatment. Extracellular ATP levels were measured by proxy via addition of RealTime-Glo luciferase in fresh media to wells containing 10^4 AMs, and **A)** time points examining 7c-expressing and 7c-deficient AMs each hour (7+ samples from a total of three mice per genotype) showed no significant differences. **B)** Addition of 5μM heme to both $7c^{FL/FL}$ and $7c^{-/-}$ AMs results in a rapid increase in ATP release from both $7c^{FL/FL}$ and $7c^{-/-}$ AMs, but the **C)** rate of ATP release from $7c^{FL/FL}$ AMs as measured from the first time point is more significant ($p = 0.0286$). D) AMs that had been treated or untreated (same batch) with heme were assayed for intracellular ATP levels 20 minutes after heme addition. **E)** Purinergic receptors as measured via RNAseq of naïve $7c^{FL/FL}$ vs $7c^{-/-}$ AMs demonstrated reduced expression in $7c^{-/-}$ mice.

observed effects associated with Mfsd7c. The altered expression in all purinergic receptors observed in *7c*$^{-/-}$ AMs from RNAseq is displayed to reinforce this notion **(Figure 10E).**

MFSD7C as a heme-gated ATP secretor explains many of the phenomena we have observed previously, namely the rapid increase in thermogenesis upon heme treatment observed in cells expressing MFSD7C. Whereas the protein seemed gated by heme in AMs, *E. coli*

expressing the protein exhibited basal levels of transport even without heme addition. There are a variety of explanations for this observation, but some possibilities include the necessity of a cofactor not expressed in *E. coli* or the fact that half the MFSD7C in *E. coli* may be oriented in the wrong direction. It is possible that the heme gate is only functional at blocking ATP transport coming from the direction of the N-terminal domain, and so half the MFSD7C proteins in *E. coli* are inhibited until addition of heme; this seems to line up with the data obtained thus far.

Discussion

ATP as the substrate for Mfsd7c helps clarify some of the observations we observed when knocking out the gene in AMs. Without Mfsd7c, AMs have a transcriptional signature suggestive of reduced fatty acid oxidation and increased glycolysis. If AMs are secreting ATP using via Mfsd7c, they would need to maintain higher rates of ATP synthesis which can be accomplished via increased fatty acid oxidation. When it is knocked out, the ATP requirements of the cell would be altered and reduced levels of fatty acid oxidation would be needed.

Mfsd7c-deficient AMs also exhibit impaired ability to kill *M. smegmatis*. This may be because increased ATP levels are required for phagocytosis and phagolysosomal acidification, and the cells have downregulated the fatty acid oxidation transcriptional program. Because glucose levels are low in the alveolar surfactant, glycolysis is unlikely to provide the additional ATP needed to counter the infection. This is supported by the fact that glucose supplementation helps alleviate the reduced bacterial killing capacity of the knockout AMs. Furthermore, IFN-gamma is reduced in the $7c^{-/-}$ infections despite the higher quantities of neutrophils, which are likely to be

the source of IFN-gamma. Notably, extracellular ATP has been established as an upstream signal for IFN-gamma release via purinergic signaling (Amores-Iniesta et al. 2017).

In considering the overall AM phenotypes associated with Mfsd7c expression, one possibility is that autopurinergic signaling occurs when Mfsd7c secretion of ATP then binds to the AM's own purinergic receptors. To this end, we performed a correlation analysis examining MFSD7C expression across tissues to those of each purinergic receptor (even though not every purinergic receptor is activated by ATP or its downstream products) (**Supplemental Figure S24A**). We also examined cancers that upregulate MFSD7C (most downregulate the protein) on the hypothesis that the driving factor behind MFSD7C upregulation may be autopurinergic signaling (**Supplemental Figure S24B, C, D**). P2Y13 was the most significantly correlated purinergic receptor across different tissue types and it correlated extremely highly in each cancer examined.

P2Y13 has an established role not only in the induction of heme oxygenase (Perez-Sen et al. 2015) but is also implicated in cholesterol export (Lichtenstein et al. 2013). Calcium signaling (**Supplemental Figure S25**) and cholesterol pathways (**Supplemental Figure S26**) may therefore be aberrant in *7c*$^{-/-}$ AMs due to the modification of this axis. The alveolar macrophage likely needs to transport significant quantities of cholesterol, which makes up ~10% of the pulmonary surfactant, as part of its role in surfactant clearance and lipid catabolism. Changes to this pathway may therefore generate the observed phenotype in AMs via P2ry13 rather than through Mfsd7c itself. A model for such a system is shown in **Figure 11**.

Future experiments and directions

The ATP transport assay in *E. coli* provides a relatively easy and rapid method for examining MFSD7C transport activity. This can be used to evaluate the effect of various Fowler Syndrome mutations and examine whether they affect basal rates of ATP transport or rates associated with heme treatment. Demonstrating that mutations seen in patients with Fowler Syndrome also affect rates of ATP transport would provide even stronger evidence that MFSD7C directly transports ATP, rather than affecting it indirectly (e.g. affecting the integrity of plasma membrane).

It is also possible that the orientation of MFSD7C on the E. coli is random and therefore a combination of proteins oriented in opposite directions, whereas it is likely to only be oriented in one direction in mammalian cells. It is possible that the directionality of the protein affects heme gating or other aspects of the protein, so examining transport using an alternate method may also be important. We are planning to test transport activity in proteoliposomes, but those are similarly likely to contain the protein oriented in both directions.

Working backwards with the knowledge that Mfsd7c transports ATP, there are a variety of experiments that we might perform with AMs. We can examine whether IFN-gamma levels in the knockout infection model can be rescued by simply supplementing extracellular ATP. Similarly, we can assess the extent to which extracellular ATP rescues the impaired bacterial killing phenotype of the knockout AMs. Naïve AMs also have a phenotype associated with reduced fatty acid oxidation; we can test whether this is secondary to autopurinergic signaling by blocking purinergic receptors.

Notably, the protein MFSD7C itself also becomes an interesting target if it does indeed secrete ATP and if it could be activated to do so using a small molecule rather than heme. Such a

molecule might be able to increase thermogenesis and increase oxygen consumption as seen previously in experiments with cell lines, potentially providing a therapeutic avenue to increase fatty acid oxidation and counter obesity and the metabolic syndrome.

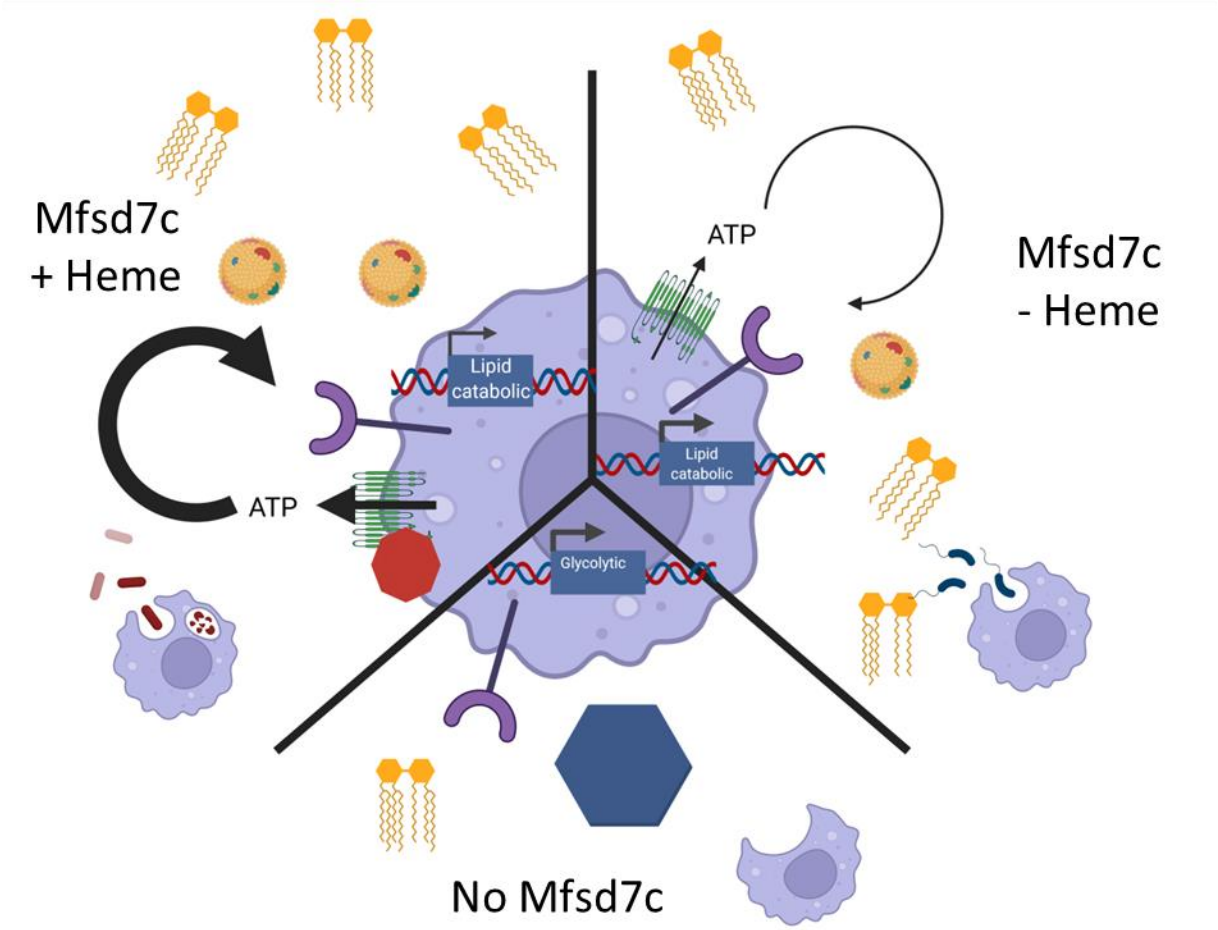

Figure 11 | Model: Mfsd7c releases ATP in response to heme and upregulates fatty acid oxidation and phagocytosis in AMs. Expression of Mfsd7c confers a lipid catabolic role onto AMs, as demonstrated by the change to glycolytic propensity when it is knocked out. It is unclear whether this lipid-oriented state is directly conferred by ATP secretion by the AM, or even if it is related to the transporter substrate at all. The model depicted here suggests that ATP secretion via Mfsd7c may activate P2ry13, a purinergic receptor whose expression strongly correlates with that of Mfsd7c. Activation of this receptor, which is implicated in signaling for HMOX1 transcription and may help to accelerate HDL-mediated lipid transport, supports the AM in its lipid-degrading role. In the presence of heme, the AM increases its cholesterol export and increases its beta oxidation, metabolically preparing it to better scan the alveoli for peroxidized lipids that free heme may create. In the absence of heme, some latent activity of this enzyme supports a less exaggerated lipid-catabolic and phagocytic role, which is sufficient to create the differences observed when Mfsd7c is knocked out and the AMs encounter *M. smegmatis*.

Methods

Zinc mesoporphyrin uptake assay. Zinc mesoporphyrin (SCBT # 14354-67-7) uptake was assessed using AMs plated at $2x10^4$/well in non tissue-culture treated 48-well plates. 30 minutes after adherence to plate in RPMI, RPMI media was removed and cells were washed once in uptake buffer (0.1% bovine serum albumin [BSA], 25 mM HEPES [pH 7.4], 130 mM NaCl, 10 mM KCl, 1 mM CaCl2, 1 mM MgSO4). 5μM ZnMP in uptake buffer was then obtained via dilution of frozen stock ZnMP aliquot in uptake buffer and allowed to stain the AMs for 20 minutes. The AMs were then washed once in 1% BSA in PBS, then once in PBS, and then left in accutase solution for one hour at 37°C. Plate was then moved onto ice and cells were lifted (pipetting up and down) and analyzed using LSR II flow cytometer with 561excitation and 582/15 emission capture.

Expression and purification of human MFSD7C. Nikola Ivica and James Ham prepared purified MFSD7C protein which was frozen down and subsequently used in thermal shift assays; a summary of their optimized protocol is as follows: A lentiviral vector harboring codon-optimized human MFSD7C-TEV-8xHis-2xStrepTagII, expressed under EF-1α core promoter was packaged into lentiviral particles using a calcium phosphate precipitation method of transfection. Lentivirus was used to transduce MCF-7 a Mfsd7b/Mfsd7c$^{-/-}$ double-knockout cell line., which allows for sustained and high expression of the MFSD7C protein. Transduced MCF-7 cells were transitioned into suspension cells with a slow reduction of FBS in the media. For additional expression of MFSD7C, suspension cells were transfected with 400ug of MFSD7C-expression plasmid, at $4x10^6$/mL in a total of 1L shaking cells. After two days of protein induction, the cells were washed once using DPBS resuspended with 40 mL of cold buffer containing 500 mM NaCl, 10% glycerol (v/v), 50 mM HEPES-NaOH pH 7.0, cOmplete Roche protease inhibitors. The resuspension was

sonicated for 2 minutes while on ice in order to shear genomic DNA and break lipid membranes, after which 5 mL of 10% (w/v) n-Dodecyl-β-D-Maltopyranoside (DDM, Anatrace) was added to the lysate (for a final concentration of 1% DDM), mixed and left rotating at 4°C for 30 min to allow for lipid solubilization. The mixture was cleared by centrifugation at 20,000g for 20min at 4°C, and the supernatant was transferred to a fresh 50 mL tube and incubated with 1 mL of pre-equilibrated Strep-Tactin Sepharose Resin (IBA Lifesciences) for 2 hours while rotating at 4°C Protein-bound resin was captured with EconoPac gravity chromatography column (Bio-Rad) and the flow-through was discarded. The resin was washed once with 20 mL of cold buffer containing 500 mM NaCl, 10% glycerol, 0.1% DDM, 50 mM HEPES-NaOH pH 7.0, and once with 20 mL of cold buffer containing 100 mM NaCl, 10% glycerol, 0.05% DDM, 50 mM HEPES-NaOH pH 7.0. MFSD7C was eluted with 8 mL of cold buffer containing 100 mM NaCl, 10% glycerol, 0.05% DDM, 50 mM HEPES-NaOH pH 7.0, 2.5 mM desthiobiotin. The eluted fractions were immediately pooled, concentrated to 3 mL using Amicon Ultra-4 centrifugal filters (Millipore Sigma) and desalted using PD-10 columns (GE Healthcare).

Thermostability shift-based compound screening. The thermostability shift assay was adopted from a previously described protocol (Majd et al., 2018). 5 mg/mL solution of 7-diethylamino-3-(4'-maleimidylphenyl)−4-methylcoumarin (CPM) was dissolved in DMSO and diluted to 0.02 mg/mL (250x dilution) in thermal shift (TS) buffer containing 100 mM HEPES-NaOH pH 7.0, 50 mM NaCl, 10% glycerol, 0.05% DDM and 50μg/mL of purified MFSD7C protein. Equilibration was performed for 15 min at 4°C, after which time 90 μL of the equilibrated protein sample was combined in a qPCR plate wells with 10 μL of the screening compound dissolved in TS buffer. Thermostability of MFSD7C incubated with either 50 mM HEPES-NaOH pH 7.0 or with various

screening compounds was assayed using fluorescence intensity change (Ex/Em = 460/510 nm, standard SYBR-Green setup) in a qPCR machine with the following temperature ramp setup: 20°C pre-incubation step for 3 min, 20-95°C ramp at 1.8°C/min increase, fluorescent reading every 5 seconds. The apparent melting temperature (the inflection point of the fluorescence intensity curve) was determined by fitting the Boltzmann sigmoidal curve to the experimental data using the GraphPad Prism 8.0 built-in analysis.

Expression of MFSD7C in E. coli. Heat-shock competent *E. coli* BL21 cells were freshly transformed each experiment with MFSD7C-His plasmid or puc19 vehicle control plasmid via heat shock at 42°C, 1 hour recovery in SOC, and grown in LB + ampicillin overnight. They were then diluted 1:100 into fresh LB + ampicillin for approximately four hours until they reached an OD600 of 0.1. At this time, IPTG was added to a final concentration of 0.5mM in bacteria with LB + ampicillin, after which bacteria was grown for an additional hour.

α32-ATP uptake in E. coli. Protocol was adapted from one used to identify a separate ATP transporter, AXER, by Klein et al. (Klein et al., 2018). MIT Radiation Protection Program approved research to be pursued and space was established for use and disposal of 32P-ATP. In each experiment, *E. coli* freshly prepared to express MFSD7C or empty puc19 were spun down at 3000g for 15 minutes at 4°C to form a pellet, which was washed twice in cold PBS. OD600 was measured and adjusted to 4.0 in PBS for each sample. For heme treatment, a solution of 10x freshly prepared heme was added to a bulk sample at the appropriate concentration 3 minutes prior to 32P-ATP addition; PBS was added to separate samples for negative controls. For the actual uptake assays, 10µL of OD4.0 *E. coli* were co-incubated with 10µL freshly diluted 32P-ATP

(PerkinElmer # BLU003H250UC, diluted 1:50 in PBS for experiments) and *E. coli* resided in 32P-ATP PBS solution for an experimentally-controlled amount of time. 15 seconds prior to the designated end of uptake, the full 20uL of bacteria and ATP solution was transferred into a 0.2µm syringe filter (Thermo Fisher Scientific #726-2520). At exactly the end of uptake, 20mL of PBS was rapidly passed through the filter, and the syringe filter and contained bacteria/residual PBS were inverted and 5mL of Scintiverse BD Cocktail (Fisher Scientific) scintillation fluid was passed through in the opposite direction to the original *E. coli* addition in order to maximize elution. The radioactivity of the eluted scintillation fluid was then quantified via liquid scintillation counting on a Beckman LS 5000 Scintillation Counter.

AM ATP release assay. AMs were freshly isolated into complete RPMI containing 10% FBS and 2mM L-Glut, concentration of cells was measured via hemocytometer, and 10^4 AMs per well were allowed to adhere to a tissue-culture treated white 96-well optical plate (Greiner). After 30 minutes in cell culture incubator at 37°C, media was removed, 200uL PBS was added and removed to wash cells, and 100uL solution of ATP reporter media, which consisted of 1:20 dilution of stock RealTime-Glo (Promega #GA5010) diluted in Opti-Mem (Gibco). Luminescence was immediately measured via plate reader and subsequent measurements were taken each hour for the next three hours. At the third hour, 10µL of freshly prepared 50µM heme was added to each well containing 100µL (5µM final concentration) and the plate tapped gently to promote diffusion of the heme. Luminescence was measured via plate reader (kept at 37°C) after 90 seconds and measurements were repeated at regular intervals for the desired length of the assay. 20 minutes after the initial heme addition, cells were washed in PBS and the intracellular ATP levels were assessed using a traditional luciferase lysis kit (Sigma-Aldrich #MAK135).

P2GY13 Correlational Analyses. MFSD7C (under the name FLVCR2) expression in various tissues was examined for correlation with purinergic receptor transcripts using AnalyzeR (Miller et al., 2021). The Cancer Genome Atlas (TCGA) was examined for the degree of upregulation or downregulation of MFSD7C across various cancers versus normal tissue using GEPIA (Li et al., 2021), which was also used to examine how purinergic receptor expression varies in cancers where MFSD7C is upregulated and the extent of correlation between each of those purinergic receptors and MFSD7C for each sample for the given cancer.

References

Amores-Iniesta, J. *et al*. (2017) 'Extracellular ATP Activates the NLRP3 Inflammasome and Is an Early Danger Signal of Skin Allograft Rejection', *Cell Reports*, 21(12), pp. 3414–3426. doi:10.1016/j.celrep.2017.11.079.

Duffy, S.P. *et al*. (2010) 'The Fowler Syndrome-Associated Protein FLVCR2 Is an Importer of Heme', *Molecular and Cellular Biology*, 30(22), pp. 5318–5324. doi:10.1128/MCB.00690-10.

Klein, M.-C. *et al*. (2018) 'AXER is an ATP/ADP exchanger in the membrane of the endoplasmic reticulum', *Nature Communications*, 9(1), p. 3489. doi:10.1038/s41467-018-06003-9.

Li, C. *et al*. (2021) 'GEPIA2021: integrating multiple deconvolution-based analysis into GEPIA', *Nucleic Acids Research*, 49(W1), pp. W242-W246. doi:10.1093/nar/gkab418.

Lichtenstein, L. *et al*. (2013) 'Lack of P2Y13 in mice fed a high cholesterol diet results in decreased hepatic cholesterol content, biliary lipid secretion and reverse cholesterol transport', *Nutrition & Metabolism*, 10(1), p. 67. doi:10.1186/1743-7075-10-67.

Miller, H.E. and Bishop, A.J.R. (2021) 'Correlation AnalyzeR: functional predictions from gene co-expression correlations', *BMC Bioinformatics*, 22(1), p. 206. doi:10.1186/s12859-021-04130-7.

Pérez-Sen, R. *et a*l. (2015) 'Neuroprotection Mediated by P2Y13 Nucleotide Receptors in Neurons', *Computational and Structural Biotechnology Journal*, 13, pp. 160–168. doi:10.1016/j.csbj.2015.02.002.

Vandivort, T.C., *et al*. (2016) 'An Improved Method for Rapid Intubation of the Trachea in Mice', *Journal of Visualized Experiments: JoVE*, (108), p. 53771. doi:10.3791/53771.

Appendix 2: Supplementary figures

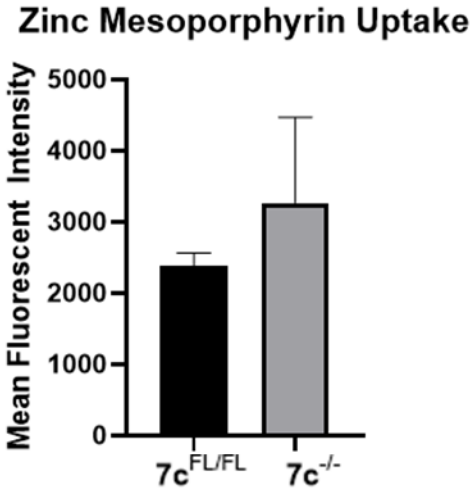

Figure S23 | $7c^{-/-}$ AMs do not uptake zinc mesoporphyrin at a reduced rate. Uptake of ZnMP, a fluorescent heme analog, was compared between $7c^{-/-}$ and $7c^{FL/FL}$ AMs (three mice per genotype). No significant difference was observed.

A

Gene Name	Description	Correlation Value	P Value
P2RY13	purinergic receptor P2Y13	0.344	0.000004175
P2RX7	purinergic receptor P2X 7	0.339	0.000004388
P2RX1	purinergic receptor P2X 1	0.326	0.000005006
P2RX4	purinergic receptor P2X 4	0.318	0.00000544
P2RY6	pyrimidinergic receptor P2Y6	0.239	0.00001376
P2RY14	purinergic receptor P2Y14	0.225	0.00001665
P2RY2	purinergic receptor P2Y2	0.204	0.00002265
P2RY12	purinergic receptor P2Y12	0.178	0.0000346
P2RY4	pyrimidinergic receptor P2Y4	0.146	0.00006361
P2RY11	purinergic receptor P2Y11	0.0347	0.004512
P2RY1	purinergic receptor P2Y1	0.0267	0.009377
P2RX3	purinergic receptor P2X 3	0.0158	0.036
P2RX5	purinergic receptor P2X 5	0.0072	0.1534
PPAN-P2RY11	PPAN-P2RY11 readthrough	-0.0314	0.005982
P2RX2	purinergic receptor P2X 2	-0.0337	0.004902
P2RX6	purinergic receptor P2X 6	-0.0474	0.001837
P2RX5-TAX1BP3	P2RX5-TAX1BP3 readthrough (NMD candidate)	-0.0777	0.0004267

B

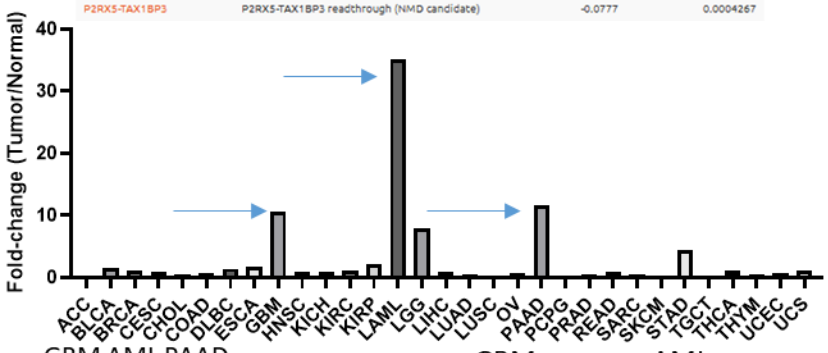

C

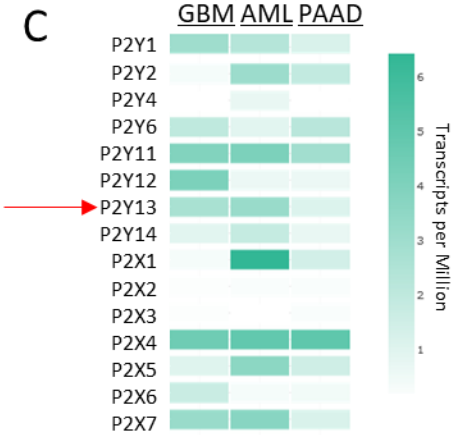

D

	GBM		AML		PAAD	
	p-value	R	p-value	R	p-value	R
P2Y1	0.64	0.037	0.74	0.026	0.0049	0.21
P2Y2	4.10E-05	0.32	0.019	0.18	0.13	0.11
P2Y3	0.63	-0.038	0.67	-0.032	0.35	-0.07
P2Y6	8.30E-09	0.43	0.04	0.16	2.10E-05	0.31
P2Y11	0.22	0.096	0.0077	-0.2	0.4	-0.064
P2Y12	2.30E-06	0.36	0.31	3.50E-05	0.38	1.70E-07
P2Y13	1.10E-15	0.57	0	0.63	2.30E-12	0.49
P2Y14	2.40E-01	0.0016	0.46	0.057	2.20E-06	0.35
P2X1	0.14	0.12	0.38	0.068	4.60E-01	-0.056
P2X2	4.70E-01	-0.057	0.049	-0.15	8.40E-01	-0.016
P2X3	0.94	0.0059	0.46	-0.057	5.10E-01	-0.049
P2X4	0.00E+00	0.66	6.60E-08	0.4	5.90E-01	0.04
P2X5	0.73	-0.027	0.039	-0.16	8.40E-01	-0.015
P2X6	6.10E-01	-0.04	0.18	-0.1	5.60E-03	-0.21
P2X7	0.61	0.04	2.20E-16	0.57	0.00E+00	0.57

Figure S24 | MFSD7C expression closely correlates with that of the purinergic receptor P2Y13. A) A tissue gene expression database was examined for correlation between MFSD7C expression and known purinergic receptors (regardless of substrate). P2Y13, an ADP receptor, was most closely correlated (R = 0.344, p = 0.000004). **B)** The cancer genome atlas was examined for cancers that upregulate MFSD7C; the top three cancers were selected for further analysis (GBM = glioblastoma multiforme, LAML or AML = acute myeloid leukemia, PAAD = pancreatic adenocarcinoma). **C)** Purinergic receptor expression was compared across these three cancer types, and **D)** each receptor was correlated with expression levels of MFSD7C for each sample corresponding to the given cancer. P2Y13 consistently correlated strongly with MFSD7C (R > 0.48 in all cancers examined) with extremely high significance values.

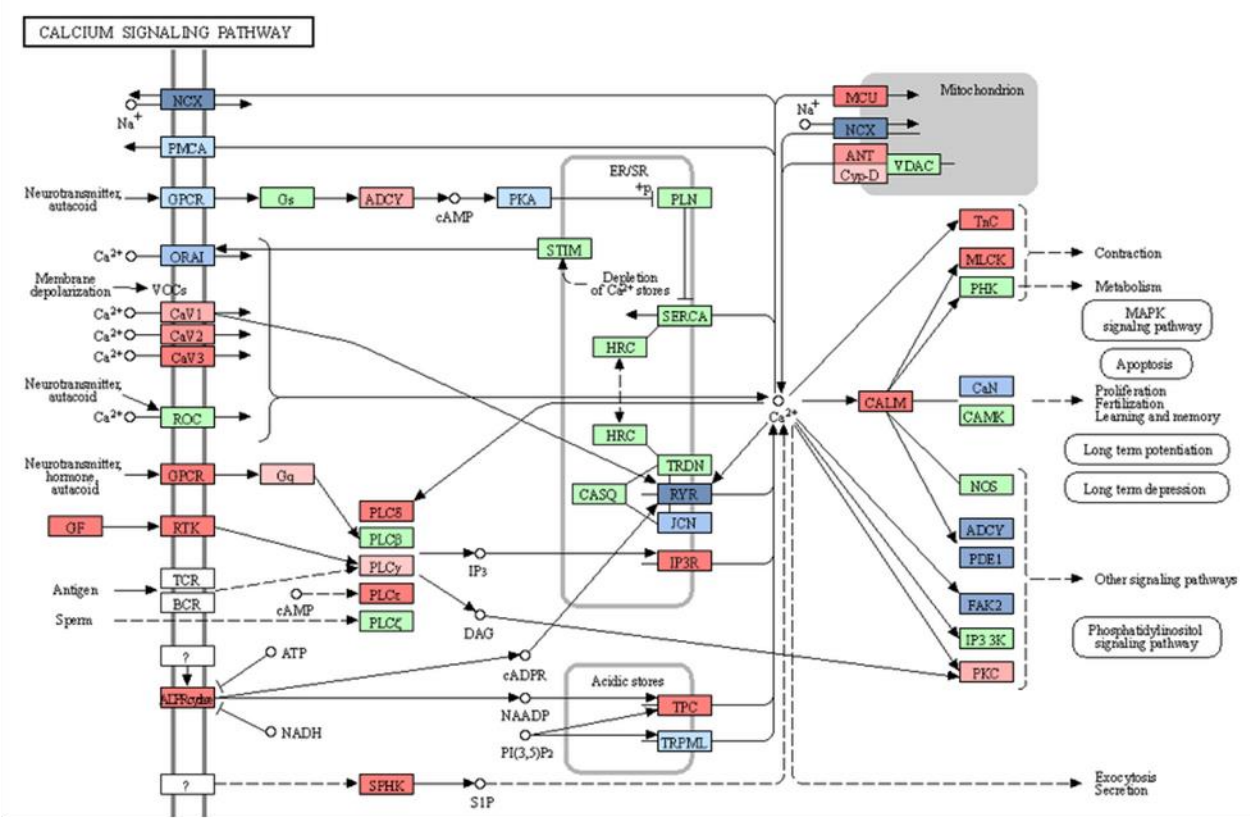

Figure S25 | Changes in transcript values in $7c^{-/-}$ versus $7c^{FL/FL}$ AMs for KEGG Calcium Signaling Pathway (mmu04020) . Blue boxes indicate that the transcript is downregulated at least 25% in $7c^{-/-}$ AMs vs $7c^{FL/FL}$ AMs (dark blue indicates >2-fold decrease), while red indicates that the transcript is upregulated at least 25% in $7c^{-/-}$ AMs vs $7c^{FL/FL}$ AMs (bright red indicates >2-fold increase). White and green boxes represent transcripts that were altered <25% between $7c^{-/-}$ and $7c^{FL/FL}$ AMs or not detected in sufficient abundance from RNAseq (green boxes show genes that differ significantly among species; shown here is a mouse pathway map).

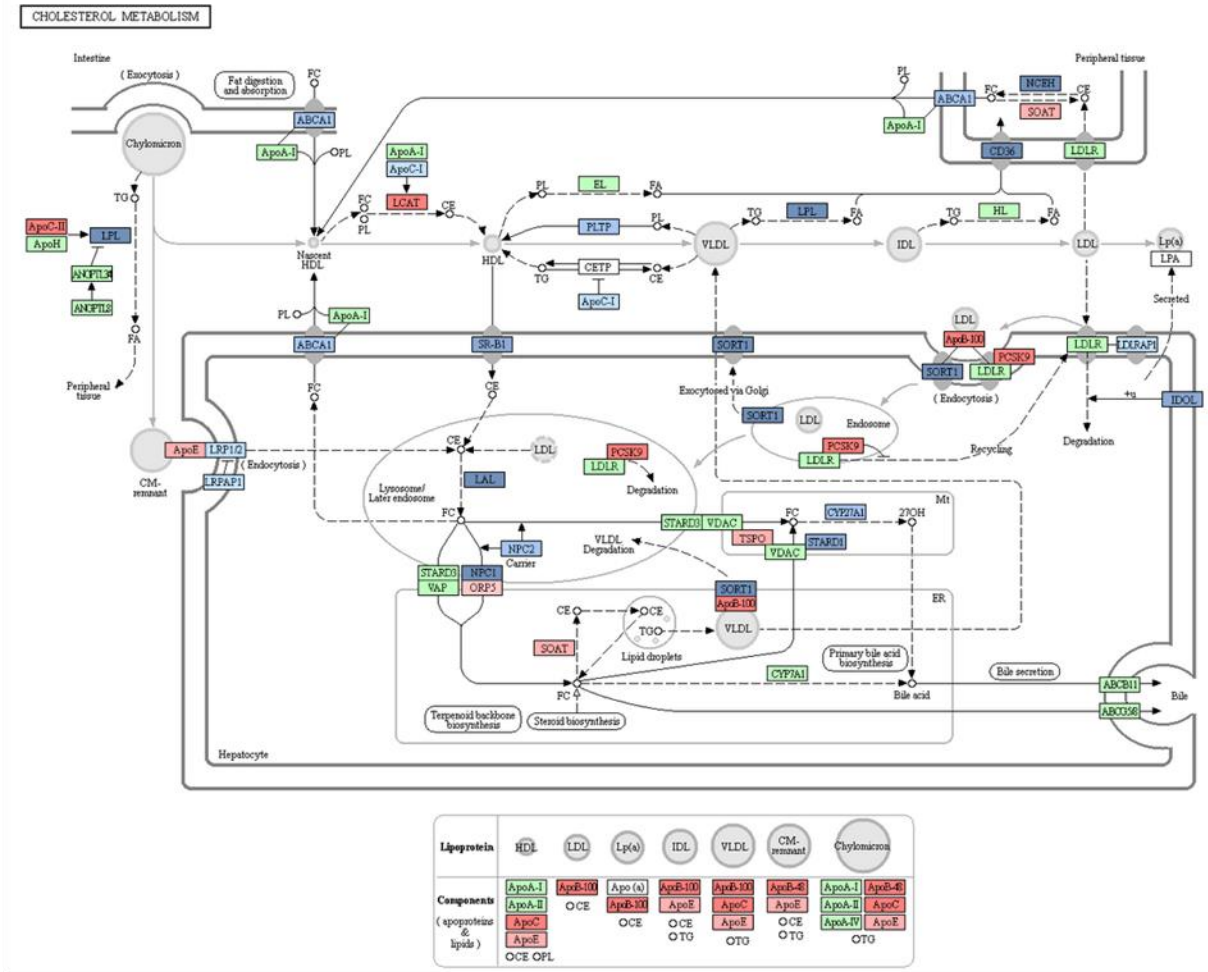

Figure S26 | Changes in transcript values in $7c^{-/-}$ versus $7c^{FL/FL}$ AMs for KEGG Cholesterol Metabolism Pathway (mmu04979) . Blue boxes indicate that the transcript is downregulated at least 25% in $7c^{-/-}$ AMs vs $7c^{FL/FL}$ AMs (dark blue indicates >2-fold decrease), while red indicates that the transcript is upregulated at least 25% in $7c^{-/-}$ AMs vs $7c^{FL/FL}$ AMs (bright red indicates >2-fold increase). White and green boxes represent transcripts that were altered <25% between $7c^{-/-}$ and $7c^{FL/FL}$ AMs or not detected in sufficient abundance from RNAseq (green boxes show genes that differ significantly among species; shown here is a mouse pathway map).